Lung Mechanics and Hyperpolarised Gas MRI

James Thorpe

July 26, 2018

Abstract

Lung diseases affect the lives of millions of people across the UK and result in the thousands of deaths every year. It is therefore vitally important to continue to develop a wide range of diagnostic techniques to improve our understanding of lung diseases and how they can be treated. This thesis provides an overview of the main methods of assessing lung condition before focussing on developments in two specific areas: Forced Oscillation Technique (FOT) and Hyperpolarised (HP) gas MRI.

FOT is an inexpensive, non-invasive lung function test that measures the acoustic impedance of the airways by applying an oscillating waveform via a mouthpiece. FOT cannot be used to image the lung but instead provides information on a variety of other physiological parameters. Two FOT studies are presented in this thesis: a multi-site phantom study and a patient based study. The phantom study confirmed the validity of the Nottingham FOT system used in the patient study and investigated the effects of lung stiffness and airway obstruction on measured FOT parameters using a 3D printed lung phantom, as well as comparing phantom results between three different FOT devices (an in-house device from the University of Nottingham, an Erich Jaeger MasterScreen IOS and a tremFlo C-100 airwave oscillometry system) at two sites (the University of Nottingham and Glenfield Hospital, Leicester). It was found that changes in lung stiffness and airway obstruction are observable in the reactive

and resistive (respectively) components of measured impedance. A difference was seen between the Jaeger IOS system and the other two devices. The patient based study was undertaken to investigate the efficacy of FOT, in comparison to spirometry, in differentiating between three patient groups, healthy, asthmatic and chronic obstructive pulmonary disease (COPD), with a particular focus on investigating the effect of a bronchodilator on measured FOT parameters. It was found that both FOT and Spirometry were effective at differentiating between the patient groups, however, they provided different information about patient response to bronchodilator thus demonstrating that both techniques should be performed to obtain the maximum information about a patients disease state.

HP gas MRI uses isotopes of noble gases, such as ^{3}He and ^{129}Xe, to either image the lungs or perform non-imaging measurements of parameters such as the Apparent Diffusion Coefficient (ADC). A short study using ^{3}He was performed comparing ADC measurements at two different time scales between two sites (the University of Nottingham, 13ms, and the University of Sheffield, 2ms) with a secondary aim of investigating the effect of age on ADC. A study on HP ^{129}Xe MRI is presented covering developments that have been made in various imaging techniques including breathing protocols and scanning techniques. The objective of this study is to establish a reliable scanning protocol using healthy volunteers before expanding the study to investigate different disease states including COPD and idiopathic pulmonary fibrosis (IPF). Although progress has been made in testing the validity of various imaging techniques, with ventilation images at 25mm and 10mm slice thicknesses obtained, more development is still needed to improve the quality of the images in order for them to be useful in a clinical setting.

Publications

- M. Soares, R. Bordas, **J. Thorpe**, B. Timmerman, C. Brightling, D. Kay, K. Burrowes, J. Owers-Bradley and S. Siddiqui. Validation of impulse oscillometry R5-R20 as a small airways dysfunction detection tool in adult asthma. *European Respiratory Journal*, 2016.

- S. Safavi, **J. Thorpe**, B. Haywood, M. Barlow and I. Hall. Hyperpolarised xenon-129 MRI of lungs in healthy volunteers: a safety & feasibility study. *Thorax* 2016;71:A105

- S. Safavi, C. Arthofer, **J. Thorpe**, M. Barlow, I. Hall. Reproducibility of hyperpolarised xenon-129 MRI (129Xe-MRI) of lungs in healthy volunteers. *European Respiratory Journal* 2017 50: PA3743; DOI: 10.1183/1393003

- C. Arthofer, A. Pitiot, **J. Thorpe**, S. Safavi, M. Barlow, B. Haywood and I. Hall. Consistent quality assessment in hyperpolarized lung MRI. *PiNG*, 2017

Acknowledgements

My first thanks must go to God who makes all things possible. There are also many people who must be thanked for their invaluable contributions to this work. In fact, there are too many to be able to mention everyone who has helped me in the duration of this project so if you are not directly mentioned I hope you know that I am grateful for all that you did.

Foremost among those who deserve thanks is my supervisor, Prof. John Owers-Bradley who I thank for giving me this opportunity to study and learn and provided an incredible amount of support, ideas, advice and all sorts of other general help throughout the whole process. I must also thank my second supervisor, Dr. Michael Barlow for his help and assistance with ideas for the Xe MRI project as well as for his labours in producing many bags of hyperpolarised xenon.

Many thanks must also go to the various people who have helped with the various different projects undertaken during my time at the University of Nottingham. On the FOT project these include Prof. Dominick Shaw and Marica Soares, and for the HP gas MRI I would like to thank everyone who helped at SPMIC-QMC, especially Brett Haywood for all his help with the project, Steven Hardy for his contributions and support, Shahideh Safavi and Christoph Arthofer.

None of this would have been possible without funding from the Haydn Green Foundation so I extend my thanks for funding this project.

I would also like to thank my family for their support, particularly my fantastic wife Naomi who was a constant source of encouragement, confidence and loving help along the way.

Finally I would like to thank my numerous friends in the department who made my time at the University all the more enjoyable. Special thanks must go to Richard Cousins for making the office a fun environment, and to Ryan Beardsley, Ashley Tyler and Duncan Parkes for accompanying me on our morning gym sessions. Thanks also to (in no particular order) Chris Judd, James Thomas, Maike Ostmann, Loredana Vasiloiu, Josh Whale, Caroline Poyser, Bill York, Sarah Heywood, Andrew Morley, Stuart Bowe, Vicky Hills, and Dave Peat.

Contents

1 The Respiratory System **1**

1.1 Lung Anatomy, Physiology and Pathology 1

1.1.1 Anatomy and Physiology 1

1.1.2 Lung Pathology 7

1.2 Assessing Lung Condition 11

1.2.1 Introduction 11

1.2.2 Lung Function Tests 12

1.2.3 Lung Imaging 26

1.3 Conclusion 39

2 Forced Oscillation Technique **42**

2.1 Introduction 42

2.2 Theory 44

2.2.1 The Forced Oscillator 44

2.2.2 Electric Circuit Models 46

2.3 Method - Phantom Study 54

2.3.1 Equipment 54

2.3.2 Parameter Evaluation 60

2.3.3 Measurement Procedure 60

2.4 Results - Phantom Study 61

2.4.1 Barrel Phantom 61
2.4.2 Printed Airway Phantom 64
2.4.3 Comparison of FOT devices 71
2.5 Method - Patient Study 76
2.5.1 Data Acquisition 76
2.6 Results - Patient Study 77
2.6.1 Patient Baseline 77
2.6.2 Identifying Disease Type using FOT 77
2.6.3 Effect of Bronchodilator on FOT 87
2.7 Conclusion 99

3 Hyperpolarised Gas Magnetic Resonance Imaging 103

3.1 Introduction 103
3.2 Theory 105
3.2.1 Nuclear Magnetic Resonance 105
3.2.2 Magnetic Resonance Imaging 111
3.2.3 Gas Polarisation 118
3.3 ^{3}He MRI Study 123
3.3.1 Method 123
3.3.2 Pulse Sequences 125
3.3.3 Results 133
3.4 ^{129}Xe Study Method 136
3.4.1 Collaborators 136
3.4.2 Equipment 137
3.4.3 Pulse Sequences 142
3.4.4 Scan Visit Protocol 143
3.5 Image Processing 147
3.5.1 Image Reconstruction 147
3.5.2 Signal-to-Noise Ratio Analysis 150

3.5.3 Super Resolution 155
3.6 ^{129}Xe MRI Development Results 158
3.6.1 Polarisation 158
3.6.2 Dynamic Imaging 159
3.6.3 Coronal Projections 162
3.6.4 Slice Thickness 166
3.6.5 Transverse Plane Imaging 171
3.6.6 Flushing Breath 175
3.6.7 Dissolved Phase Imaging 179
3.7 Conclusion 182

4 Conclusions and Future Work **184**
4.1 Conclusions 184
4.1.1 FOT 184
4.1.2 Hyperpolarised Gas MRI 188
4.1.3 Comparison of Modalities 191
4.2 Future Work 192
4.2.1 FOT 192
4.2.2 Hyperpolarised Gas MRI 193

List of Abbreviations

Abbreviation	**Meaning**
Lung Diseases	
ACOS	Asthma-COPD Overlap Syndrome
CF	Cystic Fibrosis
COPD	Chronic Obstructive Pulmonary Disease
IPF	Idiopathic Pulmonary Fibrosis
Lung Function	
FEV_1	Forced Expiration Volume in 1 Second
FRC	Functional Residual Capacity
FVC	Forced Vital Capacity
LCI	Lung Clearance Index
RV	Residual Volume
TLC	Total Lung Capacity
Lung Function Tests	
FOT	Forced Oscillation Technique

IOS	Impulse Oscillometry
MBW	Multiple Breath Washout
Medication	
BD	Bronchodilator
SABA	Short-Acting Beta Agonists
FOT Parameters	
aRIC Model	Augmented Resistor-Inductor-Capacitor Model of Respiratory Impedance
C_p	Component of Peripheral Capacitance for aRIC Model
f_{res}	Resonant Frequency
I	Inductive Component of aRIC model
p	Pressure measured at the mouth during FOT
Q	Flow Rate measured at the mouth during FOT
R	Resistive Component of Respiratory Impedance
R_c	Central Resistive Component of aRIC Model
R_5	R measured at 5 Hz
R_{20}	R measured at 20 Hz
$R_5 - R_{20}$	R measured at 20 Hz subtracted from R measured at 5 Hz
X	Reactive Component of Respiratory Impedance
Z	Respiratory Impedance

Lung Imaging	
CT	Computed Tomography
MRI	Magnetic Resonance Imaging
NMR	Nuclear Magnetic Resonance
PET	Positron Emission Tomography
r.f.	Radio Frequency
SPECT	Single-Photon Emission Computed Tomography
Hyperpolarised Gas MRI	
ADC	Apparent Diffusion Coefficient
CMRS	Clinical MR Solutions
HP	Hyperpolarised
MEOP	Metastable Exchange Optical Pumping
ROI	Region of Interest
SEOP	Spin Exchange Optical Pumping
SNR	Signal-to-Noise Ratio
MRI Pulse Sequences	
CPMG	Carr-Purcell-Meiboom-Gill Sequence
FGRE	Fast Gradient Echo
FSE	Fast Spin Echo
STE	Stimulated Echo

Chapter 1

The Respiratory System

1.1 Lung Anatomy, Physiology and Pathology

1.1.1 Anatomy and Physiology

The Thoracic Cavity

Respiration is the biological process of converting sugar (glucose) and oxygen into carbon dioxide and water in order to provide cells with energy. In a single-celled organism the required oxygen and waste carbon dioxide can travel to and from the surface to the centre of the cell by simple diffusion. However, for a larger sized organism a system is required for these gases to be spread throughout the entire body. In the case of humans this is done with the circulatory system which uses the heart and haemoglobin in red blood cells to transport the oxygen and carbon dioxide to and from where it is needed. This works in conjunction with the respiratory system which brings oxygen into the body from the atmosphere and removes excess carbon dioxide from the circulatory system, in a process known as gas exchange.

The thoracic cavity is located in the upper half of the torso and is surrounded by the thoracic walls, which contain the ribcage and intercostal muscles, and is separated from the abdominal cavity by the dome shaped diaphragm. It is further divided into three smaller compartments, the two separate pulmonary cavities and the mediastinum. Each pulmonary cavity contains one lung enclosed in a pleural sac whilst the mediastinum, which sits between the two pulmonary cavities, contains the heart, trachea, oesophagus and large blood vessels. The inner and outer layers of the pleural sac are called the visceral and parietal layers with the visceral layer in contact with the lung and the parietal layer in contact with the thoracic wall. The pleural cavity refers to the space between these layers and is at a pressure that is lower than the atmospheric pressure. This lower pressure environment is essential for the lungs to inflate and deflate during breathing.

Gas Exchange

Effective gas exchange is dependent on three key factors. Firstly the air within the lungs must be well ventilated to remove the carbon dioxide and bring in oxygen. Perfusion is the second key factor and refers to the necessity of a good supply of red blood cells to the lungs for gas exchange. The third factor is that the distance between the red blood cells and the gas exchange surface of the lungs needs to be a small as possible for effective diffusion. Overall the rate of diffusion is described by Fick's law:

$$J = -AD\frac{\Delta C}{\Delta x} \tag{1.1}$$

where J is the rate of diffusion, A is the area of diffusion, ΔC is the concentration difference, Δx is the thickness of the barrier between the gas and the blood and D is the diffusion constant which is dependent on the properties of the gas and tissue. From this equation it can be seen that to increase the rate of

gas exchange the red blood cells need to be brought as close as possible to the largest area of the lungs. For this reason the lungs contain a large number of small air sacs called alveoli that are each covered in a network of capillary blood vessels thus maximising the area for diffusion whilst minimising the distance.

Inhalation occurs when the diaphragm contracts and flattens and the intercostal muscles contract pulling the ribs up and out from the centre of the body (the pectoral muscles can also have a part in this if the arms are braced). This increases the volume of the pleural sac. The lungs expand into the pleaural sac due to the pressure difference between them. This increased volume lowers the pressure within the lungs thus drawing external air into the lungs. Conversely passive exhalation is caused by the relaxation of the diaphragm and muscles with the elastic nature of the lungs providing the main force to expel the air. Forced exhalation can be achieved by contracting the abdominal muscles, thus pushing up the diaphragm, and contracting the internal intercostal muscles [1]. This process is shown diagrammatically in Figure 1.1.

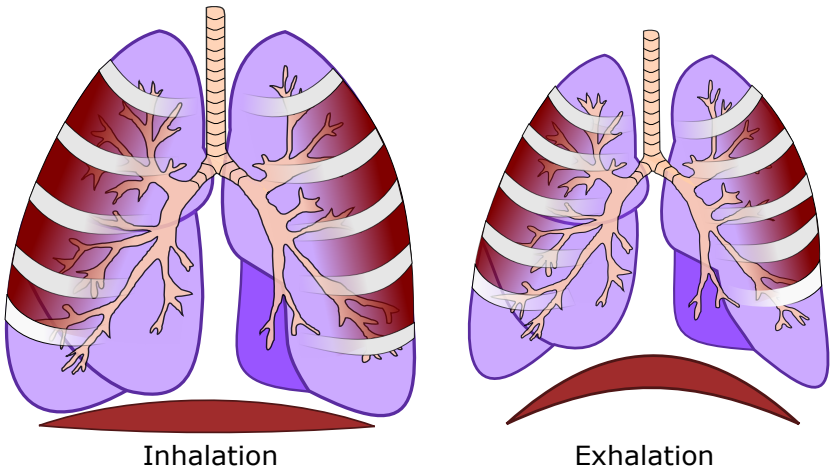


Figure 1.1: The anatomical differences between inhalation (with the diaphragm contracted and flat and the intercostal muscles contracted to expand the ribcage) and exhalation (with the diaphragm relaxed and "domed" and the ribcage less spread).

The Respiratory Tract

During inhalation air is draw into the body through either the nose, into the nasal cavity, or the mouth where it enters the oral cavity. These cavities are connected by the pharynx at the back of the throat. The pharynx is in turn connected to the trachea, which leads to the lungs, and the oesophagus which connects the mouth to the stomach. In order to prevent food from entering the lungs a flap of cartilage, the epiglottis, covers the trachea during swallowing. The larynx is the organ of voice production and also has a role in preventing food and other unwanted substances from entering the lungs. It connects the pharynx to the trachea acting as an open valve during breathing but moving forwards and upwards to underneath the tongue during swallowing. These component parts of the respiratory tract, as well as the upper part of the trachea, are all located above the thorax and so are referred to as the upper respiratory tract [2].

The lower respiratory tract refers to the organs and structures of the respiratory tract located within the thoracic cavity. The main structure within the lower respiratory tract is the large network of branching airways called the tracheobranchial tree [2]. This has two zones, the conducting zone, which distributes air through the lung, and the respiratory zone where gas exchange occurs. The conducting zone begins with the trachea which is a tube wrapped in rings of cartilage for support and has the function of being the inlet of air into the thoracic cavity. The trachea bifurcates at its base splitting into the two main bronchi which each act as the inlet into the two pulmonary cavities and lungs. Once inside the lungs the bronchi continue to divide into smaller bronchi which in turn branch into smaller bronchioles after eleven generations [3]. As well as being smaller, bronchioles are different from bronchi as bronchi have supporting cartilage and submucosal glands whilst bronchioles do not. Bronchioles continue to divide for a further ten or more generations ending with the terminal bronchioles which supply the respiratory zone of the tracheobranchial tree. Due to the branching nature of the airways, the respiratory zone consists of several small units called acini [4]. The acinus is the site of gas exchange and consists of respiratory bronchioles which each branch into approximately five or six alveolar sacs. These alveolar sacs contain several alveloi such that in total the average lung contains 150 to 400 million alveoli with a large surface area of 50 to 100 m^2 [5]. This combined with the fact that the alveoli are only one cell thick results in efficient gas exchange. The tracheobranchial tree is shown in Figure 1.2.

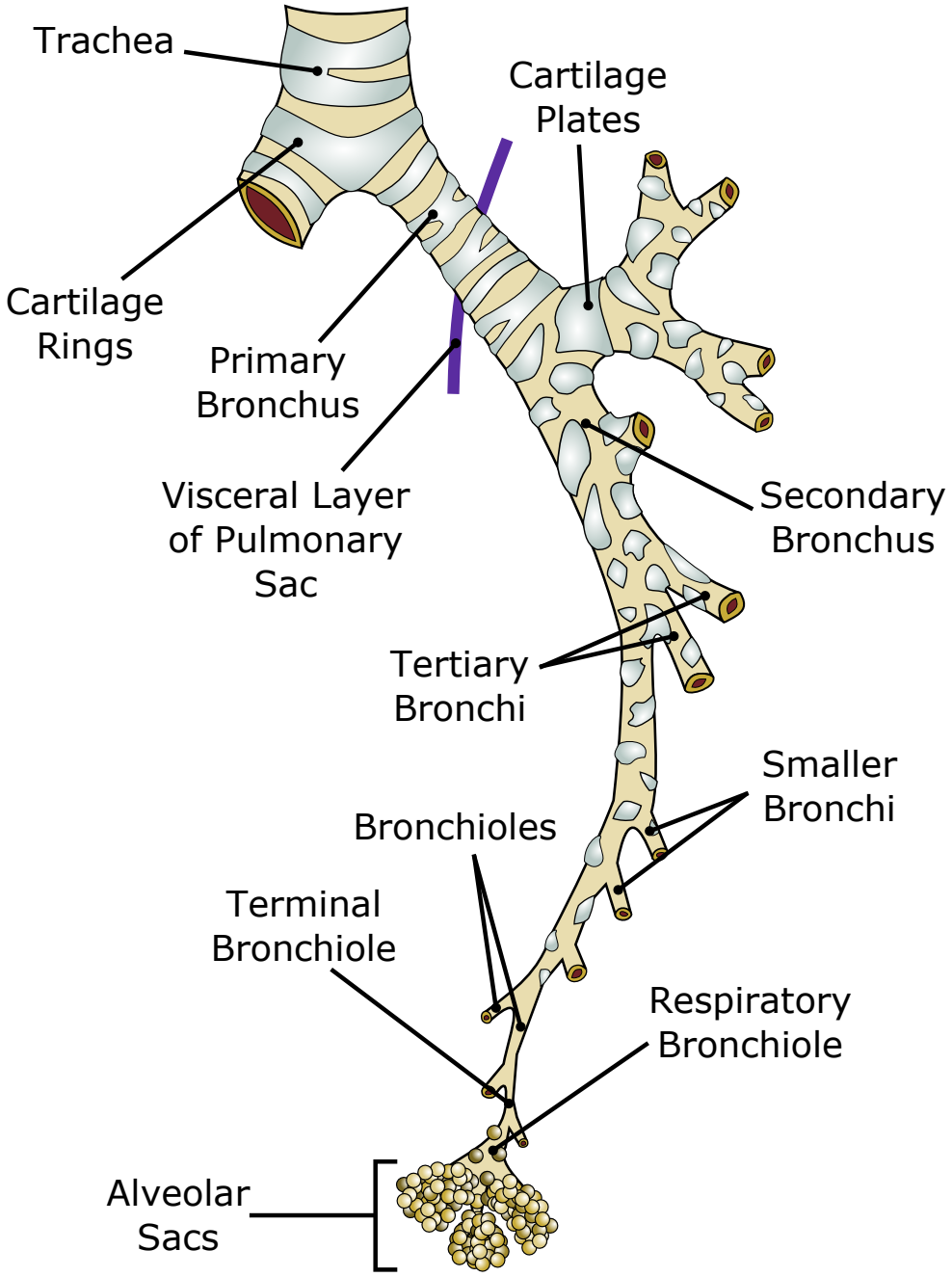


Figure 1.2: Schematic diagram of the lower respiratory tract showing the branching of the airways from the trachea to the alveolar sacs.

Overall the lungs are made up of five lobes. The right lung has a superior, middle and inferior lobe whilst the left lung only has a superior and inferior lobe. This difference is due to the heart which is more prominent on the left side of the body thus reducing the space available for the left lung. The nasal cavity, pharynx and conducting zone of the tracheobronchial tree have mucus glands and ciliated epithelial cells. These have the function of trapping dust and bacteria and wafting them into either the oesophagus to be destroyed by the stomach, or to the mouth or nose to be expelled from the body [6, 7].

1.1.2 Lung Pathology

Lung diseases are extremely prevalent affecting one in five people in the UK. Common conditions include the stiffening of the lungs, build-up of mucus and breakdown of the smaller airway structures. Lung disease can have a large impact on well-being due to common symptoms (such as breathlessness, wheezing and coughing) preventing patients from performing physical activities such as exercise, housework or moving around the house. Severe cases of lung disease can be fatal with lung disease causing 20.1% of deaths in the UK in 2012 [8].

There are two main types of lung disease: obstructive and restrictive. An obstructive disease is one in which the patient experiences difficulty in rapid exhalation due to a narrowing of the airways. However, with an obstructive disease the capacity of the lung is unchanged and remains comparable to that of a healthy person. In the case of a restrictive lung disease the amount of air held within the lungs is reduced due to the lungs being unable to fully expand. In many cases patients can exhibit signs of both obstructive and resistive lung diseases such as asthma and COPD being potentially both obstructive and restrictive in nature.

Asthma

Asthma is an obstructive airways disease that gives rise to breathing difficulties due to inflammation of the airways and airway hyperresponsiveness. Bronchial obstruction due to inflammation has several contributory factors including smooth muscle constriction, thickening of the airway wall due to small muscle hypertrophy (increased muscle size) and oedema (build-up of fluid), and mucous hypersecretion leading to a build-up of excess mucus lining the lumen of the airways [9]. These factors result in a narrowed airway thus impeding airflow [10]. Acute asthma is due to smooth muscle spasms and blockage due to mucus plugging. The hyperresponsive element of asthma refers to the airways overreacting to stimuli. There are various triggering stimuli that affect different patients with common stimuli including particles such as dust, smoke and pollen. There are also other stimuli such as stress[11].

One of the characteristic features of asthma is that the airway obstructions are typically temporary and not in a fixed location. However, in severe cases, chronic inflammation can occur leading to necrosis of bronchial epithelial cells, fibrosis and oedema. Symptoms including breathlessness, chest tightness, coughing, wheezing and fatigue. Asthma is a condition that can be managed by avoiding known triggers and through drug treatment including the use of short-acting bronchodilators, regular inhaled anti-inflammatory agents and inhaled or ingested steroids [12].

COPD

Chronic obstructive pulmonary disease (COPD) is one of the leading causes of death in the UK resulting in between 25,000 to 30,000 deaths per year [8]. COPD is an umbrella term for several obstructive airways diseases, the most prominent of which are chronic bronchitis and emphysema [12]. The pathology of chronic bronchitis is comparable to the bronchial inflammation present in

asthma with obstruction caused by hyperplasia of the goblet cells resulting in a large excess of mucus. However, unlike asthma, in the case of chronic bronchitis the inflammation is more permanent and the mucus build-up can then lead to damage to the ciliated epithelial cells lining the bronchi, which greatly increases the chances of bacterial infection. Chronic bronchitis is clinically defined as a persistent cough with sputum production for at least three months [11].

Emphysema is a breakdown of the alveolar structure of the lungs due to the permanent enlargement of air spaces distal to the terminal bronchiole along with the destruction of their walls. As a result the lungs are filled with larger sacs called bullae instead of alveoli, thus reducing the surface area over which gas exchange can occur. Emphysema also causes a decrease in the elasticity of the lungs due to damage to the elastic fibres [13, 14]. There are different forms of emphysema that refer to distribution of damaged areas within the acinus. The two main types are centriacinar emphysema, which refers to damage to the centre of the acinus and is associated with chronic bronchitis, and panacinar emphysema, which refers to damage to the whole acinus and is not associated with chronic bronchitis[11].

Cigarette smoking is the primary cause of COPD due to the impairment of ciliary movement, causing mucus gland hypertrophy and altering the structure and function of alveolar macrophages [15]. Other factors leading to the development of COPD include exposure to atmospheric pollution, recurrent bacterial infection and genetic abnormality. Symptoms include productive cough, breathlessness, wheezing, infective exacerbations and air trapping [12]. COPD can be managed using steroids and bronchodilators which can reduce hyperinflation by reducing the volume of trapped air within emphysematous regions of the lungs. Antibiotics and vaccines for other diseases (such as the annual flu vaccine) are used to prevent secondary illness caused by infection. In certain cases surgery

can be performed to remove emphysematous lung with severe exacerbations treated using oxygen. One of the most important aspects of treating COPD is to encourage smoking cessation to reduce the rate of deterioration [11].

ACOS

The similarity in the pathology of asthma and COPD causes difficulty in diagnosing patients who exhibit clinical features of both diseases. Recently a new term called asthma-COPD overlap syndrome (ACOS) has been introduced to describe patients in this situation. Features of ACOS include restrictions to airflow that are persistent and not fully reversible (often with a high amount of variability and airway hyperresponsiveness), difficulty in breathing after exertion (again with high variability) and exacerbations occurring at a higher rate than expected in COPD alone. The symptoms of ACOS worsen over time but can be partly reduced by treatment [16].

IPF

Idiopathic pulmonary fibrosis (IPF) is a rare disease affecting between 0.001% and 0.005% of the population with a mean age at presentation of 71 and is very rare in people under 50. The pathogenesis of IPF is unknown, however the condition affects twice as many men as women and has strong associations with smoking cigarettes. There are many unknown aspects of IPF despite many developments in understanding the disease over the past decade [11, 1]. The main feature of IPF is established fibrosis (build up of scar tissue) of the lungs reducing elasticity resulting in a breakdown of the alveolar sacs which reduces the gas exchange area. Another aspect of IPF is mild to moderate interstitial inflammation (inflammation of the tissue supporting the air sacs). IPF primarily affects the lower lobes of the lung spreading upwards as it progresses. As a result many patients with IPF have other lung diseases such as centriacinar emphysema [17, 18]. There is also an association between IPF and lung cancer,

however how much IPF increases the risk of developing cancer is disputed [19].

Symptoms of IPF include breathlessness (initially on exertion but progressing), dry cough, fatigue, weight loss, swelling of the fingers, and audible bilateral end-inspiratory crackles originating from the base of the lungs. There is no known cure for IPF. Primarily treatment of symptoms is done using immunosuppressants to slow the development of scarring however this has only been effective in some cases. Other attempted drug treatments include antioxidants, steroids and anticoagulants which have shown promise in slowing disease progression, however these treatments are all still in the developmental stage. Oxygen treatment can be used to reduce the impact of IPF, and in some cases transplantation can be performed [20, 21].

Further information on lung anatomy, physiology and pathology can be found in the following textbooks: [2, 11, 12, 1].

1.2 Assessing Lung Condition

1.2.1 Introduction

There are numerous techniques for assessing the condition of the lungs and respiratory system. These can be grouped into two main categories: non-imaging and imaging. Non-imaging techniques provide information about the physiology of the lung measuring metrics such as lung volume and flow rate. However non-imaging modalities, by their nature, provide limited anatomical information. On the other hand some imaging modalities, such as planar x-ray and CT, provide primarily anatomical information with limited physiological information, whilst other imaging modalities such as MRI and nuclear medicine can provide both anatomical and physical information.

The main advantage of non-imaging lung function tests is that they are cheaper, easier and generally have fewer safety concerns (i.e. no ionising radiation or large magnetic fields). However the lack of anatomical information provided limits the scope of their usefulness. It is therefore the case that different conditions require different examinations to provide a detailed diagnosis. This section will describe some non-imaging and imaging modalities in general terms to provide context to the modalities used in this thesis, with greater detail on the theory of these modalities provided in their respective chapters.

1.2.2 Lung Function Tests

Lung function tests are non-invasive methods of examining the various volumes and flow rates associated with the lungs during a patients breathing and include spirometry, Forced Oscillation Technique (FOT), body plethysmography and multiple breath washout. The most important lung volume measurements are highlighted in Figure 1.3 which shows lung volume against time for a typical healthy human with the following commonly measured volumes highlighted: *a*) Tidal Volume; *b*) Functional Residual Capacity (FRC); *c*) Residual Volume (RV); *d*) Forced Vital Capacity (FVC); and *e*) Total Lung Capacity (TLC).

The Tidal Volume (*a*) is the volume inhaled and exhaled during normal breathing. FRC (*b*) and RV (*c*) both refer to the volume of air remaining in the lung after exhalation with FRC being the volume remaining after a normal breath and RV being the minimum possible volume of air remaining in the lung after forced exhalation. FVC (*d*) and TLC (*e*) both refer to the maximum volume of the lungs with FVC referring to the difference in volume between maximum inhalation and maximum exhalation and TLC including the additional RV that is always present in the lungs.

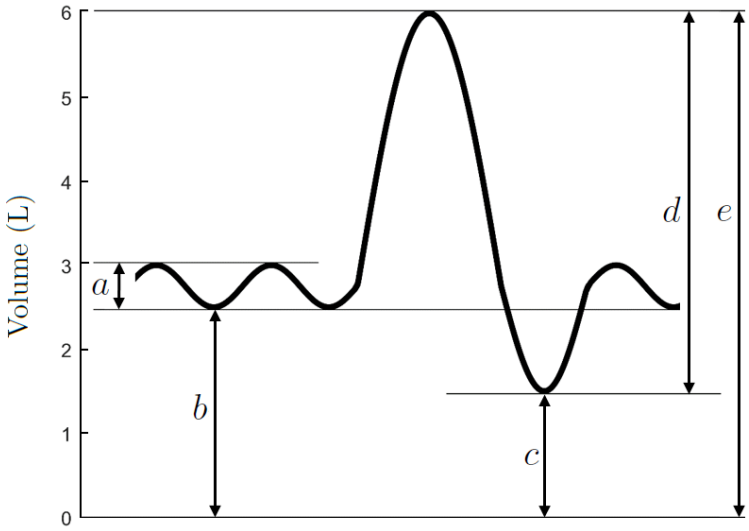


Figure 1.3: Lung volume against time for a typical healthy human where a is the Tidal volume, b indicates the Functional Residual Capacity (FRC), c is the Residual volume, d is the Forced Vital Capacity (FVC) and e indicates Total Lung Capacity (TLC)

Spirometry

Spirometry is one of the mostly commonly performed lung function tests and is used to measure various parameters during normal breathing, such as tidal volumes, and others parameters during forced breathing such as FVC. Spirometry utilizes a device called a spirometer to monitor air flow during patient tidal and forced breathing by having the patient breathe through the mouth into a mouthpiece connected to a tube whilst wearing a nose-clip. This allows for the measurement of flow rate during breathing as well as lung volume. However, no anatomical information is acquired. Spirometry is an effective method of identifying whether a lung disease is obstructive or restrictive with the most common diseases monitored using spirometry being asthma, COPD, CF and pulmonary

fibrosis.

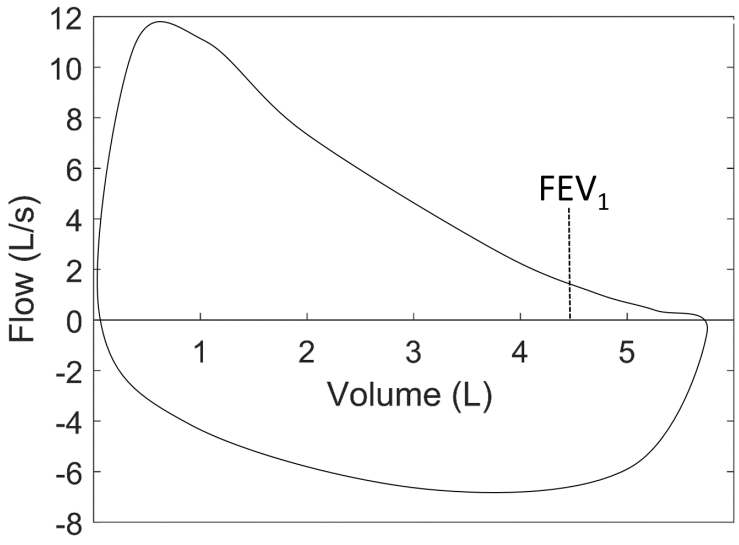


Figure 1.4: A typical flow-volume loop for a healthy person with FEV_1 shown.

One of the main parameters measured by spirometry is the forced expiration volume in one second (FEV_1), which is the maximum volume of air a patient can exhale from their lungs in one second. This has a typical value of typically around 2 to 5 litres for a healthy person, depending on their age, height, sex etc. In order to remove the factors of age and height etc. it is common practice to express FVC and FEV_1 as a percentage of the predicted value for the patient [22]. These measurements are well validated and provide information on the degree of airway obstruction, which can aid diagnosis or be used to monitor response to treatment [23]. The standard way to display spirometric data is in the form of a flow-volume loop where the flow rate for an exhalation/inhalation cycle is plotted against the volume exhaled/inhaled. A typical flow-volume loop with the value of FEV_1 highlighted is shown in Figure 1.4 where expiration has

a positive value and inspiration has a negative value with the intersect being the FVC. This loop should be read in a clockwise direction.

One significant issue with spirometry as a pulmonary function test is that it requires a large amount of patient cooperation. In order to find the FVC of a patient, the patient is required to inhale to their maximum lung capacity. Similarly for FEV_1 the patient is required to forcibly exhale as hard as they can. Both of these can be difficult for patients, particularly patients with severe lung disease, and so the results of the test can be affected. There are no significant side effects to spirometry although the forced exhalations can cause dizziness.

FOT/IOS

Introduction

The first detailed study of the mechanics of breathing was carried out by Otis et al. in 1950 [24] who looked at the forces needed for breathing and the elastance of the lungs. In 1954, Mead and Whittenberger went a step further and investigated pulmonary air flow resistance [25]. They concluded that there was both an in phase component and an out of phase component to the air flow resistance, which they labelled "lung resistance" and "lung elastance" respectively. Otis et al. recognised that heterogeneous damage to the lung would affect these properties and so, by probing these properties at different frequencies, the extent of the damage to the lung could be observed.

The Forced Oscillation Technique (FOT) is a non-invasive method of assessing lung condition by measuring the respiratory acoustic impedance of the lungs through the application of pressure waves to the patient's airways, via the mouth, during normal tidal breathing and was first developed in 1956 by Dubois et al. [26]. As the measurements occur during tidal breathing, FOT, unlike spirometry, does not require a high level of patient cooperation as no ab-

normal breathing patterns are required from the patient, which increases patient comfort and the reliability of the test. FOT was first introduced in a clinical setting in 2003 by Oostveen et al. [27], who looked at children, before Goldman et al. expanded the research to include adults in 2005 [28]. The impedance (Z) of the airways is defined as:

$$Z = \frac{p}{Q}, \tag{1.2}$$

where p is pressure and Q is flow.

In all forms of FOT, Q is measured at the mouth, however p can be measured at either the mouth or the chest wall. In the case of p being measured at the chest wall, the calculated impedance is known as the transfer impedance, whilst if both p and Q are measured at the mouth then the calculated impedance is called the input impedance. In the early development of FOT the transfer impedance was measured [26], however in order to measure p at the chest wall the patient must be enclosed in a sealed box with only their head protruding from the box whilst they breathe through a tube. It is for this reason that p is now almost exclusively measured at the mouth as this is far more comfortable on the patient. All values of p described in these studies refer to the pressure at the mouth and therefore all values of Z refer to the input impedance.

The setup for an FOT device for measuring input impedance can be seen in Figure 1.5. In this example device, the forced excitations are produced by a loudspeaker that can produce pressure waves at multiple frequencies simultaneously; thus implementing the idea of effectively using a waveform containing multiple frequencies that was developed by Lutchen et al. in 1993 [29]. These travel to the patient though the cross shaped mouthpiece, containing a filter for patient safety, with the pressure and flow at the patients mouth measured using a pneumotachograph. A pneumotachograph measures the flow by measuring

the pressure at two points separated by a small distance. As the difference in pressure between these points is proportional to the flow rate a measurement can be made. A connection to the atmosphere is also necessary to allow the patient to breathe normally for the duration of the measurements. This connection must have an impedance high enough to prevent the pressure waves from leaking out of the system but not too high otherwise it would prevent the patient from breathing. The signal waveform produced by the loudspeaker can be synthesised by a computer to contain the desired frequencies.

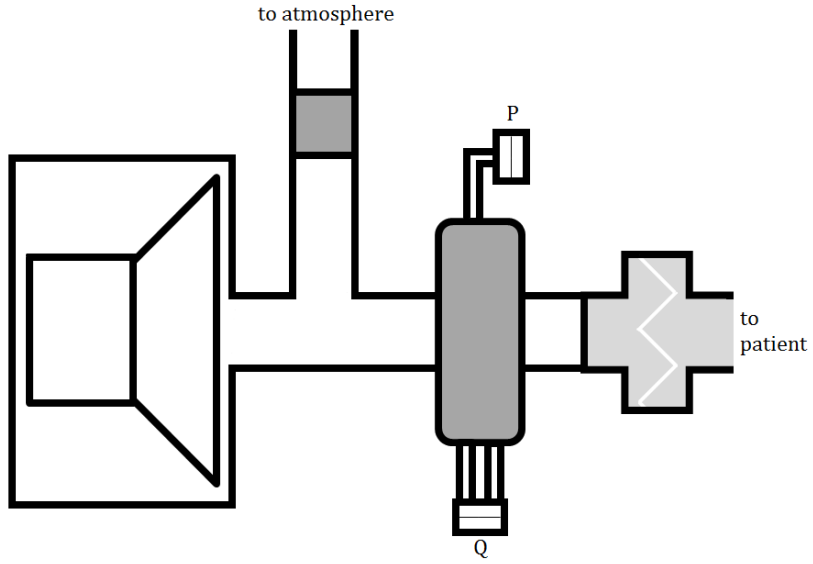


Figure 1.5: Schematic diagram of an FOT machine for measuring input impedance where p and Q represent the measuring of pressure and flow respectively.

There are two types of waveform commonly used in FOT of which the simplest form comprises of a series of superimposed sinusoidal waves that are produced continuously. Alternatively, the oscillations can be produced in the form of a series of impulses containing multiple frequencies making the waveform pulsatile

rather than continuous [30]. This method is called Impulse Oscillometry (IOS) to distinguish it from conventional FOT methodology. Commercial devices utilizing both FOT and IOS are available however research into how comparable the results from the two methods of FOT and IOS has been, and is still, ongoing [31, 32] with a short study on comparing the two methods included in this thesis.

It is desirable to minimise the peak pressure of the multisine waveform applied to the patient. Peaks in the waveform are cause by the superposition of the different sinusoidal waves combined int the waveform. The peak pressure during FOT was minimised by applying a different phase shift to each of the frequencies included in the waveform.

Respiratory Impedance

One of the most clinically important aspects of respiratory impedance is that it is frequency dependent [26, 33]. This is due to the different properties of the different regions of the respiratory system; for example the trachea is a large stiff airway whilst alveolar sacs are small and spongy and so these regions have different acoustic impedances. This allows different regions of the lungs to be evaluated based on the frequency (which is in turn related to the penetration depth) of the applied pressure waves. This can be done by using individual frequencies one at a time, or by combining a range of frequencies into one waveform as described previously. Different disease states affect separate regions of the lung by varying amounts and so the frequency dependence of respiratory impedance can be used to assess lung condition.

In the case of constant flow through a rigid tube, the impedance to flow of the tube is entirely resistive. However in the case of a fluctuating flow rate through a pliable tube, the impedance will have an additional reactive component. As

the airways of the respiratory system are pliable and the pressure waves supplied during FOT are non-constant, respiratory impedance comprises both a resistive component and a reactive component [34]. The resistive component refers to the drag on the pressure waves by the airways and is dependent on properties such as the diameter and length of the airway as well as the viscosity of the air flowing through the tube. Airways disease can cause obstruction and narrowing of the airways causing an increase in the resistive component of respiratory impedance. A highly resistive tube results in a low flow rate through the tube.

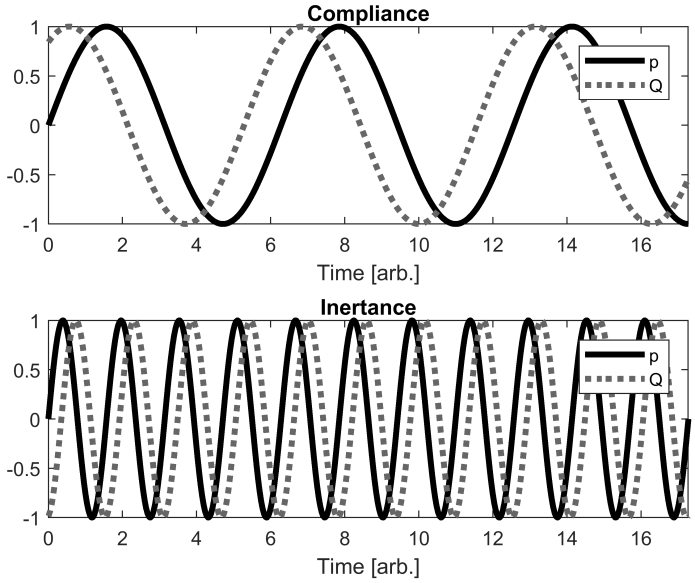


Figure 1.6: Graphical representation of the phase difference between p and Q caused by compliance and inertance respectively

The reactive component is caused by two factors: compliance and inertance. Compliance, the inverse of elastance, is the property of a material which refers to the materials ability to resist distension. The energy required to distend the tissue of the airways is stored potentially in the tissue and released later. In a

fully rigid tube there is no distension and so there is no element of compliance in the impedance of the tube. The compliance causes Q to lead p as shown in Figure 1.6. As p and Q are no longer in phase, the reactive component gives impedance an imaginary component. Compliance dominates at lower frequencies [27]. The inertance of the lungs refers to the initial effort required to accelerate the mass of air in the airways. There is therefore no component of inertance in the impedance of a tube for the case of constant flow. As energy is stored kinetically in the air, Q starts to lag behind p as shown in Figure 1.6. The higher the frequency the more frequently the air in the airways will be accelerated by the pressure waves and so the inertance dominates.

Measured Parameters

As compliance causes Q to lag behind p and inertance causes Q to lead p with both components being frequency dependent, there exists a frequency at which the effects of inertance and compliance are perfectly balanced with Q and p being perfectly in phase. In this situation the reactive component of respiratory impedance has a value of zero. This frequency is the resonant frequency (f_{res}) of the lungs. For a healthy person this has a typical value of between 5 and 15 Hz, increasing as lung function worsens.

By measuring respiratory impedance at multiple frequencies an impedance curve can be plotted with a real part (the resistive component) and an imaginary part (the reactive component). Not only can this be used to find the value of f_{res} but it can also be used to evaluate another FOT parameter: the reactance triangle (A_X). This is defined as the magnitude of the integral of the reactive component of respiratory impedance between 5 Hz and f_{res}. Figure 1.7 shows a typical respiratory impedance curve for a healthy person. It can be seen that in this case, f_{res} has a value of approximately 9 Hz. The reactance triangle has been highlighted in blue.

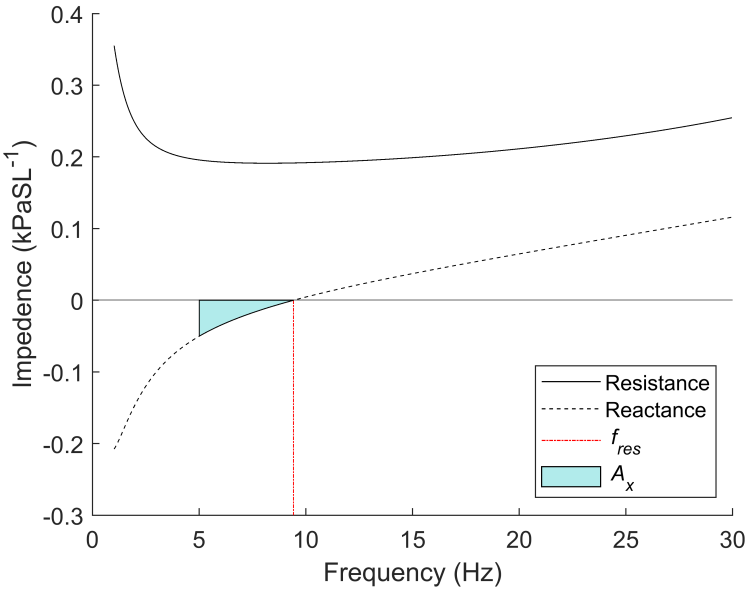


Figure 1.7: A typical respiratory impedance curve from a healthy person with f_{res} and A_X highlighted.

Another commonly used FOT parameter is the value of the resistive component at 5 Hz (R_5) minus the value of the resistive component at 20 Hz (R_{20}). The significance of this value is that the lower frequency of 5 Hz should give information about a larger portion of the lung as the lower frequency pressure waves are more penetrating whilst the higher frequency impedance is the impedance of the larger upper airways. Therefore the resistive component of the smaller airways can be identified by subtracting R_{20} from R_5. This parameter is denoted $R_5 - R_{20}$.

There are also several other features of these impedance curves that vary between patients such as the gentle increase in resistance with frequency at the higher end of the frequency range. These features can be quantified by fitting a theoretical model to the data. Numerous models have been proposed over

the years starting with Dubois. However his proposed model was demonstrated to be unsuitable for the time due to a lack of data that could be acquired with contemporary techniques [35]. More recently there have been new models developed that allow other parameters to be evaluated [25, 36, 37].

FOT/IOS has the significant advantage of not requiring large amounts of patient cooperation. This is because the oscillations are applied during normal tidal breathing, making FOT a patient friendly test. One key disadvantage of FOT is a lack of unifying standards for calibration as FOT is still in the research stage. There is also dispute over aspects of FOT such as the most useful frequency range to interrogate, and the main parameters to measure with the technique. This is being addressed with the use of parameters such as $R_5 - R_{20}$ (the difference in the resistive component of respiratory impedance at 5 Hz and 20 Hz) and the reactance triangle (the magnitude of the integral of the reactance curve between 5 Hz and the resonant frequency). There are no known side effects to FOT/IOS.

Body Plethysmography

Both spirometry and FOT provide information about obstructive airways disease however they provide far less information about restrictive airways disease (this is particularly true for spirometry). Body plethysmography is a common clinical lung function test that provides information about lung volume as well as the flow rate of breathing. Therefore body plethysmography is often used to assess restrictive lung disease rather than obstructive disease. As well as this, body plethysmography can also be used to determine respiratory flow resistance which is the resistive component of the respiratory impedance as measured using FOT [38].

"Plethysmography" refers to the measurement of a change in volume in an organ or region of the body. In the case of body plethysmography, the change in volume due to inspiration is evaluated by measuring the change in pressure this causes in a sealed container. During body plethysmography the patient is placed within a sealed container with a mouthpiece containing a tube connecting to atmosphere and a shutter. The patient is attached to the mouthpiece whilst wearing a nose-clip and instructed to breathe normally whilst the shutter is open. The shutter is then closed and the patient is instructed to perform a forced inhalation to maximum capacity against the shutter. This increases the volume of the lungs causing a decrease in the pressure of the air at the mouth which can be measured by the mouthpiece. Simultaneously the volume of air within the sealed contained decreases due to the increase in lung volume, causing an increase in the air pressure within the box which can also be measured. The patient is then asked to perform a forced exhalation against the shutter which causes the opposite effect to occur with respect to the pressures at the mouth and within the box. The shutter is then opened and the patient is free to breathe normally. As the change in pressure cause by the forced inspiration and exhalation against the shutter is proportional to the change in lung volume, the ratio between the pressure measure at the mouth and in the box can be used to calculate a value for FRC.

The patient may then be asked to perform a vital capacity manoeuvre, which consists of the patient performing a full exhalation, followed by a maximum inhalation, followed by a maximum exhalation. This is all done with the shutter open to allow the flow rate to be monitored. The vital capacity manoeuvre on its own allows for the calculation of FVC however using the previously acquired information about the FRC of the patient, the values for RV and TLC can also be calculated. Body plethysmography is therefore used to assess conditions such as asthma and COPD as well as other restrictive and obstructive lung diseases.

Although body plethysmography provides an abundance of physiological data, the process is comparatively complicated compared to spirometry and requires an even greater amount of patient cooperation. This disadvantage is exacerbated by the discomfort that arises from the measurements occurring within a sealed container. The box is designed to be transparent in order to reduce the feeling of claustrophobia but this does not remove the problem entirely. There are no significant side effects to body plethysmography although forced breathing manoeuvres can cause dizziness.

Gas Dilution/Multiple Breath Washout

An alternative to body plethysmography as a method of assessing lung volume (and therefore restrictive lung disease) is gas dilution. The gas dilution procedure requires the patient to breathe normally through a mouthpiece thus reducing the level of required patient cooperation. A known amount of a tracer gas is then introduced to the patient through the mouthpiece during inhalation after which the concentration of that gas found in the patients subsequent exhalations is monitored. As the volume of tracer gas inhaled is significantly smaller than the volume of air within the lungs, a dilution effect will take place. By observing the concentration of the gas for each exhalation this dilution effect can be quantified and the volume of the lungs calculated. The tracer gas used in gas dilution must be inert and not absorbed by the body in any significant quantity, with commonly used tracer gases including nitrogen, helium and sulphur hexafluoride. Gas dilution is used to observe restrictive airways diseases such as CF and IPF.

The gas dilution method can be taken a step further by performing a washin or washout test to provide additional physiological information [39]. A washin test is where the patient breathes in a a tracer gas whilst all exhalations are monitored. In this case there is no fixed amount of tracer gas but rather the

patient continues to breathe in a mix of tracer gas and air (or 100% tracer gas) until the exhaled gas mix reaches equilibrium. This provides information on the number of breaths required to replace the gas in the lungs with new gas (be that tracer gas or air as would be the case in normal life). Once equilibrium has been achieved a washout test can be performed where the patient no longer breathes in a tracer gas mix but instead breathes normal air. The concentration of tracer gas found in each exhalation is monitored and should decrease exponentially as the gas in the lung is recycled. This process continues until the concentration of the tracer gas present in an exhaled breath has reached 1/40 of the concentration of the initial mix. It is not essential to perform both a washin and washout test as each test can be performed separately. As with gas dilution, multiple breath washin or washout utilizes a non-toxic gas such as nitrogen, sulphur hexafluoride (SF_6) or 100% oxygen. A typical SF_6 washin and washout trace is shown in Figure 1.8.

One of the main parameters measured is the lung clearance index (LCI). The LCI of a patient is the ratio between the total expired volume of gas during the washout, and the FRC of the patient. This ratio describes the average number of breaths required to wash out the tracer gas to 1/40 of the initial concentration and increases with increased disease severity. One key advantage of LCI is its sensitivity towards measuring small airways disease, a feature that is not observable using spirometry. Furthermore multiple breath washout requires no significant breathing manoeuvres which reduces patient cooperation and therefore increases the reliability of the test. However multiple breath washout is a significantly slower process than spirometry. There are no significant side effects to multiple breath washout.

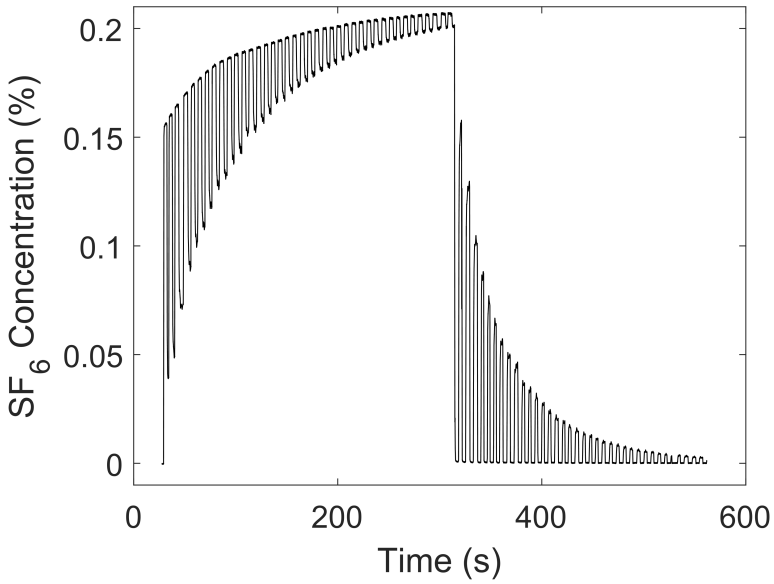


Figure 1.8: A typical sulphur hexafluoride (SF_6) washout trace demonstrating both the washin phase from 0 to ∼300s followed by the washout phase from ∼300 to ∼550s.

1.2.3 Lung Imaging

Lung function tests are quick and inexpensive methods of providing physiological information about a patient's respiratory system however they provide limited information about the anatomy of the patients lungs. For certain conditions, anatomical information is important in order to determine either the type or severity of a disease. For example if a patient has obstructed airways it is useful to know whether these obstructions have a fixed location or whether they move around the lung. This cannot be determined by lung function tests but can be determined using lung imaging techniques.

There are two main types of medical imaging modality: ionising and non-ionising. Ionising imaging utilises high energy radiation to penetrate the body

to observe internal structures using either an external source (planar x-ray and CT) or an internal source (SPECT and PET). Medical imaging using an internal ionising radiation source is known as nuclear medicine. Non-ionising medical imaging modalities use lower energy mechanisms to image the body using methods such as high frequency sound (ultrasound) or high strength magnetic fields and radio frequencies (MRI). There are benefits and disadvantages for each of the different imaging modalities requiring different disease states to be investigated using the modality that best suits the situation.

Planar X-ray

Planar x-ray is the simplest and oldest medical imaging modality having been first discovered in 1895. The principle of planar x-ray is that high energy radiation passes through the body with some amount of the x-ray beam being attenuated. The remaining x-rays are detected by a detector on the opposite side of the body. The energy of the x-rays is such that the main forms of beam attenuation come from scattering and absorption. The rate of scattering and absorption is dependent of several environmental factors, the most significant of which is the density of the medium through which the x-ray is travelling. As a result, denser anatomical features, such as bones, attenuate more x-rays than less dense features, such as soft tissue, and therefore the denser object forms a "shadow" of reduced signal on the radiograph produced. By inverting the image a 2D map of density throughout the body can be formed. As the x-rays penetrate the whole body, limited information is provided on the depth of observed features.

The most common use of planar x-ray is to investigate bones for fractures, breaks and other damage as bone is significantly denser than soft tissue; however planar x-ray can be used to look at other features. With regard to lungs, planar x-ray has historically been used to observe pneumonia and bronciolitis [40] as

well as CF in more recent studies [41]. In these cases it is the abnormalities around the lung that is being observed rather than the airways of the lung itself. With pneumonia the fluid in the lung is observed whilst for CF it is the fibrosis that is seen. There is a difficulty in imaging the lungs that arises from the fact that they should be filled exclusively with air, a poor attenuator of high energy radiation. It is therefore the case that a healthy pair of lungs appear as a blank black region on an x-ray image. This difficulty in imaging lungs is not exclusive to planar x-ray but is present in all major imaging modalities.

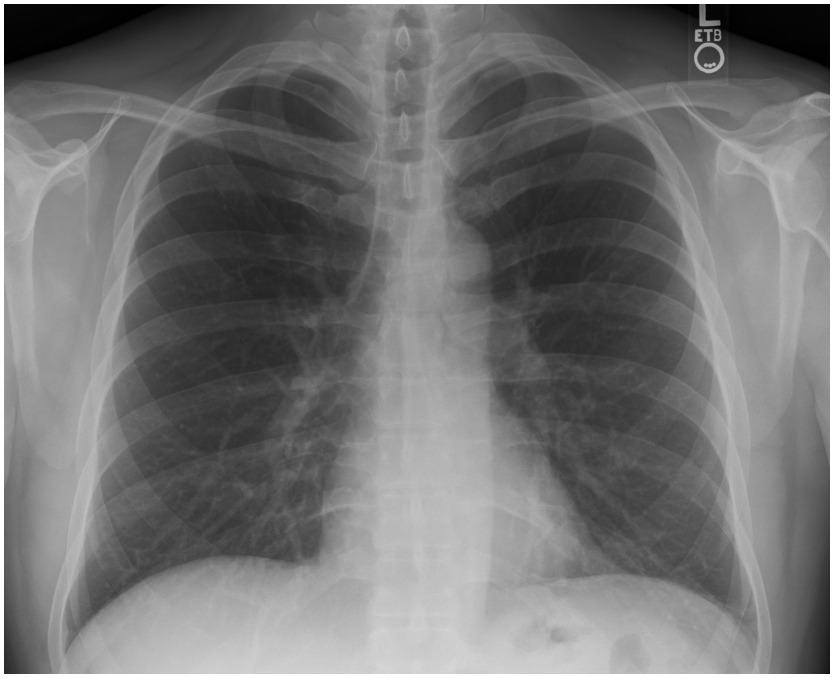


Figure 1.9: Chest x-ray of a healthy human with the heart, ribcage and vasculature of the lungs clearly visible. Source: Wikimedia Commons.

Figure 1.9 shows a chest radiograph of a healthy human. The dense bone structures of the skeleton are clearly visible in white with good resolution seen in the spine, ribcage and clavicles. In contrast the soft tissue in the shoulder and

neck region is blurred with no visible difference in contrast between the muscle, fat and other soft tissues. Another visible feature is the blurred outline of the heart and sternum which can be seen in the centre of the image. Overall the image is dominated by the lungs which appear as two dark regions as previously discussed with the trachea and its bifurcation visible behind the sternum. The thin white web-like structure that can be seen throughout the lungs is the surrounding blood vessels that are necessary for efficient gas exchange rather than features of the airways within the lungs. Figure 1.9 highlights the difficulty in obtaining detailed anatomical information about the airways.

As planar x-ray uses ionising radiation there is an increased risk of contracting cancer associated with each scan. However the dose from a typical single chest x-ray in the UK is 0.02 mSv (equivilent to the dose recieved from three days exposure to natural background radiation in the UK) so the cancer risk is minimal [42]. There are no other known significant side effects of planar x-ray. Overall, a planar x-ray is a quick and inexpensive method of providing anatomical data of large structures (e.g. bones), however it has low contrast resolution with regard to soft tissue and provides extremely limited information about the depth of any observable features. These issues can be addressed by using x-ray computed tomography (CT) imaging.

X-ray CT

X-ray CT operates on the simple principle that a composite 3D image can be formed from multiple planar x-ray images taken from different angles (or projections). These separate images care combined using a computer, hence the name computed (or computerized) tomography. In practice the x-ray tube (the source of the x-rays) is continuously rotated around the body whilst the detector array rotates around the body at the same rate but on the opposite side. This produces a detailed 2D image of a slice of the patient in which the

slice has a known thickness. The patient can then be moved in relation to the x-ray tube and detector array in order to image the next slice of the patient. By repeating this process the entire body can be broken up into sliced images allowing for a 3D reconstruction of objects within the body. The thickness of these slices can be adjusted by adjusting the collimation of the x-ray beam.

An alternative method to imaging the patient in discreet slices is to continually pass the patient through the x-ray beam as it rotates so that the beam follows a helical path along the body. This is known as helical or spiral CT and has advantages such as shorter examination times and improved visibility of vascular structures. On the other hand, helical CT also has certain disadvantages including unique artifacts [43].

In order to provide easily readable anatomical information from the raw data measured using x-ray CT, an image must be reconstructed. Initially the raw data consists of a series of 1D arrays from each projection. These can be displayed in sequential order producing an sinusoidally undulating image known as a sinogram. Alternatively these data can undergo a process called back projection where each projection is rotated by the angle of the beam and then superimposed on top of each other producing a blurred image of the object. The blurriness of this image can improved by applying a filter to the projections to sharpen the image by detecting any edges and creating negative pixels elsewhere to reduce noise. Different filters can be used in filtered back projection with different outcomes. A balance needs to be struck between filtering out noise to produce an image with high spatial resolution, and inadvertently removing anatomical information. Another option for image reconstruction is to use an iterative reconstruction algorithm where an initial "guess" of the image is made (usually using back projection) before refining the image over numerous iterations. Each refinement is done by assessing the possible variation of the

signal due to noise and adjusting the image accordingly. The refined image is then compared to the initial "guess" to see if there is an improvement. This process is more computationally expensive but provides better quality images and can factor in prior knowledge of the object imaged (for example, that the lungs are a certain shape).

All x-ray CT images are taken in the axial plane as the patient must pass through the gantry containing the x-ray source and detector. As the bore of the gantry is as small as possible to minimise the distance between the source and the detector, the patient must pass through the gantry either head-first or feet-first. However the resolution of an x-ray CT image is high enough that images can be reconstructed in the other planes if required.

One of the main benefits of x-ray CT that makes it such a well used imaging modality is the incredibly high spatial resolution of the images as shown in Figure 1.10 which shows an axial x-ray CT image of the chest of a healthy female. The lungs are visible as two large dark regions with the heart and major blood vessels in-between. The three dark vessels that can be seen in the centre of the image are the two bronchi and the oesophagus (the oesophagus being in the middle and more posterior). As with planar x-ray there is very little detail to the lungs aside from the network of blood vessels that are clearly visible and demonstrate the remarkable spatial resolution provided by CT. However although the spatial resolution is good, it is still not high enough to resolve the any small structural features of the lungs such as obstructed airways.

X-ray CT also has low contrast resolution due to the relative similarities of the absorption rates of soft tissues at the energy range used. This is noticeable in the tissue surrounding the thoracic cavity where it is difficult to differentiate between muscle, fat and other soft tissue. It is therefore only fibrosis of the lungs or, in the case of pneumonia, fluid within the lungs that can be detected

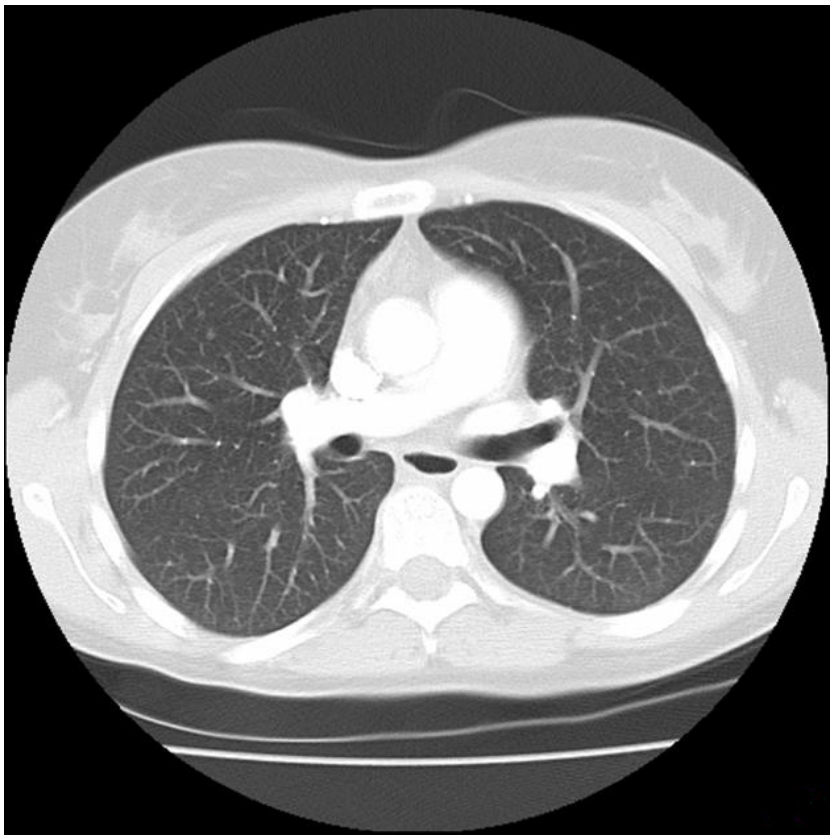


Figure 1.10: Axial x-ray CT slice of a healthy female with lungs, heart, major blood vessels, bronchi and oesophagus visible. Source: radiopedia.org.

using x-ray CT. The issue of low contrast resolution can be reduced through the application of an external medium (called a contrast agent) with a significantly different absorption rate to that of the surround tissue thus enhancing the contrast resolution. Examples of contrast agents used in x-ray CT include iodine for imaging blood vessels and barium for imaging the digestive tract. The use of contrast agents can be further developed by taking a subtraction image. This is where the same region is imaged twice, once before and once after a contrast agent is introduced. The first image is then subtracted from the second image leaving only the object affected by the contrast agent. The

use of contrast agents allows physiological information to be acquired from an otherwise purely anatomical imaging modality.

X-ray CT delivers a significantly larger radiation dose than planar x-ray with a typical dose of 8 mSv for a chest CT scan [42]. This is the equivalent of 3.6 years of exposure to UK background levels and is therefore creates a not insignificant increased cancer risk meaning x-ray CT should not be performed on pregnant women. There are also certain diseases, such as ataxia telangiectasia, where patients are more susceptible to radiation damage and therefore cannot be scanned using this modality [44].

MRI

The two main disadvantages of x-ray imaging (both planar and CT) are the lack of contrast resolution in soft tissue and the use of ionising radiation. Nuclear Magnetic Resonance Imaging (MRI) is a good alternative as it provides very high contrast resolution in soft tissue and uses non-ionising radiation.

Nuclear magnetic resonance (NMR) utilizes the fact that many nuclei in the body have charge and spin and therefore an inherent magnetic moment. Ordinarily the direction of these magnetic moments is randomly distributed throughout the body such that there is no net magnetic moment. However when the body is placed within a large static magnetic field (B_0), the magnetic moments of the nuclei within the body align with B_0 resulting in a net nuclear magnetisation along the direction of the B_0 field. It is very difficult to measure this net magnetisation as the strength of the B_0 field is orders of magnitude larger and dominates the signal. However the magnetic moment of each nucleus precesses with a frequency that is dependent on factors including the atomic number of the nucleus, the strength of B_0, and the environment of the nucleus. If a secondary weaker oscillating magnetic field (a radio frequency, or r.f., pulse) is applied to

the body at the same frequency as the precession frequency of the nuclei then resonance will occur and the net magnetic field will be tipped out of line with B_0. This produces a net oscillating magnetic field in a different direction to B_0 which can be detected using a receive coil. As the frequency of the r.f. pulse and the strength of B_0 are known it is possible to calculate the environment of the nuclei causing the signal. For example it is possible to differentiate between hydrogen nuclei (i.e. protons) in fat and in water.

NMR is an effective method of identifying the components parts of an unknown sample; however it provides no information about the relative positions of the component parts. In order to form an image, magnetic gradient fields are applied. These change the strength of B_0 along a given direction which in turn applies a gradient with position of the precession frequency of the nuclei. By applying gradients in three dimensions at different moments in relation to the r.f. pulse a 2D image of a slice of the body can be formed. Slices of the body can be imaged sequentially to create a 3D map of the body in a similar manner to x-ray CT.

The most common form of MRI is proton MRI which forms an image from ^{1}H nuclei. This is extremely abundant throughout the body as it is present in water, fat, muscle and most other organs and tissues which allows for the effective imaging of most regions of the body. MRI has become a powerful tool in brain imaging due to the high contrast resolution in soft tissue but is also used to scan other parts of the body, particularly in cases where a patient cannot receive an x-ray CT scan. However the lungs are filled with air which contains a relatively low abundance of ^{1}H and so appears as a dark region of low signal in an MRI scan. Without the application of a contrast agent it is only possible to observe extreme fibrosis or fluid build-up with the lung using conventional MRI due to issues with spatial resolution. However recent developments in ultrashort

echo time (UTE) MRI has increased the spatial resolution of pulmonary MRI to a comparable level with x-ray CT [45].

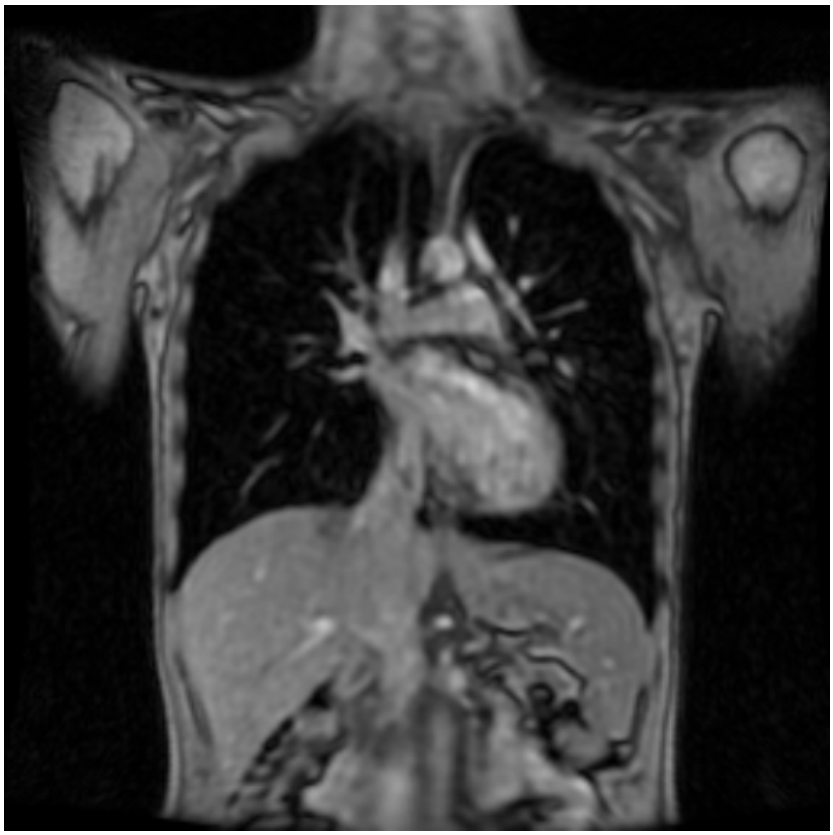


Figure 1.11: Coronal MRI slice of a healthy male with lungs, heart, major blood vessels, and liver visible.

Typically MRI provides anatomical rather than physiological information with the notable exception of functional MRI (fMRI) which looks at the concentration of oxygen in the blood in the brain during different stimuli (a technique called BOLD-contrast imaging) [46, 47]. A typical MRI slice of the chest is shown in Figure 1.11. This highlights the necessity for a contrast agent in order to gain useful information about the lung condition. Gadolinium is the most

commonly used contrast agent for proton MRI to provide physiological information, however a gaseous (and non-toxic) contrast agent is required to image the lungs. One option is to use an isotope of a noble gas such as ^{3}He or ^{129}Xe. However the density of gas is low in comparison to the liquids and solids that make up the body resulting in a gaseous contrast medium giving a small NMR signal unless the gas is hyperpolarised (HP). HP gas MRI provides physiological information about airway obstructions and trapped air within the lungs that can be combined with anatomical information from a proton scan taken immediately before the HP gas scan. This information can be used to assess the condition of lung diseases such as asthma, COPD, CF and IPF.

Oxygen can also be used as a contrast agent to assess lung function in a process known as oxygen-enhanced MRI (OE MRI). In this process the oxygen alters the signal from the protons in the water of the lung. By comparing a series of images taken whilst the patient breathes air with images taken whilst the patient breathes pure oxygen a subtracted image can be formed [48]. This will show the regions that have been ventilated by the oxygen allowing for obstructions to be observed and monitored. One key advantage of OE-MRI is that the patient is not required to hold their breath during the scan (as is the case during HP gas MRI) which allows for the scan to be performed on paediatric patients.

MRI uses high strength magnetic fields to take an image and is therefore unsuitable for patients with pacemakers or metal objects within the body including foreign bodies (such as piercings, shrapnel etc.), extensive tattoos or artificial joints/surgical clips (unless these are MR safe). Scan times can also be long requiring the patient to be in the bore of the magnet for tens of minutes making MRI unsuitable for patients with claustrophobia. MRI is also a loud process requiring the patient to wear ear defenders for the majority of scanners making MRI unsuitable for patients with tinnitus. However, as previously mentioned,

MRI is non-ionising and so presents no cancer risk.

Nuclear Medicine

Nuclear medicine is an imaging modality that provides physiological data rather than anatomical information which is primarily provided by planar x-ray, x-ray CT and MRI. The principle of nuclear medicine is similar to that of x-ray (both planar and CT) with high energy gamma rays passing through the body to a detector however an internal radiation source is used in nuclear medicine instead of an external source. A radiopharmaceutical is used as a source which consists of a radioactive isotope bound to a molecule that will be selectively absorbed by a specific region within the body. For example, the most common application of nuclear medicine is to monitor cancer by binding a gamma emitter (such as ^{99m}Tc) to a molecule that is absorbed by a tumour at a higher rate than any other feature of the body resulting in a high concentration of radioactive material in the tumour. A detector placed on the outside of the body is the used to create an image of the distribution of the radiopharmaceutical within the body highlighting regions of interest such as tumours. Computed tomography can be carried out by by rotating the detector around the body to produce a 3D image of the position of the radiopharmaceutical.

The two most common forms of nuclear medicine are Single-Photon Emission Computed Tomography (SPECT) and Positron Emission Tomography (PET). A gamma emitter is used as the radionuclide in SPECT with a gamma camera used as the detector as described previously. PET is a more complicated process using a β^- emitter as the radionuclide. The emitted positrons interact with electrons in the region of the radiopharmaceutical emitting two gamma rays in exactly opposite directions which are detected by a ring of detectors surrounding the patient. The position of the initial annihilation event can be calculated by comparing the difference in time between the two detection inci-

dents. By measuring repeated annihilations a 3D map of the concentration of the radiopharmaceutical used can be created [49].

One issue with nuclear medicine is that the images produced can be amorphous due to their purely physiological nature. This can lead to difficulties in interpreting the image if there are no clear anatomical features within the image. This issue has lead to the development of fusion images where two modalities are used in quick succession (e.g. PET/CT or PET/MRI). The physiological information from the nuclear medicine scan is the overlaid on top of the anatomical information provided by a different imaging modality, resulting in an image that is easier to interpret. An example of a PET/CT image is shown in Figure 1.12. Although nuclear medicine has traditionally been, and still is primarily, used for monitoring cancer it can also be used to monitor lung diseases such as CF, Pneumonia, Tuberculosis and other infectious diseases (as seen in Figure 1.12). However the use of nuclear medicine in the monitoring of non-oncological diseases is still very much in the research stage.

As with planar x-ray and x-ray CT there is an associated cancer risk with all nuclear medicine imaging as ionising radiation is used. Due to the variety of modalities, scan types and radionuclides used there is a large range in patient dose, ranging from 0.1 mSv (equivalent to 2.4 weeks of natural background radiation) up to 18 mSv (equivalent to 8 years worth of exposure to natural background radiation) [42]. Consequently nuclear medicine techniques are not advised for pregnant women or children. This large radiation dose can be used as a form of treatment instead of diagnosis in certain situations. For example iodine is preferentially absorbed by the thyroid gland and so a radioactive isotope of iodine can be used to destroy any remaining traces of the thyroid gland after a thyroidectomy.

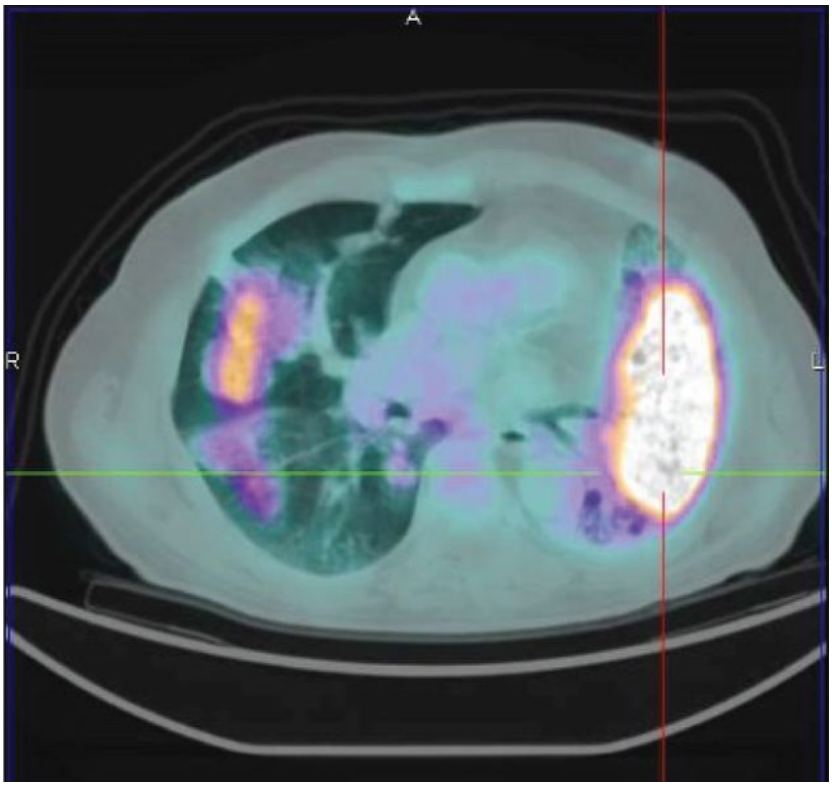


Figure 1.12: Axial PET/CT image of 71-year-old male with diffuse pulmonary infection. Infections parenchymal alterations show an increased fluorodeoxyglucose uptake. Image taken from Capitanio et al. [50].

1.3 Conclusion

The respiratory system is a necessary yet complex system that works in tandem with the circulatory system to provide a source of oxygen to the entirety of the body whilst simultaneously removing waste. This system consists of a large network of airways that branch from the trachea. The delicate nature of this network of smaller airways leaves the respiratory system vulnerable to damage through disease despite the defence mechanisms of the mucus layer and epithelial cells. A selection of these potential diseases has been described in Section

1.1.2.

There are numerous methods of assessing the condition of the lungs, both anatomically and physiologically. The large variety of airways diseases warrants a large number of observation techniques to diagnose and monitor these various diseases depending on the patients circumstances. Research is being done into all aspects of lung function tests to identify the best treatments for specific conditions. This thesis will particularly focus on one lung function test (FOT) and one lung imaging technique (HP gas MRI) drawing comparisons to other more commonly used tests such as spirometry and x-ray CT.

The current main method of assessing lung function in a clinical setting is spirometry, with body plethysmography and gas washout available as options if further investigation is required. One assessment that can be performed using spirometry is bronchodilator (BD) reversibility testing. This is done by taking spirometric measurements before and after the inhalation of short-acting beta agonists (SABA) which increase large airway calibre, which improves airflow, as well as reducing obstruction in smaller airways. This effect is why SABA are used to manage and treat asthma which, unlike COPD, is considered to be a reversible condition. In COPD, SABA use may reduce dynamic hyperinflation by reducing the volume of air trapped within emphysematous lungs, which in turn can improve symptoms [51]. Although spirometry is effective at measuring an improvement in airflow, it has difficulties in measuring reductions in both small airway bronchoconstriction and dynamic hyperinflation, both features that can be measured using Forced Oscillation Technique (FOT) [52, 53]. It has been noted that there is overlap between the features of asthma and COPD [54] leading to the recent introduction of the term asthma-COPD overlap syndrome (ACOS) [55, 16] which highlights the importance in obtaining more information about the smaller airways of patients with ACOS.

Although medical imaging is well developed and established for most areas of the body, it is still difficult to image the lungs. This is due to the rarefied nature of the tissue within the lungs. As lung disease affects so many people it is important to develop lung imaging techniques that will be able to provide more diagnostic information on the previously described conditions. The diverse nature of HP gas MRI (in that it can be used for physiological and anatomical measurements) is particularly useful in this situation.

Chapter 2

Forced Oscillation Technique

2.1 Introduction

The Forced Oscillation Technique (FOT) is a non-invasive lung function test that is currently not common practice in a clinical setting, but is instead a research technique. As with spirometry, a patient undergoing FOT will breathe (whilst wearing a nose-clip) into a mouthpiece connected to a device via a tube. However, with FOT, the patient would not be asked to carry out any forced breathing exercises, only tidal breathing. Pressure waves of varying frequencies are applied to the patients airways along the same connecting tube. The pressure and flow rate of air at the patients mouth are then measured in order to evaluate the impedance of the respiratory system to the pressure waves.

Two studies are presented in this thesis: a phantom study and a patient study. The phantom study had three aims. These were to 1): to establish the validity of the Nottingham FOT system; 2): explore how physical changes to

the resistance and compliance of a phantom affected FOT measurements; and 3): compare the Nottingham FOT system to two commercial systems at another site. The second aim was achieved using a phantom lung comprising of a replica of the first seven generations of the airways housed in a cylinder with a rubber membrane at the base. The phantom used had 72 airway openings that could be obstructed using an adhesive sealant to simulate airway obstruction whilst the elasticity of the rubber membrane could be altered to investigate the effects of lung compliance on measured FOT parameters. The other devices looked at in the final part of the phantom study were housed in Glenfield Hospital, Leicester. A secondary aim of this part of the study was to investigate the differences between continuous and impulse based FOT.

The patient study was undertaken to investigate the effects of SABA on measurements of lung condition using FOT, with a focus on comparing the disease states of asthma and COPD using both spirometry and FOT. This was done to ascertain the value of FOT in a clinical setting as a source of information about lung condition that would be unavailable using current pulmonary function tests. Identifying patterns of FOT response irrespective of disease labels may therefore be useful in tailoring medication use to disease phenotype [56]. The main aims of the study were to 1): confirm that FOT can distinguish between disease states in a similar manner to spirometry; 2): establish the differential effects of a BD on specific FOT parameters, irrespective of disease label; and 3): establish whether patients with spirometric bronchodilator reversibility had BD response in FOT parameters.

2.2 Theory

2.2.1 The Forced Oscillator

The measurement of the acoustic impedance of the lungs using FOT can be modelled by considering the lungs as a Helmholtz resonator with the lungs acting as the cavity and the upper respiratory tract acting as the neck. In this situation, the elasticity of the lungs is modelled by the compressibility of the air within the cavity. If an external force acts on this damped oscillator system then the result will be a forced oscillator in which the pressure at the aperture, p, and the volume of gas displaced by the oscillations, V, are related by

$$p = EV + R\dot{V} + I\ddot{V}, \tag{2.1}$$

where E is the elastance, R is the resistance and I is the inertance. These can be evaluated using

$$E = \frac{\gamma p_c}{V}, \tag{2.2}$$

$$R = \frac{8\eta l}{\pi r^4}, \tag{2.3}$$

$$I = \frac{\rho l}{A}, \tag{2.4}$$

where p_c is the pressure in the cavity, γ is the adiabatic index, η is the viscosity of the gas within the system, l is the length of the oscillating mass in the neck, r is the radius of the neck, and A is the cross-sectional area of the neck. When the system is being driven by a sinusoidal oscillation the driving force, equation 2.1 can be solved for

$$V = V_0 e^{i(\omega t - \phi)} \tag{2.5}$$

such that

$$p = EV_0 e^{i(\omega t - \phi)} + Ri\omega V_0 e^{i(\omega t - \phi)} - IV_0 \omega^2 e^{i(\omega t - \phi)} \tag{2.6}$$

with

$$p = p_0 e^{i(\omega t + \phi)} \tag{2.7}$$

where ω is the angular frequency of the oscillations, t is time and ϕ is the phase angle of the displacement. By substituting from equations 2.6 and 2.7 into

$$Z = \frac{p}{Q}, \tag{2.8}$$

as $Q = \dot{V}$, it holds that,

$$Z = \pm \frac{p_0 e^{i(\omega t + \phi)}}{i\omega V_0 e^{i(\omega t - \phi)}}, \tag{2.9}$$

in which the sign change is dependent on the sign of ϕ which can be calculated using

$$\phi = \tan^{-1}\left(\frac{R\omega}{E - I\omega}\right) - \phi_d, \tag{2.10}$$

where ϕ_d is the phase angle of the driving force. V_0 is the amplitude and is described using

$$V_0 = \frac{p_0}{I\sqrt{\left(\omega_0^2 - \omega^2\right)^2 + 4\Gamma^2 + \omega^2}}, \tag{2.11}$$

with

$$\Gamma = \frac{R}{2I}, \tag{2.12}$$

and the resonant angular frequency ω_0 is given by

$$\omega_0 = \sqrt{\frac{E}{I}}. \tag{2.13}$$

The acoustic impedance of a driven Helmholtz resonator is shown in Figure 2.1 which shows Z for an adiabatic system (in which $\gamma_{air} = 1.4$) and an isothermal system (in which $\gamma_{air} = 1$) against frequency. This highlights the difference between an adiabatic and an isothermal system where a noticeable difference can be seen in f_{res}. This is due to the way that f_{res} is proportional to $\sqrt{E}$ which is in turn directly proportional to $\sqrt{\gamma}$. As a result, for an air filled system, there can be a shift in f_{res} of up to 18% depending on whether the system is adiabatic or isothermal.

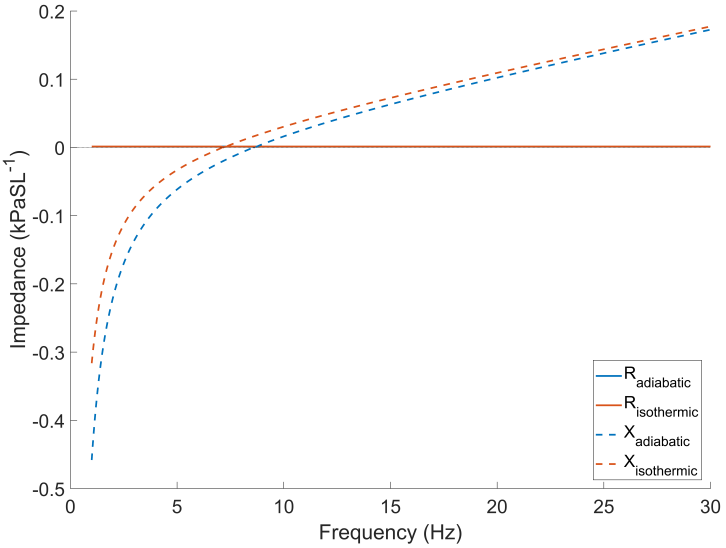


Figure 2.1: Comparison of the theoretical impedance of an adiabatic and an isothermal driven Helmholtz resonator with a 50L cavity volume.

This theoretical model of respiratory FOT is limited by a lack of a significant resistive component to the impedance, as shown in Figure 2.1, as the cavity is assumed to have no resistance. The addition of resistive components rapidly increases the complexity of this model and so it is common practice to use an electrical circuit based analogous model instead.

A more detailed look at Forced Oscillations can be found in [57].

2.2.2 Electric Circuit Models

Electrical impedance to the flow of charge within a circuit is comparable to respiratory impedance to the flow of air, with the potential difference across a wire relating to pressure in the airways, and electric current relating to air flow. The resistance of a circuit is therefore directly comparable to the resistive component of respiratory impedance. If a circuit has an inductance this will

cause the current to lag behind the potential difference as the inductor resists the change. This is directly comparable to the phase shift between air flow and pressure caused by the inertance of air in the airways. Conversely, if an electric circuit is primarily capacitive, the current will lead the potential difference making capacitance comparable to compliance. These three components can be combined in different ways to produce different RIC circuit models of respiratory impedance.

The purpose of a mathematical model such as the electric circuit models of respiratory impedance is to describe the features of the system they are modelling. In the case of respiratory impedance, a good model should accurately describe both the resistive and reactive components of Z.

RIC Model

The simplest model RIC circuit consists of a single resistor (R), inductor (I) and capacitor (C) in series as shown in Figure 2.2

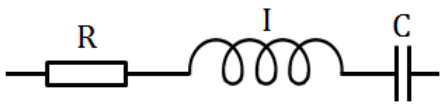


Figure 2.2: Schematic diagram of RIC circuit model of human respiratory impedance.

The impedance of the RIC circuit is given by

$$Z = R + \left(\omega I - \frac{1}{\omega C}\right) i, \tag{2.14}$$

where ω is the angular frequency. This is a poor model of respiratory impedance as, whilst the reactive component approximately follows the curve of the patient data, the resistive component has no frequency dependence. This

is due to the fact that the resistive component is described using a constant with no dependence on ω. This is illustrated in Figure 2.3 which shows the RIC model fitted to typical healthy data.

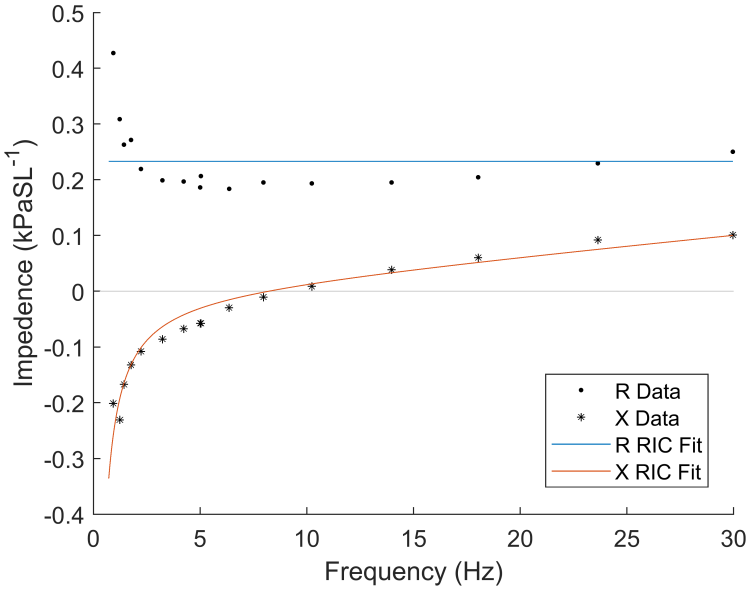


Figure 2.3: RIC model fitted to healthy volunteer data.

Extended RIC Model

An improved version of the model was created with the addition of a second resistive component representing the peripheral resistance (R_p), as opposed to the central resistance (R_c). This model is called the extended resistor-inductor-capacitor (eRIC) model and is shown schematically in Figure 2.4 [36].

The impedance of the eRIC model is given by

$$Z = R_c + \frac{R_p}{1 + (\omega R_p C)^2} + \left(\omega I - \frac{\omega {R_p}^2 C}{1 + (\omega R_p C)^2}\right) i. \tag{2.15}$$

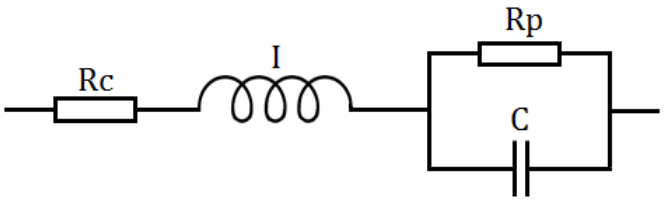


Figure 2.4: Schematic diagram of eRIC circuit model of human respiratory impedance.

The added resistor makes the resistive component of the eRIC model frequency dependent and also gives a closer fit to the reactive component of the data. Figure 2.5 shows the eRIC model fitted to the same healthy volunteer data as shown in Figure 2.3. It can be seen that at lower frequencies the eRIC model gives a good fit however at the higher frequencies the resistive component plateaus instead of increasing with frequency. Once again this is due to the model lacking a component part that describes an upward trend in resistance at higher frequencies.

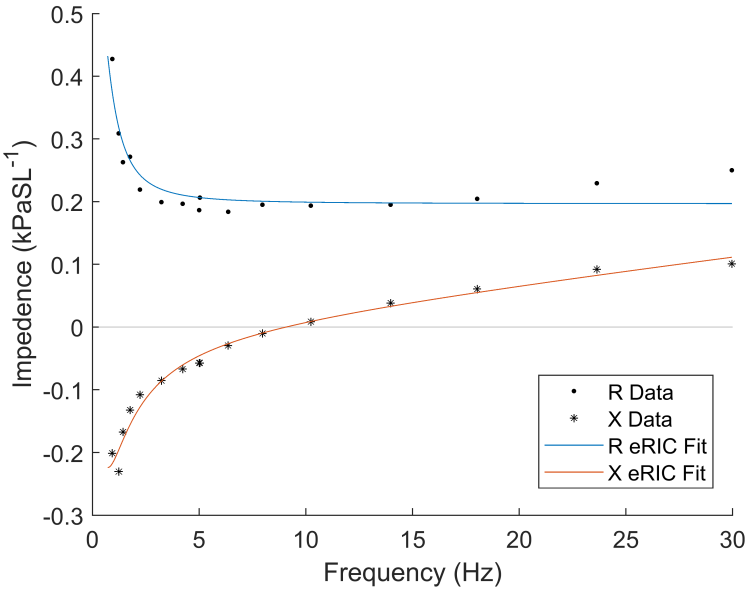


Figure 2.5: eRIC model fitted to healthy volunteer data.

Augmented RIC Model

The eRIC model can then be further developed by the splitting the capacitance of the circuit into two component parts: the extrathoracic capacitance (C_e) which refers to the capacitance of the upper respiratory tract, and the peripheral capacitance (C_p). This five component model is called the augmented RIC model (aRIC) and is shown in Figure 2.6 [37].

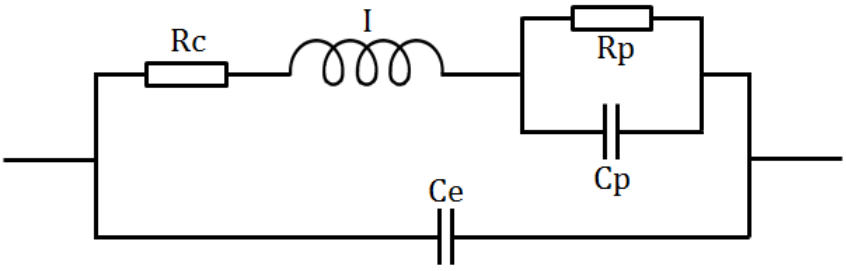


Figure 2.6: aRIC model of human respiratory impedance.

The impedance of the aRIC model can be calculated using Equation 2.16.

$$Z = \frac{A(R_cA + R_p)}{\left[A(1-\omega^2 IC_e) + \omega^2 {R_p}^2 C_p C_e\right]^2 + \left[\omega C_e(R_cA + R_p)\right]^2}$$

$$+ \frac{\omega(IA - {R_p}^2 C_p)\left[A(1-\omega^2 IC_e) + \omega^2 {R_p}^2 C_p C_e\right] - \omega C_e(R_cA + R_p)^2}{\left[A(1-\omega^2 IC_e) + \omega^2 {R_p}^2 C_p C_e\right]^2 + \left[\omega C_e(R_cA + R_p)\right]^2} i, \tag{2.16}$$

where $A = 1 + (\omega R_p C_p)^2$.

The aRIC model is an improvement on the eRIC model as it not only has a frequency dependence in both its resistive and reactive components but also fits accurately to the resistive data at higher frequencies. This is shown in Figure 2.7 which shows the aRIC model fitted to healthy volunteer data.

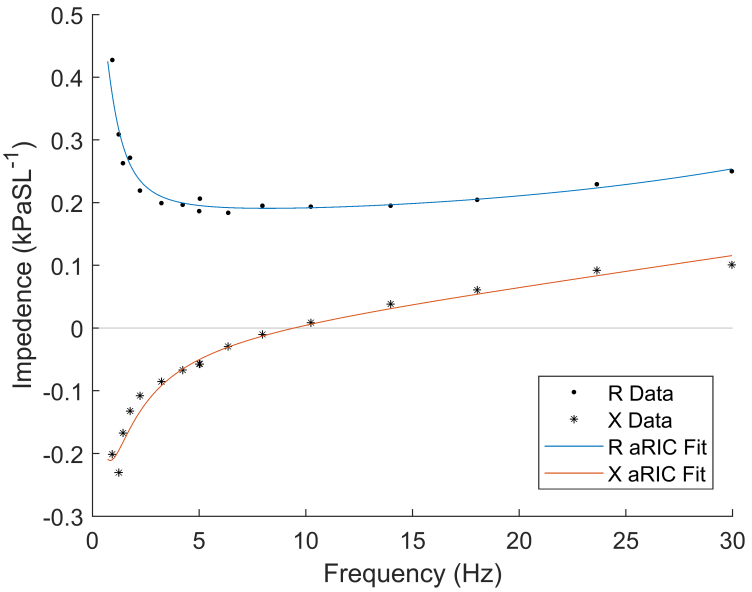


Figure 2.7: aRIC model fitted to healthy volunteer data.

Mead Model

One of the earliest models to be proposed was the seven component Mead model. Of all proposed electrical ciruit models, this model has the largest number of components with four separate capacitors to represent different tissue compliances. These are the lung compliance (C_l), bronchial tube compliance (C_b), chest wall compliance (C_w) and the extrathoracic compliance (C_e). As with the previous two models there are still two resistances labelled the central resistance (R_c) and peripheral resistance (R_p) as well as a single inertance (I) [58]. The aRIC model is sometimes considered to be a simplified version of the Mead model due to their similar layouts. The layout of the Mead model is shown in Figure 2.8.

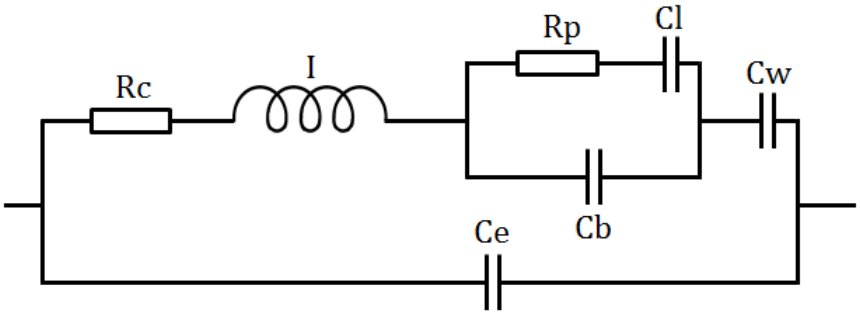


Figure 2.8: Mead model of human respiratory impedance.

The impedance of the Mead model is described by the Equation 2.17.

$$Z = Z_R + iZ_X, \tag{2.17}$$

where

$$Z_R = \frac{R_M}{1 - 2\omega C_e X_M + \omega^2 {C_e}^2 ({R_M}^2 + {X_M}^2)},$$

$$Z_X = \frac{X_M - \omega C_e ({R_M}^2 + {X_M}^2)}{1 - 2\omega C_e X_M + \omega^2 {C_e}^2 ({R_M}^2 + {X_M}^2)},$$

with

$$R_M = \frac{R_p {C_l}^2}{\omega^2 {R_p}^2 {C_b}^2 {C_l}^2 + (C_b + C_l)^2} + R_c,$$

$$X_M = \omega I - \frac{\omega^2 {R_p}^2 C_b {C_l}^2 + C_b + C_l}{\omega^3 {R_p}^2 {C_b}^2 {C_l}^2 + \omega (C_b + C_l)^2} - \frac{1}{\omega C_w}.$$

Figure 2.9 shows the Mead model fitted to the same healthy volunteer data as seen with the other models. In this instance the Mead model, with its two additional capacitive components, does not appear to have any advantage over the aRIC model as both models have a close fit to the data. The previous model, the aRIC model, contains the necessary number of component parts to fully describe respiratory impedance. However, the Mead model contains an excess of components which reduces the usefulness of the value of the model parameters. This has been previously observed by Diong et al. [37] who found the aRIC model to be superior to the Mead model for this reason. However, the Mead model is more robust, capable of fitting to data with more noise and anomalous points and is useful for matching the shape of an impedance curve for interpolating the values of f_{res} and $R_5 - R_{20}$.

The parameters calculated by fitting data to the aRIC model as well as f_{res} and $R_5 - R_{20}$ were examined to find out which parameters where useful indicators of lung condition.

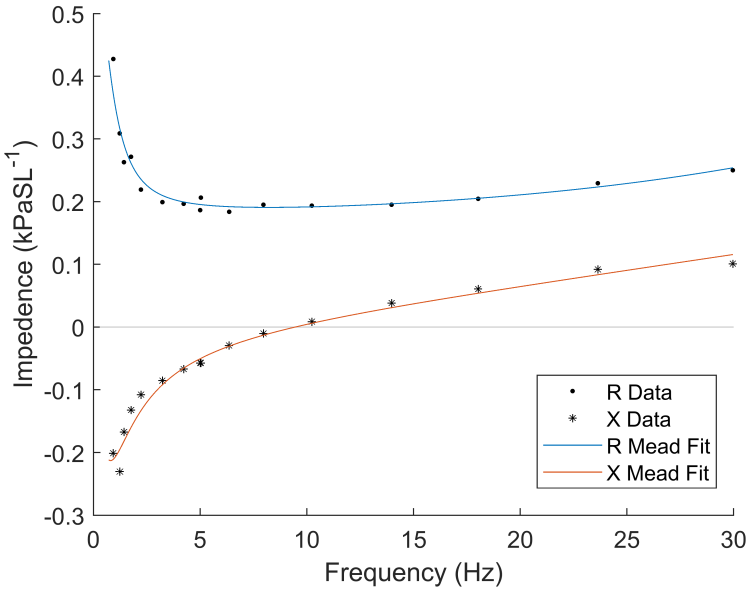


Figure 2.9: Mead model fitted to healthy volunteer data.

2.3 Method - Phantom Study

2.3.1 Equipment

FOT Device

The FOT device used for the phantom study was an in-house device utilizing an 8WAE Subwoofer manufactured by JL audio as the source of the impulses with measurements made using a Hans Rudolph Pneumotach Amplifier 1 (PA-1). A schematic of this device is shown in Figure 1.5.

Before each measurement the device was normalised by operating with the mouthpiece first fully obstructed to, theoretically, give a measure of pressure with no flow, then with the mouthpiece fully open to, theoretically, give a measure of only flow and no pressure and then finally obstructed with a known impedance to give a measure of both flow and pressure. In reality, in the first

measurement the flow rate is not zero due to the compressibility of air in the system. Similarly, during the second measurement, the pressure has a positive value due to the resistance given by the filter in mouthpiece and step changes in the diameter of the tube between the device and the mouthpiece. As these factors were present in all patient measurements, a corrective normalisation factor was required for each run, which was calculated from these first two normalisation measurements. The third normalisation run using a known impedance had the purpose of identifying the difference in phase between p and Q due to the device (as opposed to the phase difference caused by the lungs). In order for this to be achieved the known impedance had to have a known reactance as well as a known resistance. This was done by having a purely resistive standard resistor with no reactive component to its impedance which was achieved using a wire mesh gauze. The corrective normalisation factor from the first two measurements was applied to this third measurement.

Additionally the device was further calibrated to ensure that the device was measuring accurate values for pressure and flow in a more general sense. The volume was calibrated using a 3L syringe that was repeatedly pumped whilst the oscillations produced by the loudspeaker of the device had an amplitude of zero. The measured flow rate was therefore entirely due to the air exiting and entering the syringe. The measured flow rate was then integrated for each half of the pumping cycle to evaluate the volume. This allowed the flow rate measured by the device to be validated, as the volume of the syringe was known. A similar process was performed using a manometer to compare the theoretical, applied pressure given by the displacement of water, to the pressure measured by the device.

With these corrective measures in place the results from the device were given in terms of the resistance of the standard resistor. A different standard resistor

with a known resistance of R=0.18 kPaSL^{-1} was used to evaluate the resistance of the standard resistor used in the normalisation process. It was found that the standard resistor had a resistance of R=0.233 ± 0.016 kPaSL^{-1} which allowed the arbitrarily normalised measurements to be converted into SI base units.

The FOT device could be operated in two modes: "single sine" and "multisine". In "single sine" mode the loudspeaker produced waves of a single frequency whilst in "multisine" mode the loudspeaker produced a composite waveform containing multiple frequencies. For the study described in this thesis, two frequency ranges, each containing eight frequencies, were assessed: a low frequency set ranging from 1 Hz to 5 Hz and a high frequency set ranging from 5 Hz to 30 Hz. The frequencies contained in the "High" and "Low" frequency ranges are shown in Table 2.1. Any waveform containing multiple sine waves will have peaks of varying amplitudes. As these peaks correspond to the amplitude of the pressure wave imposed on the patient it is important to reduce the maximum size of these peaks as much as possible to improve patient comfort. This was done by minutely adjusting the frequency of the component sine waves to find a local minimum for each of the frequencies contained in the range. For this reason the high and low frequency ranges shown in Table 2.1 are approximations of the true frequencies. FOT measurements of both the High and Low frequency ranges were acquired for each patient as well as a single sine measurement at 8 Hz. Each data set had three repeat measurements taken with an average calculated from these.

Low	High
0.9333	5.0000
1.2333	6.3667
1.4333	7.9667
1.7667	10.2333
2.2333	13.9667
3.2333	18.0333
4.2333	23.6333
5.0333	29.9667

Table 2.1: The frequencies (in Hz) contained in the high and low frequency FOT measurements

Phantoms

One of the key aims of the phantom study was to establish the validity of the in-house device. A phantom has two key advantages of a human subject. Firstly the phantom will remain constant between measurements allowing comparisons to be made. This is not the case for a human subject who can change in many ways (e.g. breathing pattern, lung condition, general health etc.) between measurements. This makes a human subject less reliable for calibrating and comparing devices. The other advantage of a phantom is that it can be manipulated in a precise way. In this study the airways of the phantom could be readily obstructed in a way that is not possible with a human subject. A barrel phantom consisting of a 50L metal barrel with a connecting tube was used for to validate the reactive measure of the in-house device (the resistive measure was calibrated using a standard resistance as previously described in Section 1.2.1).

The phantom study was also performed to investigate how physical changes to a phantom lung affect FOT measurements. This was done using a phantom consisting of a 3-D print of the first seven generations of the upper airways, the design of which was derived from an x-ray CT of a mildly asthmatic set of lungs. This design, shown in Figure 2.10 was used to form a core around which an elastomer layer, with a similar Young's modulus to that of the cartilage in the trachea, was cast; the core was subsequently removed. Overall the airway model contained 72 termini (not including the opening at the top of the trachea) that could be systematically occluded using a reusable adhesive putty. The airway was then housed in a sealed plastic cylinder, representing the chest wall, with a rubber membrane at the base, representing the diaphragm. A moveable circular plunger was placed against the membrane such that the membrane was distended. This plunger could then be adjusted to alter the distension of the membrane.

Experiments were performed on the phantom at both the University of Nottingham and also at Glenfield Hospital, Leicester, in order to provide a comparison between FOT devices. In Nottingham, the device used for taking FOT measurements was the same as the device used for the patient study described previously in section 2.5.1. A further two commercial devices were used at Glenfield Hospital: an Erich Jaeger MasterScreen IOS and a tremoFlo C-100 airwave oscillometry system. The MasterScreen IOS system utilized a loudspeaker to produce the oscillations in a similar manner to the device used in Nottingham. However the MasterScreen produced a waveform of an impulsive nature rather than a continuous sinusoidal waveform as seen in the Nottingham and tremoFlo systems. The tremoFlo C-100 system was different to the Jaeger and Nottingham systems in that it used a fan instead of a loudspeaker to produce the continuous waveforms. This allows the tremoFlo system to be a more lightweight, handheld system.

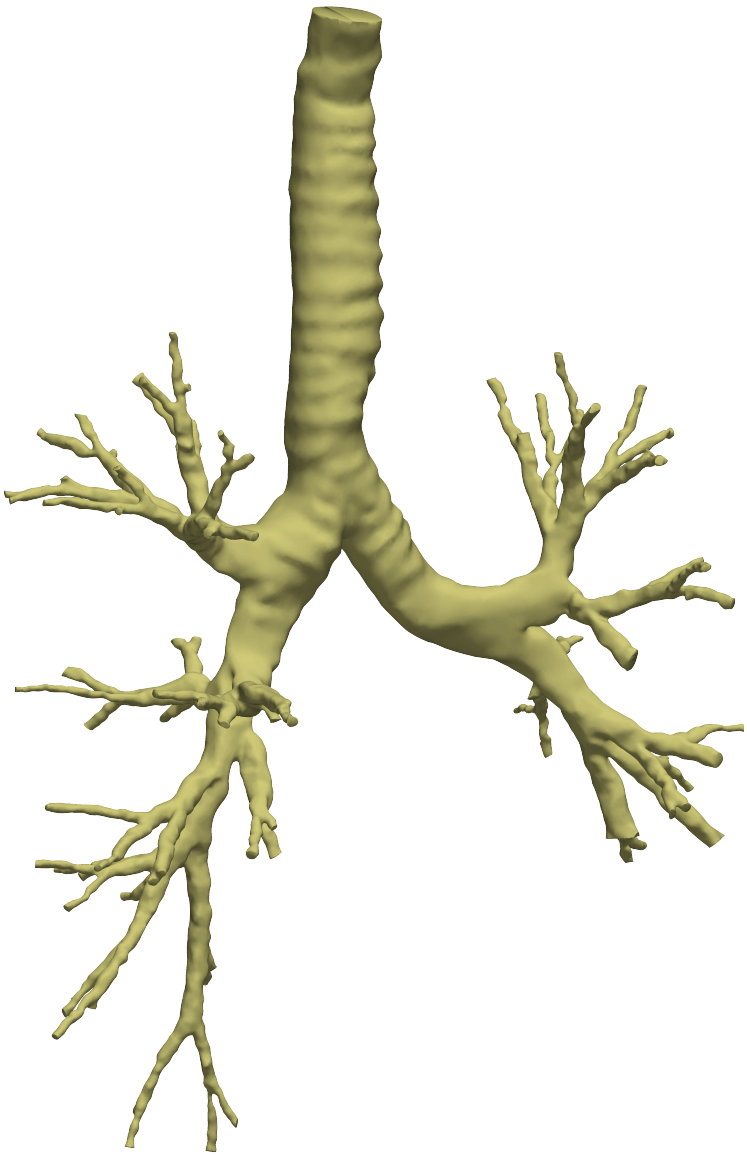


Figure 2.10: Design of the seven-generation airway model used as an FOT phantom, derived from an x-ray CT of a healthy set of lungs.

2.3.2 Parameter Evaluation

The aRIC electric circuit model, described in section 2.2.2, was fitted to the FOT measurements for both the phantom and patient studies. Fitting was done using a least squares fitting algorithm using the MATLAB function *lsqcurvefit*. The models were fitted to both the Low and High frequency ranges as well as a combined data set with the 16 frequencies from both data sets. This was done to calculate values of R_c, I and C_p. Fitting was performed on data sets taken both pre- and post-BD.

f_{res} was calculated for each data set by fitting the Mead model to the entire frequency range. This was then used to form a high resolution impedance curve to interpolate the frequency at which X had a value of zero. This impedance curve was extrapolated up to 40 Hz to allow for the estimated measurement of f_{res} in cases where f_{res} was greater than the highest frequency measured (30 Hz). The value of $R_5 - R_{20}$ was also evaluated using this fitted model as 20 Hz was not a frequency present in either of the multisine waveforms.

2.3.3 Measurement Procedure

All three systems were calibrated using a standard resistor with a known resistance (R=0.233 $\pm$ 0.016 kPaSL^{-1} in Nottingham and R=0.18 kPaSL^{-1} in Leicester) however there is no commonly used standard to calibrate the measurement of reactance as the standard resistors are made of mesh gauze with no reactance. A 3L gas syringe was used to compare the reactive measurements of the three systems as the volume of air provides an inertance due to its mass and a compliance due to its compressibility.

Two main experiments were carried out using the phantom lung in Nottingham to investigate two physiological features of the lungs: compliance and obstruction. The effect of lung compliance on FOT measurements was investigated

by distending the rubber diaphragm at the base of the phantom as described earlier. The further the diaphragm was distended the lower the compliance of the system. FOT was performed at the "High" (5 - 30 Hz) and "Low" (1 - 5 Hz) frequency ranges as described previously with the aRIC model used to evaluate further FOT parameters. This experiment was only performed at Nottingham, not at Glenfield and so no comparison could be drawn between different devices.

The other set of experiments performed on the phantom lung investigated the effect of airway obstructions on measured FOT parameters. The phantom lung had 72 termini that could be occluded to simulate different severities of obstructive lung disease. These termini were labelled and occluded in the same order at both sites to allow a comparison to be drawn. FOT was performed at the "High" (5 - 30 Hz) and "Low" (1 - 5 Hz) frequency ranges in Nottingham; 5 - 35 Hz with the Jaeger system, and 5 - 40 Hz with the tremoFlo system. Measurements of the effect of obstruction on impedance were carried out on the printed airways with and without the housing cylinder representing the remainder of the lung.

2.4 Results - Phantom Study

2.4.1 Barrel Phantom

One of the aims of the phantom study was to establish the validity of the Nottingham FOT system. The device was calibrated using a standard resistor however there are no standard reactances that can be used. It was hoped that the printed phantom could be used as a standard with both a known resistive and a known reactive component (as opposed to the purely resistive standards that are currently used) however the effect of changing the compliance of the system was only measured using the Nottingham system and so no comparison could be drawn. There is a further issue however, in that the phantom used

a rubber sheet. This is a problem as the reactance of the system is reliant on the type, thickness and, possibly most notably, age (as rubber perishes) of the rubber used, making it extremely difficult to produce an identical phantom for a standard at another site.

An alternative standard reactance is a known volume of air as this can be easily recreated at any site and has both inertance and compliance. The issue with using a volume of air is that the volume must be relatively large (tens of litres) to have a comparable reactance to the human lung and so the 3L syringe used for calibration and comparison between the Nottingham and Leicester devices is not a perfect standard. An example of the impedance curve for a large volume of air (50L) in a barrel with a rigid connecting tube containing an obstruction (to provide a resistive component to Z) is shown in Figure 2.11 along with an impedance curve from a healthy human lung for reference.

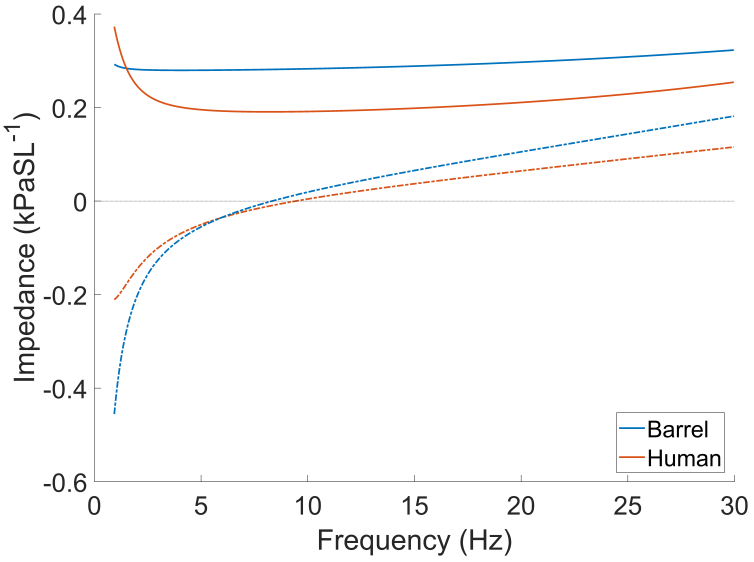


Figure 2.11: Impedance curve for Barrel Phantom and healthy human lungs.

It can be seen that the Barrel Phantom had a similar value to the human for f_{res} (f_{res} = 8.32 Hz and 9.45 Hz for the Barrel and human respectively) as well as a similar shape to the reactive component of the impedance curve; however, there was extremely limited frequency dependence seen in the resistive component. There is another issue with using a large volume of air as a phantom in that the system will behave adiabatically rather than isothermally, which is the case in both the lungs and phantoms that utilise a smaller volume (which diverges from being an adiabatic system at ~4L [60]). The effect of this difference is explored in Section 2.2.1. Figure 2.12 shows the experimental data for the Barrel Phantom compared to theoretical models of forced oscillators in adiabatic and isothermal regimes. An additional resistive component was added to the theoretical models to simulate the obstruction added to the Barrel Phantom. It can be seen that, as predicted, the Barrel Phantom reacts adiabatically as opposed to isothermally. This can be resolved through the addition of a substance that will not change temperature, such as fibreglass, to the volume. As the experimental data matches the theoretical data extremely well, the reactive measure of the Nottingham FOT system can be considered to be reliable.

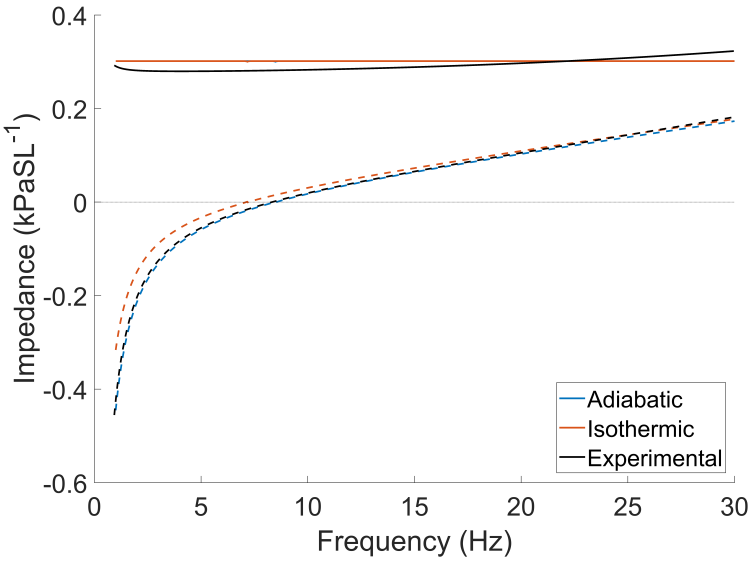


Figure 2.12: Experimental data for Barrel Phantom compared to theoretical Isothermal and Adiabatic forced oscillator models.

2.4.2 Printed Airway Phantom

A 3-D printed model (described in Section 2.3) of the upper airways of the body was used to investigate the effects of changes in compliance and severity of obstruction on respiratory impedance. The compliance of the system was changed by distending the rubber diaphragm of the phantom. Figure 2.13 shows the effect on C_p (evaluated by fitting the aRIC model to the data) and f_{res} of the increase in distension in the rubber. As expected, increasing the distension of the diaphragm resulted in a decrease in compliance, which supports the idea that the stiffness of the lungs can be measured using FOT. A clear trend can also be seen between the value of f_{res} and distension, with an increased f_{res} measured with more distension. Once again this is to be expected as, when the diaphragm is more taut, it will not resonate at lower frequencies. No significant change was seen in the resistive component of Z or any related resistive variables

(such as $R_5 - R_{20}$) as a result of the distension. These results clearly demonstrate the link between the compliance of the system and f_{res} as measured using FOT, which gives confidence to the usefulness of FOT as a diagnostic technique.

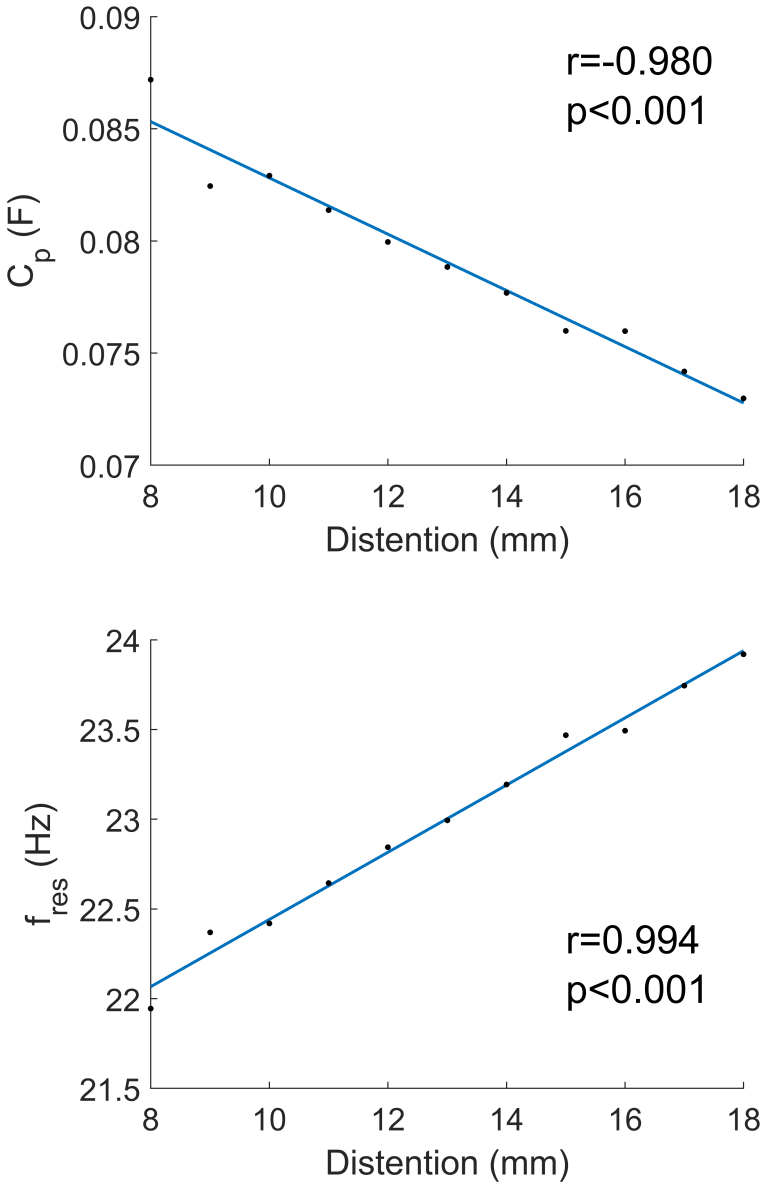


Figure 2.13: Values of C_p and f_{res} for the printed lung phantom measured at increasing distensions of the rubber diaphragm with a line of best fit.

The printed phantom was also used to investigate the effects of airway obstructions on measured FOT parameters including parameters measured using the aRIC model. This was done using the complete model (with the printed airway housed inside a cylinder representing the chest wall and a rubber diaphragm) as well as on the printed airways only (without any housing). As was expected, the most significant response to increased airway obstruction was seen in the resistive parameters, rather than the reactive component. The values of R_c (calculated using the aRIC model), R_5 (the real component of Z at 5 Hz), R_{20} (the real component of Z at 20 Hz) and $R_5 - R_{20}$ for measurements with and without the housing are shown in Figures 2.14 and 2.15, where Figure 2.14 shows the data taken with the housing cylinder and Figure 2.15 shows the data taken of just the printed airway without the housing cylinder.

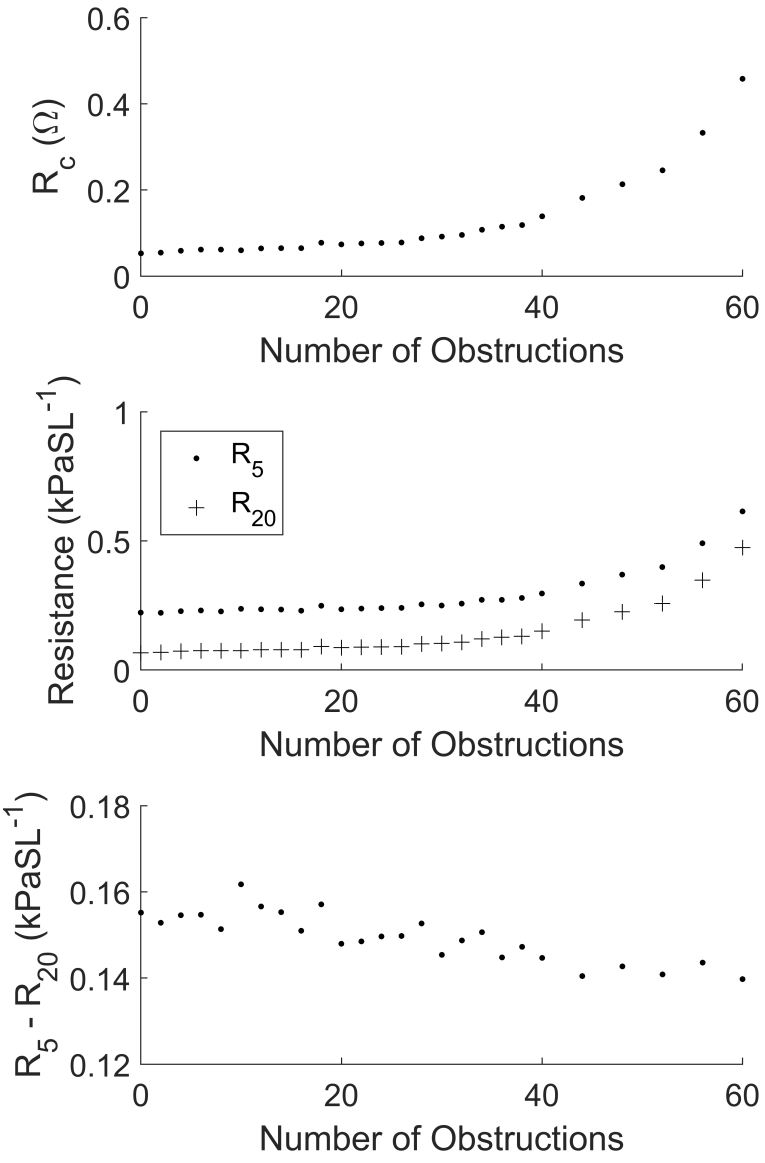


Figure 2.14: Values of R_c (calculated using the aRIC model), R_5, R_{20} and $R_5 - R_{20}$ versus the number of obstructed airways in the printed airway with the housing cylinder.

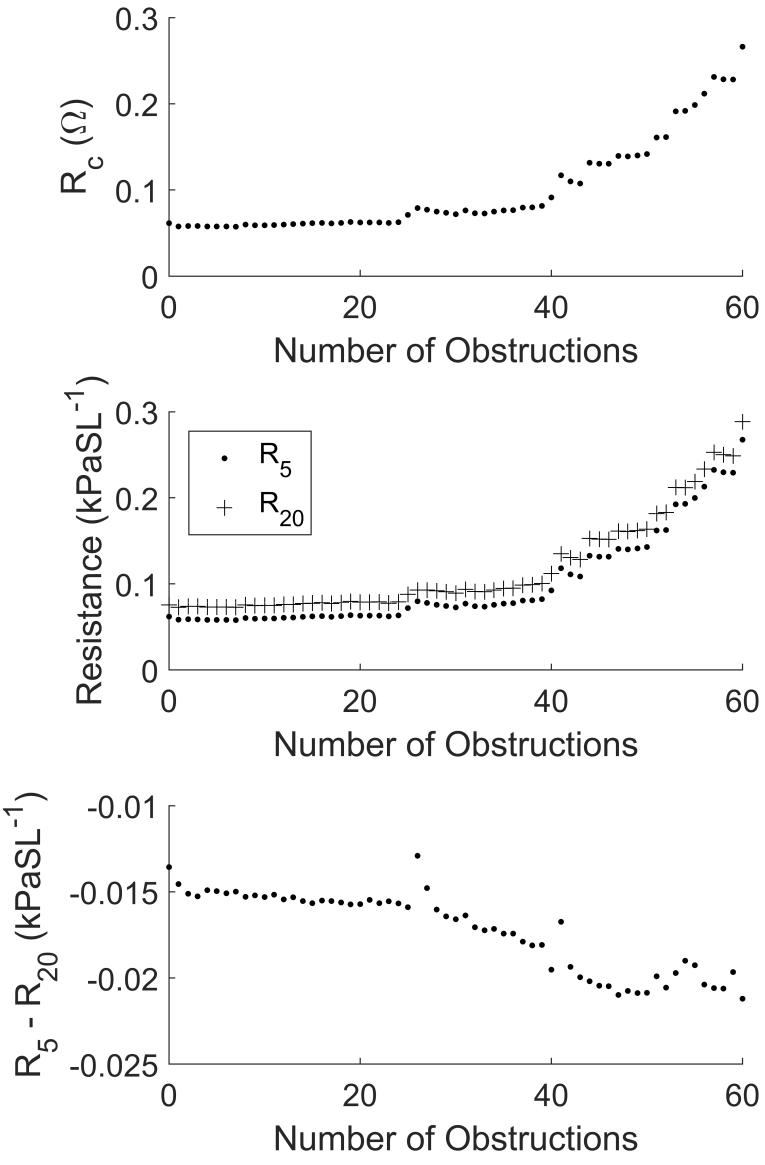


Figure 2.15: Values of R_c (calculated using the aRIC model), R_5, R_{20} and $R_5 - R_{20}$ versus the number of obstructed airways in the printed airway without the housing cylinder.

There is a clear non-linear relationship between the resistance of the system and the number of obstructions with values of R_c, R_5 and R_{20} rapidly increasing at higher levels of obstruction. There was also an observed decrease in $R_5 - R_{20}$ at higher numbers of obstruction. This was unexpected as an increase in $R_5 - R_{20}$ was seen in patients with obstructive lung disease compared to healthy volunteers. However the phantom is flawed in that the majority of the obstructions were located in the same generation of airway due to the design of the phantom, thus making it impossible to only alter the smaller airways instead of the upper airways. This could explain this unexpected trend as $R_5 - R_{20}$ is thought to relate to the condition of the smaller airways. The variation in $R_5 - R_{20}$ caused by obstructions in the phantom was very small and so this trend would most likely be dominated by a different effect in obstructive lung disease. The trends in R_c, R_5, R_{20} and $R_5 - R_{20}$ were seen both with and without the housing cylinder. Figures 2.14 and 2.15 only show values up to 60 obstructions as after 60 obstructions the system no longer resembled that of a human lung. As no functional human lung could become this obstructed, this is not a problem.

One of the issues with the resistance of the printed phantom is that all the termini were connected to the same container (or the atmosphere). Therefore a single obstruction did not remove a significant portion of the model lung from being ventilated. This explains why there is limited response to obstruction until after 20 obstructions.

The values of Z taken using the whole phantom, instead of just the printed airway, provided values of Z that were more comparable to that of a human lung including an f_{res} of approximately 23 Hz, whilst the printed airway on its own had an unrealistically small resistive component and no measurable value for f_{res}. The two commercial measurement systems in Leicester took measurements

of the printed airway without the housing cylinder only. Obstructive measurements in Nottingham were therefore taken without the housing cylinder to allow a comparison to be drawn.

2.4.3 Comparison of FOT devices

Three different FOT devices, a custom device from Nottingham (described in Section 2.5.1), an Erich Jaeger MasterScreen IOS and a tremoFlo C-100 airwave oscillometry system, were compared to investigate the differences between FOT and IOS systems, as well as possible differences between loudspeaker (Nottingham and Jaeger) and fan (tremoFlo) based systems. All three devices performed FOT on a 3L syringe of air (a purely reactive standard) and on a 3-D printed phantom.

Figures 2.16 and 2.17 show a comparison of the measured reactances of the 3L syringe between the different systems. The raw data points of reactance for the different measurement frequencies used for each of the three systems are shown in Figure 2.16. A strong similarity can be seen that the tremoFlo and Nottingham devices whilst the Jaeger has a noticeably less negative reactance, particularly at lower frequencies. This is highlighted in Figure 2.17 which shows a direct comparison between the measured reactances, with the line $y = x$ for reference. The aRIC model was fitted to the data in order to allow direct comparisons between reactances measured with different sample sizes at different frequencies. This fit is shown in Figure 2.17 and highlights the strong similarity between the Nottingham and tremoFlo devices as well as showing a notable difference in the Jaeger results at a more negative reactance.

The three devices were also used to take measurements of the printed airway (described in Section 2.3) without the housing cylinder at varying levels of obstruction. It has been previously noted that adjusting the number of obstruc-

tions in the phantom had an insignificant effect on the reactive component of Z and so this was a test of the comparability of the resistive measures of the three systems. The values of R_5, R_{20} and $R_5 - R_{20}$ for different numbers of obstructions are shown in Figure 2.18.

It can be seen that all three systems showed the same trend in the effect of obstruction on R_5 and R_{20} with a general increase with obstruction that significantly increased after 45 occlusions. However, as with the reactive measurements from the 3L syringe, there appears to be a closer similarity between the two FOT systems (Nottingham and tremoFlo) compared to the IOS system. This is extremely apparent in the measure of $R_5 - R_{20}$ where a large decrease is seen at high levels of obstruction in the Jaeger system only, with only a gradual and relatively linear decrease present in the FOT systems.

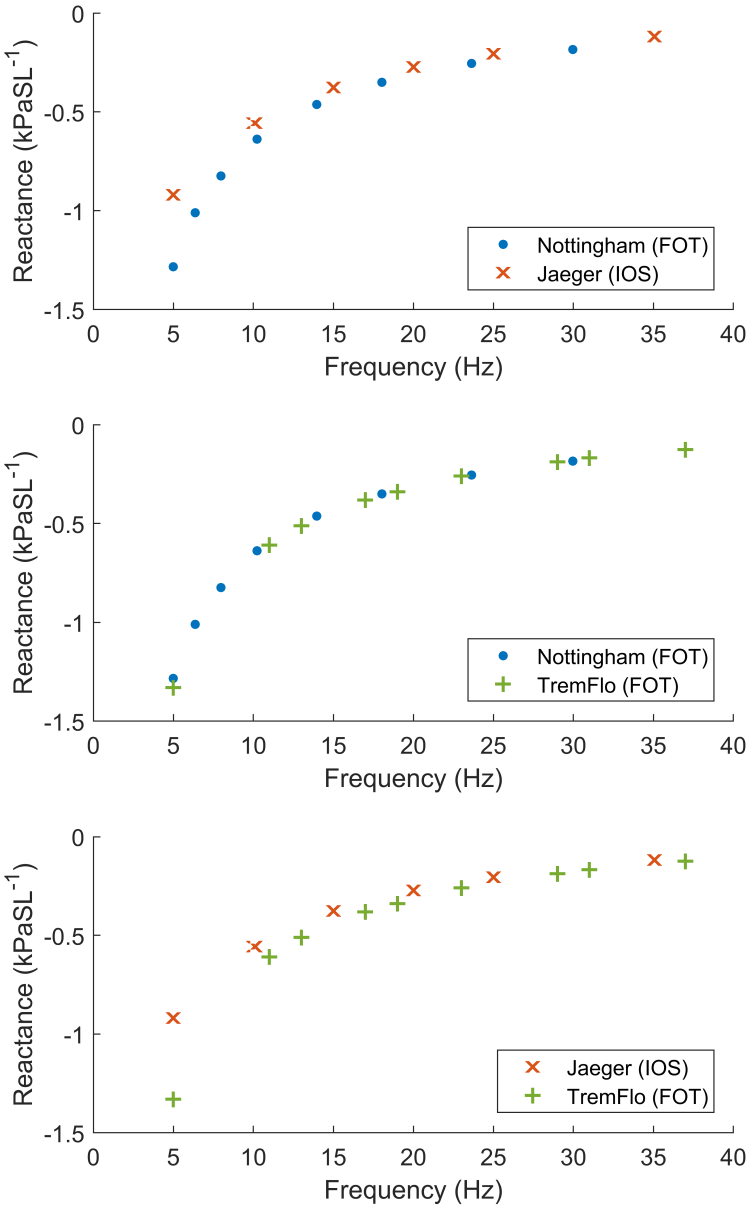


Figure 2.16: Reactance of 3L syringe measured at different frequencies by the Nottingham (FOT), Jaeger (IOS) and tremoFlo (FOT) systems.

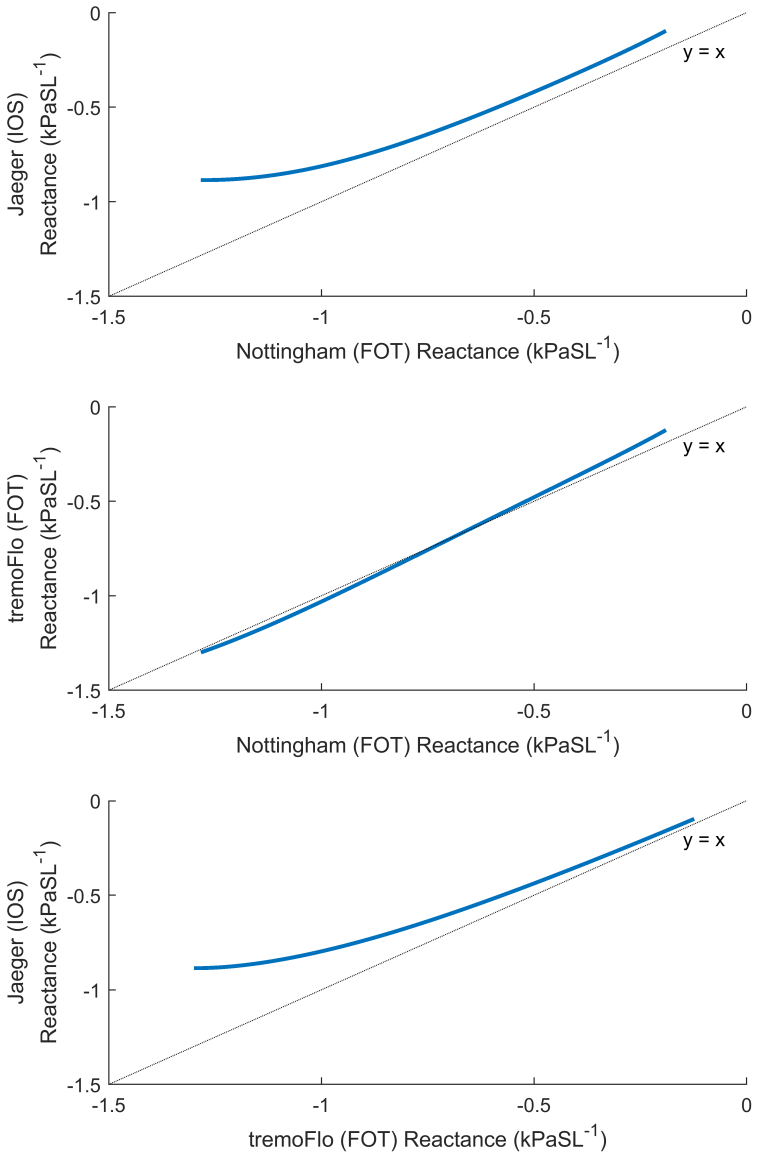


Figure 2.17: Comparison of reactance curves (calculated using aRIC model) of 3L syringe measured using three different systems with y=x for comparison.

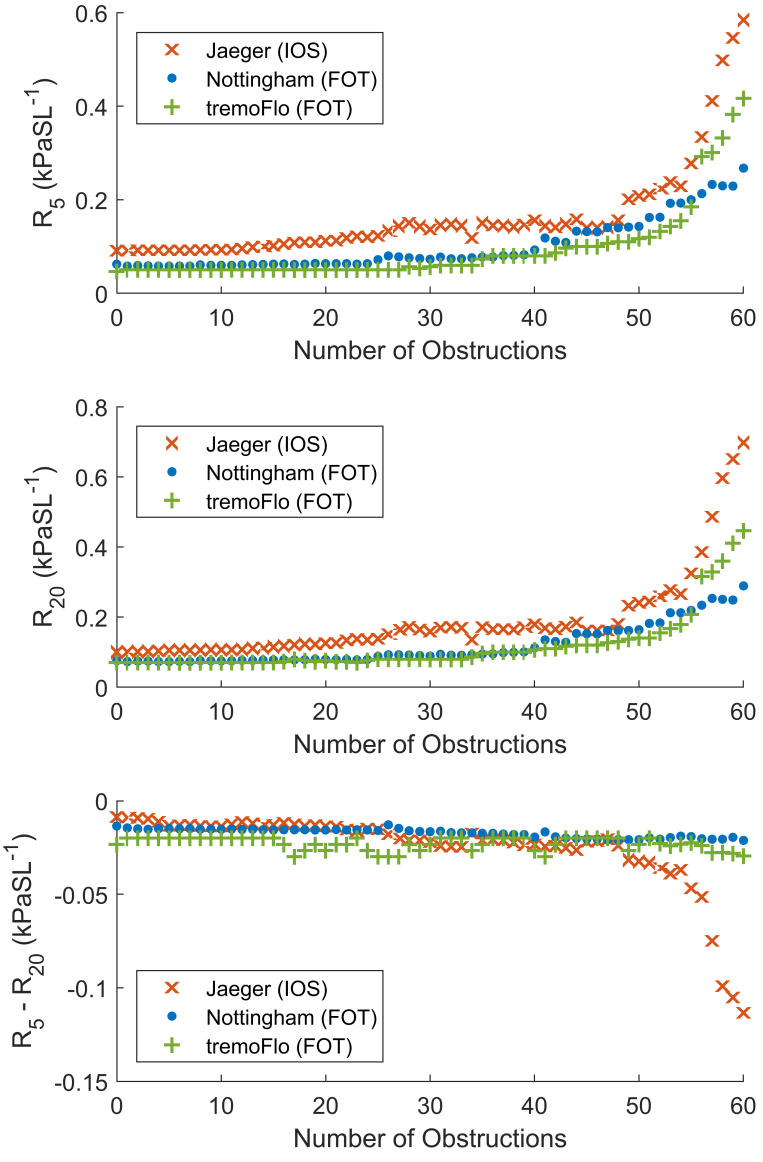


Figure 2.18: Comparison of R_5, R_{20} and $R_5 - R_{20}$ versus the number of obstructed airways in the printed airway, without the housing cylinder, measured using three different systems.

2.5 Method - Patient Study

2.5.1 Data Acquisition

In order to study the effect of a bronchodilator on lung function as measured using FOT and spirometry, participants underwent both FOT measurements and spirometry. Spirometry was performed as per the American Thoracic Society/European Respiratory Society guidelines, using a Vitalograph Gold Standard wedge bellows spirometer (Vitalograph, Buckingham, UK). This was used to evaluate values of FEV_1 and FVC which in turn were used to calculate FEV_1/FVC. The FOT device used for the patient study is described in section 2.3.

For each visit, patients first underwent FOT measurements followed by spirometry. This was then repeated twenty minutes after the administration of the SABA, 400 µg of salbutamol via a spacer. Potential participants were identified from patients attending respiratory out-patient appointments at Nottingham University hospitals NHS trust, and from the NRRU database. Exclusion criteria were: inability to perform spirometry; inability to provide written consent; inability to refrain from taking their airway medication before their next clinic appointment (24 hours for long-acting anti-muscarinics, 12 hours for long-acting bronchodilators and 4 hours for short-acting bronchodilators) and suspected active respiratory infection. The inclusion criteria for patients were: age between 18-85 years old; confirmed diagnosis of COPD or asthma (based on past medical history from consultant diagnosis, spirometry and risk factors). Healthy controls were identified from the Nottingham Respiratory Research Database. The inclusion criteria were: 18-85 years; never smoked; no diagnosis of respiratory disease. The study was approved by National Research Ethics Service Committee North West - Lancaster, reference 11/NW/0674.

2.6 Results - Patient Study

2.6.1 Patient Baseline

Baseline data for the patient study is shown in Table 2.2, with mean values and standard deviation given (mean/SD). The measurement of FEV_1 was taken pre-BD and is given as a percentage predicted value. A one-way analysis of variance (ANOVA) test with a post hoc pairwise comparison was performed on all baseline data. There were significant differences found between the age of all three groups as well as the sex ratio of the asthma group.

Parameter	Healthy (n=10)	Asthma (n=26)	COPD (n=21)	p-value (H - A)	p-value (H - C)	p-value (A - C)
Mean Age	42 / 13	57 / 15	68 / 5	0.001	<0.001	0.001
Gender (M/F)	8/2	5/21	14/7	<0.001	0.430	0.001
FEV_1 (% pred.)	102.20 / 10.21	87.08 / 24.74	48.24 / 12.64	0.037	<0.001	<0.001

Table 2.2: Mean and SD of measured pre-BD parameters (using spirometry and FOT) for all patient groups.

2.6.2 Identifying Disease Type using FOT

The first aim of the patient study was to confirm that FOT can be used to distinguish between disease states in a similar manner to spiromtery. This was done by comparing the values of the different parameters measured before the SABA was administered. The values of the three spirometric parameters, FEV_1, FVC and FVC/FEV_1, measured pre-BD, are shown in Figure 2.19 with outliers shown with a red +. The difference between the healthy group and

the COPD group is clearly noticeable for all parameters with the asthma group spanning the gap in-between, with the healthy group having higher values for all three spirometric parameters. This is to be expected as healthy lungs have a larger volume and greater ability to expel a large volume in one second than unhealthy lungs. The patients with asthma who took part in the patient study had a varying severity of asthma which gives rise to the large range in value for all three spirometric parameters in the asthma group.

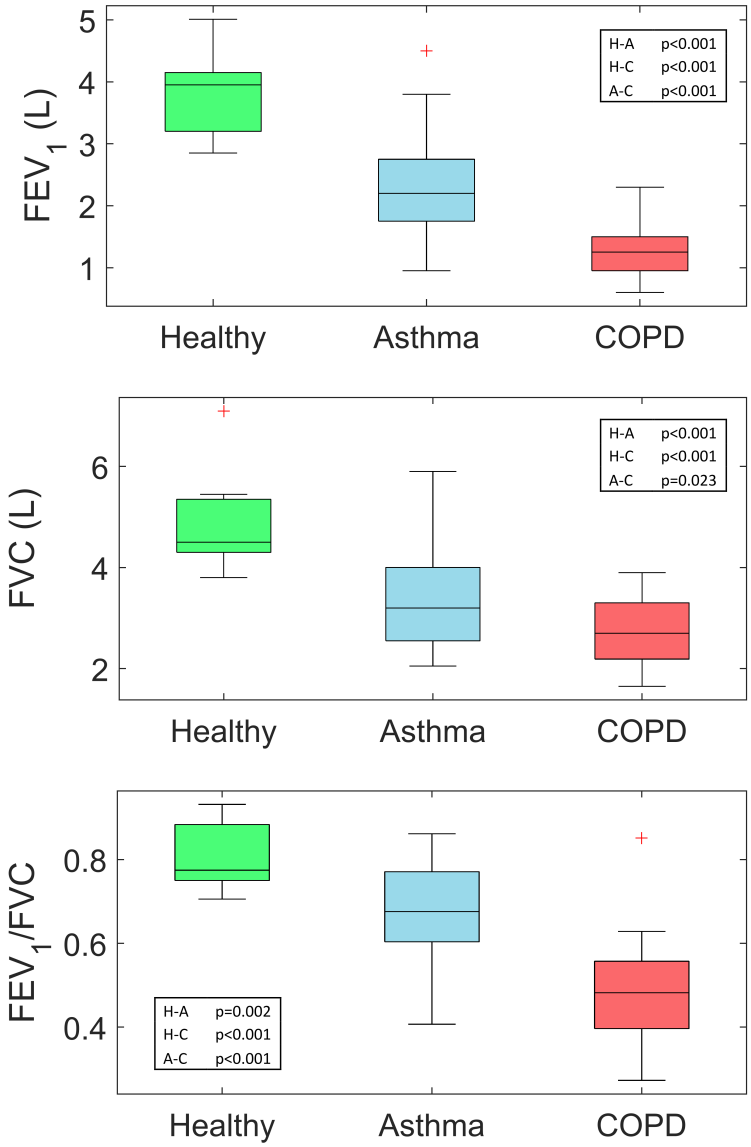


Figure 2.19: Box plots for the three spirometric parameters measured pre-BD for each of the patient groups (outliers are marked with a red +).

An ANOVA with a post hoc pairwise comparison was conducted to verify the statistical significance of the difference in values of the spirometric parameters between the patient groups. It was found that the patient group had a significant effect ($p<0.01$) on all three spirometric parameters confirming that spirometry is an effective measure of assessing disease state. The most significant difference was seen between the Healthy control group and the COPD group. This is to be expected as these are the groups with the largest difference in lung condition.

It was found that the aRIC model was the most useful model for quantifying the frequency dependence of respiratory acoustic impedance. Of the five parameters measurable using the aRIC model (R_c, R_p, I, C_p and C_e) it was found that only R_c, I and C_p were good measures of lung condition with R_p and C_e providing little useful information. The largest difference in R_c was seen at the lower frequency range so values for R were taken from the "Low" multisine waveform. The opposite was true for I which, as has been previously mentioned in Section 1.2.2, dominates at higher frequencies. The values for I were therefore evaluated by fitting the aRIC model to the "High" frequency range. It was found that a difference in C_p could be observed in both frequencies and over the entire frequency range from 1 - 30 Hz and so C_p was evaluated over the whole range for the purposes of the patient study.

The values of the three used aRIC model parameters (R_c, I and C_p) for each of the patient groups, measured pre-BD, are shown in Figure 2.20 with outliers shown with a red +. Once again a notable difference can be seen between the healthy volunteer group and the COPD group with the healthy group having a higher values for I and C_p and lower values for R_c. This is too be expected as a healthy pair of lungs will have a larger volume and therefore a larger mass of air to move giving a larger inertance or inductance in the model. Similarly a healthy lung is more elastic and therefore more compliant giving rise to a higher

capacitance in the fitted model. The lower values for R_c in the healthy volunteer group is also to be expected as healthy airways should have no obstructions of either airway constrictions or excess mucus. Again the asthma group spanned the gap between the healthy and COPD groups with an increased range that is particularly noticeable in the value of I.

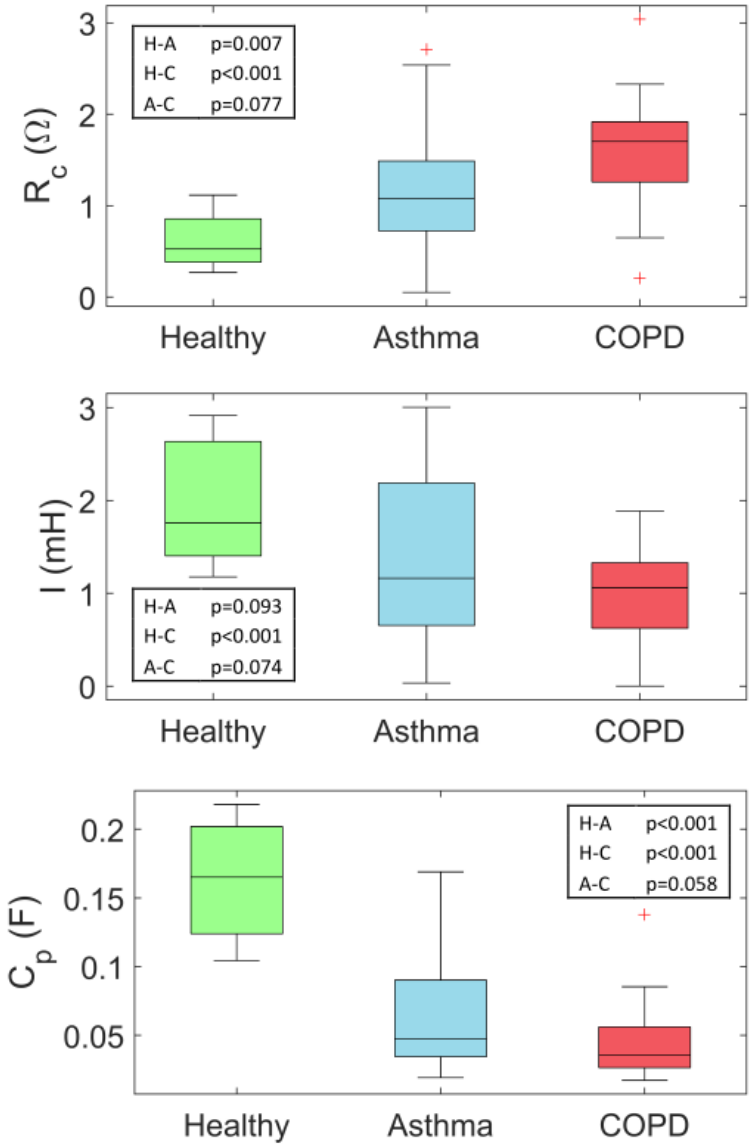


Figure 2.20: Box plots for the three aRIC Model parameters measured pre-BD for each of the patient groups (outliers are marked with a red +).

There is also a heterogeneity in the difference between the asthma group and the COPD group between the different aRIC parameters (Figure 2.20). For the values of R_c the asthma groups sits almost halfway between the healthy and COPD groups in a similar fashion to the three spirometric parameters. However for the value of C_p the asthma group bears a closer resemblance to the values of the COPD group with the healthy group standing out as markedly different. This demonstrates that the three aRIC parameters assess different measures of lung condition, both to the spirometric parameters, and to each other. The observed heterogeneity between the parameters also implies that the different parameters measured using the aRIC model are evaluating different aspects of asthma that cannot be observed using spirometry alone. The similarity of the values of C_p between the asthma and COPD supports the idea of asthma-COPD overlap syndrome (ACOS).

An ANOVA with a post hoc pairwise comparison was conducted to verify the statistical significance of the difference in values of the aRIC parameters between the patient groups. It was found that the patient group had a significant effect ($p<0.01$) on all three measured aRIC parameters confirming that fitting the aRIC model to FOT data is an effective measure of assessing disease state in a manner comparable to spirometry. The most significant difference was seen between the Healthy control group and the COPD group. This is to be expected as these are the groups with the largest difference in lung condition.

The values for f_{res} and $R_5 - R_{20}$ were evaluated by fitting the Mead model to the raw FOT data as previously described. The values for these two FOT parameters measured pre-BD are shown in Figure 2.21. Again, a large difference between the healthy and COPD patient groups can be seen with the asthma group in-between. For these parameters the inverse of the spirometric parameters is seen with higher values seen in the COPD group for both f_{res}

and $R_5 - R_{20}$. The previously mentioned increase in the resistive component of respiratory impedance at higher frequencies in healthy lungs is manifested here in a low or even negative value of $R_5 - R_{20}$, with negative values being particularly prevalent in the healthy group.

Once again an ANOVA test with a post hoc pairwise comparison was performed to ensure that the difference in the values of f_{res} and $R_5 - R_{20}$ between the patient groups was statistically significant. It was found that the patient group had a significant effect ($p<0.01$) on the values of both f_{res} and $R_5 - R_{20}$ demonstrating that these FOT values, as well as those evaluated using the aRIC model, could differentiate between patient groups in a similar way to spirometry. Again, the most significant difference was seen between the Healthy control group and the COPD group. This is to be expected as these are the groups with the largest difference in lung condition.

The mean and standard deviation for all measured parameters (both using spirometry and FOT) pre-BD is shown in Table 2.3 along with the p-values from the post hoc pairwise comparison. It is clear from this table that the most significantly different groups were the Healthy and COPD groups although several parameters such as FEV_1 and f_{res} differentiated between the healthy and asthma groups to the 1% significance level. Only FEV_1 had an equal level of significance between all three patient groups.

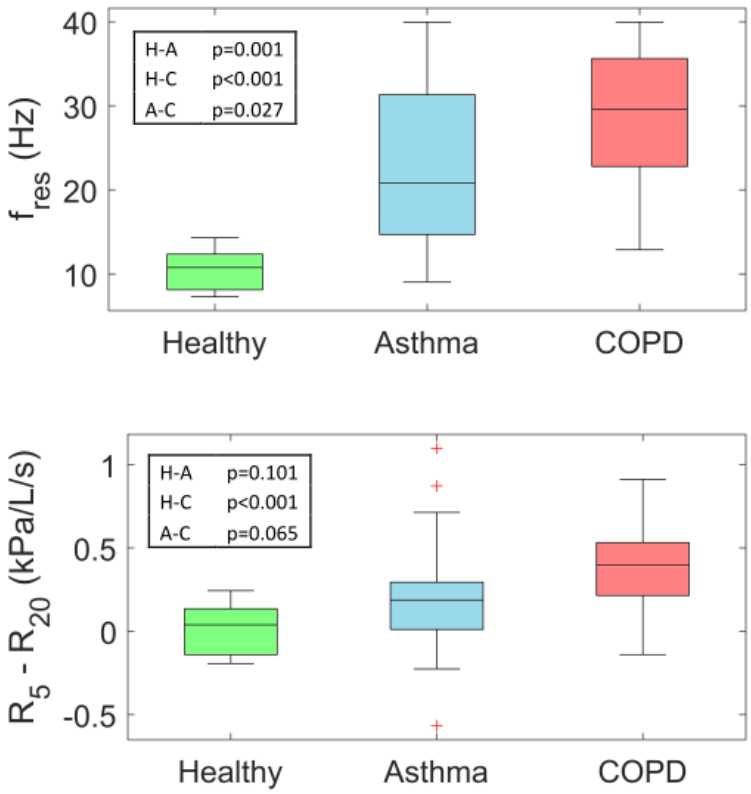


Figure 2.21: Box plots for the FOT parameters f_{res} and $R_5 - R_{20}$ measured pre-BD for each of the patient groups (outliers are marked with a red +).

Parameter	Healthy (n=10)	Asthma (n=26)	COPD (n=21)	p-value (H - A)	p-value (H - C)	p-value (A - C)
FEV_1 (L)	3.87 / 0.71	2.26 / 0.82	1.28 / 0.46	<0.001	<0.001	<0.001
FVC (L)	4.86 / 0.98	3.36 / 1.02	2.75 / 0.67	<0.001	<0.001	0.024
FEV_1/FVC	0.80 / 0.08	0.67 / 0.12	0.49 / 0.13	0.004	<0.001	<0.001
R_c (Ω)	0.59 / 0.28	1.23 / 0.68	1.58 / 0.61	0.006	<0.001	0.057
I (mH)	1.92 / 0.65	1.39 / 0.88	0.97 / 0.60	0.062	0.002	0.066
C_p (F)	0.16 / 0.04	0.07 / 0.04	0.04 / 0.03	<0.001	<0.001	0.065
f_{res} (Hz)	10.63 / 2.43	22.85 / 10.02	29.02 / 7.98	<0.001	<0.001	0.016
$R_5 - R_{20}$ (kPa/L/s)	0.01 / 0.15	0.21 / 0.36	0.39 / 0.26	0.078	0.002	0.047

Table 2.3: Mean and SD of measured pre-BD parameters (using spirometry and FOT) for all patient groups.

2.6.3 Effect of Bronchodilator on FOT

All patients underwent spirometry and FOT both before and after the administering of SABA. This was done to carry out the second aim of the study: to establish the effects of a BD on specific FOT parameters. Patients underwent spirometry pre- and post-BD in order for a comparison to be drawn. The values of the three spirometric parameters (FEV_1, FVC and FEV_1/FVC), pre- and post-BD, for the three patient groups are shown in Figure 2.22 with a line connecting the respective data points for each patient.

Although there is an amount of variability in the response of different patients to SABA a general trend of an increase in value for all three parameters can be seen in the patient groups. The only exception to this is that no significant change was observed in the value of FVC for the healthy volunteers. The healthy volunteers also had a lesser response to the SABA overall than either the asthma or COPD groups as would be expected. The asthma group exhibited the largest variation after the administering of the SABA which was similarly expected.

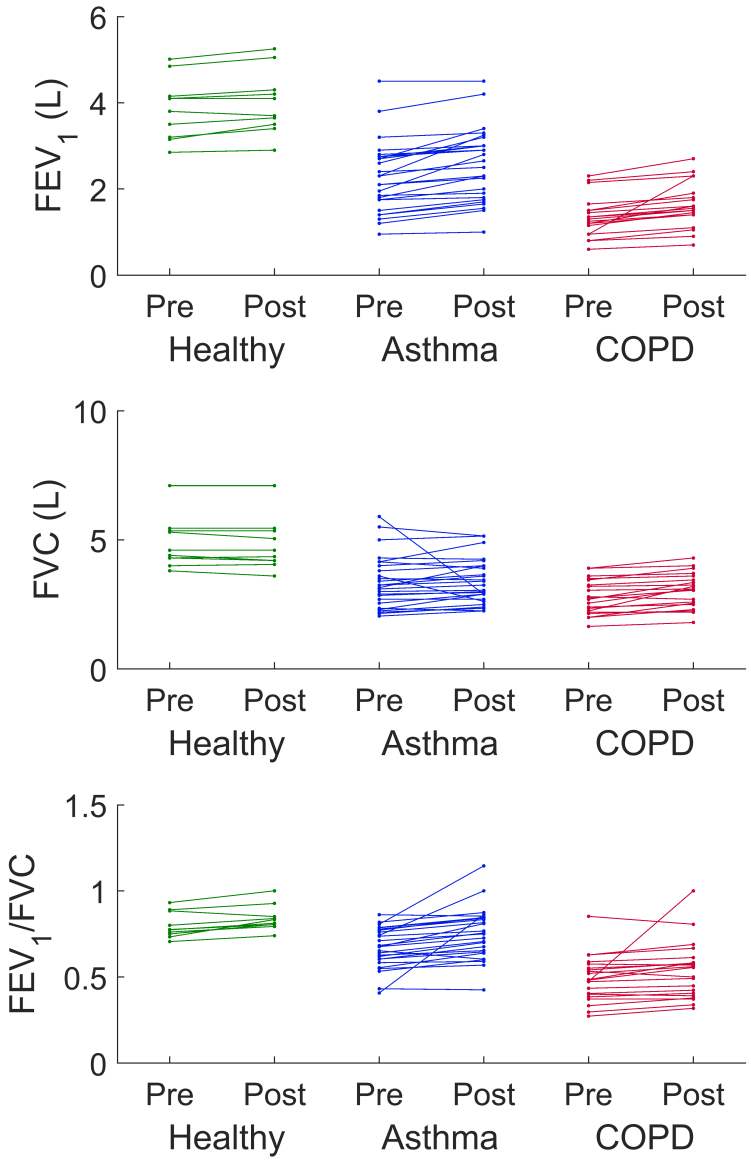


Figure 2.22: Values for the three spirometric parameters measured pre- and post-BD for the three patient groups.

Figure 2.23 shows the pre- and post-BD values of the three parameters measured by fitting the aRIC model to the data (R_c, I and C_p), for the three patient groups. The asthma group showed the largest response to the SABA across the three aRIC parameters in a comparable manner to the spirometric parameters. This is particularly noticeable in the measure of R_c, where the range of values post-BD is significantly smaller than the range of values pre-BD. However one key difference between the response seen in the spirometric data and the aRIC model data is that the aRIC data has much more variability in individual patient response. This was observed most strongly in the healthy group which, for the spirometric parameters, remained fairly constant however the aRIC model shows some significant changes in parameter values after the application of the SABA. Similarly, a large amount of change was seen in the aRIC parameters of some of the COPD patients that was not present in the spirometric measurements. This reinforces the idea that the parameters evaluated using FOT are measuring different aspects of lung condition to spirometry and that there is more than one condition in each of the patient groups resulting in different response to the SABA within the same group.

The values of f_{res} and $R_5 - R_{20}$ were also evaluated after the SABA was administered. The pre- and post-BD values of these parameters for all three patient groups is shown in Figure 2.24 with connecting lines indicating the change for each individual patient. Once again a general trend can be seen with patient lung condition improving after receiving the SABA. Again, the largest response can be seen in the asthma group, particularly for values of f_{res} where a reduction in the range as well as a reduction in mean value can be seen. This fits the classical view of asthma as a reversible disease. However the presence of a change in the COPD group goes against the classical view of COPD as an irreversible disease.

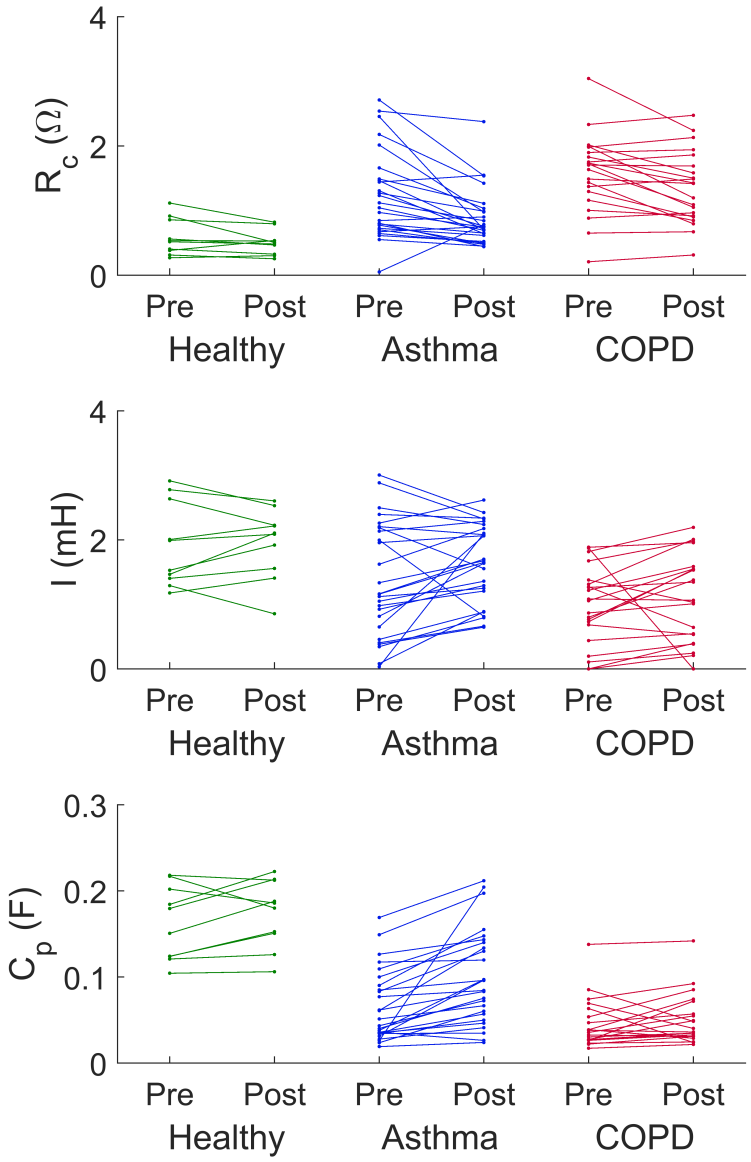


Figure 2.23: Values for the three aRIC model parameters measured pre- and post-BD for the three patient groups.

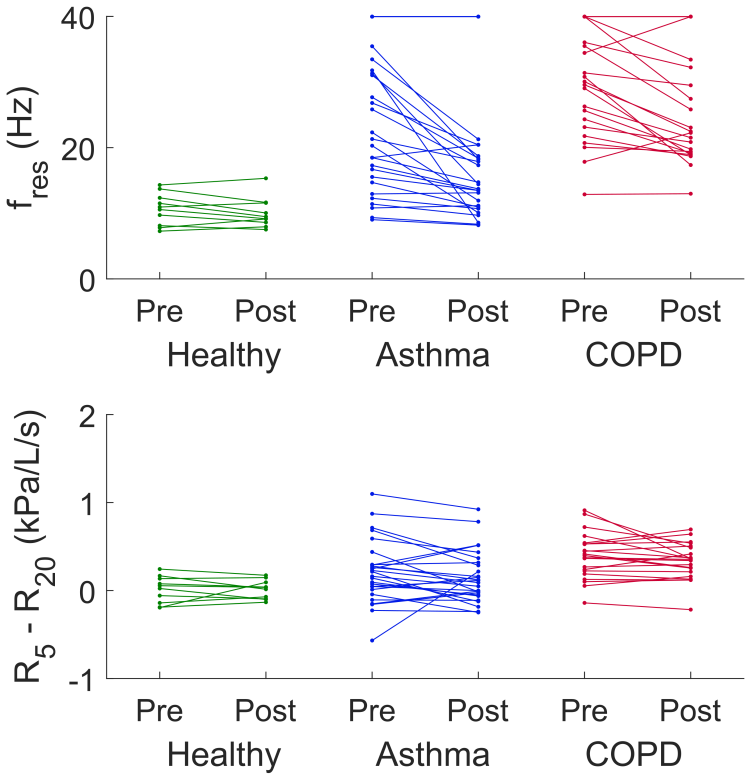


Figure 2.24: Values for the FOT parameters f_{res} and $R_5 - R_{20}$ measured pre- and post-BD for the three patient groups.

The response of the asthma patient group to SABA is shown in Table 2.4 which shows the mean and standard deviation for each parameter pre- and post-BD. A paired t-test was performed to determine the significance of the response to SABA. It can be seen that there was a highly significant change in FEV_1, FEV_1/FVC, R_c, C_p and f_{res} with a less significant but still substantial response seen in I. There was limited significance in the response measured with $R_5 - R_{20}$ and no response seen in FVC. This demonstrates that all patient parameters, with the exception of $R_5 - R_{20}$, are useful in detecting patient response to SABA.

Parameter	Pre-BD (n = 26)	Post-BD (n = 26)	p-value
FEV_1 (L)	2.26 / 0.82	2.55 / 0.84	<0.001
FVC (L)	3.36 / 1.02	3.37 / 0.86	0.928
FEV_1/FVC	0.67 / 0.12	0.75 / 0.15	0.001
R_c (Ω)	1.23 / 0.68	0.87 / 0.44	0.001
I (mH)	1.39 / 0.88	1.60 / 0.61	0.053
C_p (F)	0.07 / 0.04	0.10 / 0.05	<0.001
f_{res} (Hz)	22.85 / 10.02	17.12 / 9.28	<0.001
$R_5 - R_{20}$ (kPa/L/s)	0.21 / 0.36	0.15 / 0.30	0.242

Table 2.4: Mean values of measured parameters pre- and post-BD for the asthma patient group displayed as mean/SD.

The difference patient response between groups, as observed using different parameters, can be demonstrated by reviewing the mean difference observed in each of the measured parameters, pre- and post-BD. Table 2.5 contains the mean and standard deviation for the difference observed in all eight parameters for all three patient groups. An ANOVA test with a post-hoc pairwise pair-

wise comparison was performed to calculate the significance of patient response between groups. The p-values from the test are shown in the table.

It can be seen that there were responses detected in all three patient groups with different parameters detecting different levels of response between the groups. An example of this heterogeneity is shown in the contrast between C_p and f_{res}. In the case of C_p, there is a significant difference between the asthma group and the other two groups. On the other hand, although the healthy group also had a small mean difference in f_{res}, a much larger difference was observed in both the asthma and COPD groups. This difference in the responses of the patient groups between parameters demonstrates that there is more than one possible response to SABA within disease states, such as bronchodilation or a reduction in dynamic hyperinflation. The change in the reactive component of respiratory impedance with improvement in dynamic hyperinflation has previously been shown by Dellaca et al. [52].

Parameter	Healthy (n=10)	Asthma (n=26)	COPD (n=21)	p-value (H - A)	p-value (H - C)	p-value (A - C)
ΔFEV_1 (L)	0.13 / 0.13	0.29 / 0.25	0.26 / 0.27	0.090	0.147	0.0821
ΔFVC (L)	-0.07 / 0.11	0.01 / 0.71	0.26 / 0.25	0.687	0.118	0.125
$\Delta FEV_1/FVC$	0.04 / 0.03	0.08 / 0.11	0.05 / 0.11	0.282	0.743	0.365
ΔR_c (Ω)	-0.08 / 0.16	-0.36 / 0.48	-0.22 / 0.33	0.058	0.410	0.194
ΔI (mH)	0.03 / 0.37	0.26 / 0.64	0.13 / 0.58	0.243	0.403	0.718
ΔC_p (F)	0.01 / 0.03	0.03 / 0.04	0.01 / 0.02	0.047	0.729	0.005
Δf_{res} (Hz)	-0.59 / 1.39	-5.73 / 6.50	-4.08 / 4.99	0.011	0.094	0.301
$\Delta R_5 - R_{20}$ (kPa/L/s)	-0.002 / 0.12	-0.06 / 0.26	-0.06 / 0.18	0.465	0.429	0.901

Table 2.5: Mean and SD of the difference in measured parameters (using spirometry and FOT) pre- and post-BD for all patient groups.

The efficacy of FOT in measuring patient response to SABA in comparison to spirometry was assessed by plotting the difference in measure parameters for the asthma patient group against the percentage change in FEV_1. It is not appropriate to consider the percentage change in FOT parameters as some of the parameters have a very low value that can be negative ($R_5 - R_{20}$). It can therefore be the case that the pre-BD value for a patient could be zero resulting in any change being an infinite percentage change. These plots are shown in Figures 2.25 and 2.26 with Figure 2.25 showing the three aRIC model parameters (R_c, I and C_p) and Figure 2.26 showing the FOT parameters f_{res} and $R_5 - R_{20}$. Pearson's correlation coefficient was calculated for each comparison.

Substantial correlation was seen between ΔR_c and ΔFEV_1 (p=0.006) with less significant correlation seen between ΔC_p and ΔFEV1 (p=0.117). This indicates that these parameters measure SABA response in a comparable manner to FEV1. There was no significant correlation seen between ΔI and ΔFEV_1 (p=0.771) suggesting that either I is not a good detector of SABA response or that the response detected by I is a different patient response to the response detected by FEV_1. Δf_{res} and $\Delta R_5 - R_{20}$ showed some correlation with ΔFEV_1 (p = 0.088 and 0.196 respectively) indicating a similarity in patient response detection between the FOT and spirometric parameters. However, there is some variation in the responses detected by each method that again suggests that FOT is measuring a different form of SABA response to spirometry. The fact that a significant patient response was observed in the asthma group for all FOT parameters (Table 2.4) suggests that any lack of correlation between a spirometric response and an FOT response is due to the nature of the measured response rather than a lack of response detection.

The observation that FOT can provide additional information to spirometry about BD response has been previously documented by Yaegashi et al. [59].

However, although this data demonstrates that FOT can provide information about patient response to BD that cannot be measured with spirometry, the opposite is also true with spirometry providing additional information to just FOT.

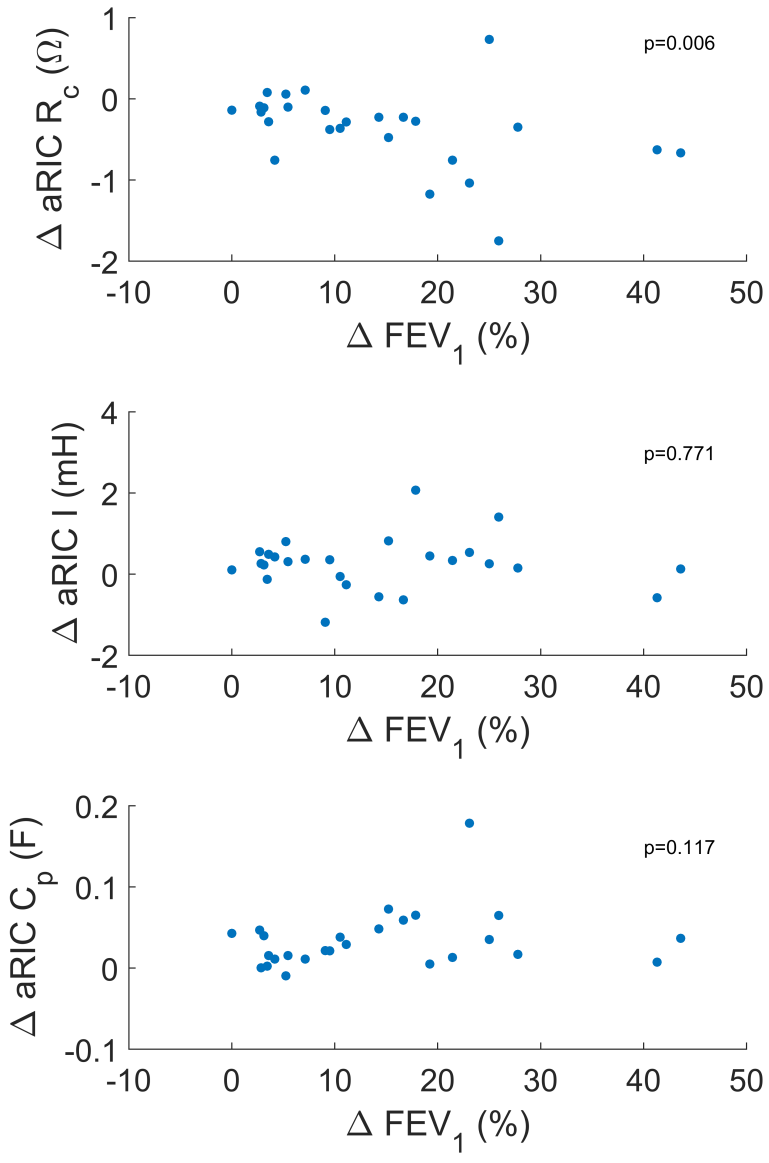


Figure 2.25: Difference in aRIC model parameters against the percentage change in FEV_1 for the asthma patient group. Pearson's correlation coefficient was calculated for each parameter with p = 0.006/0.771/0.117 for $R_c/I/C_p$ respectively.

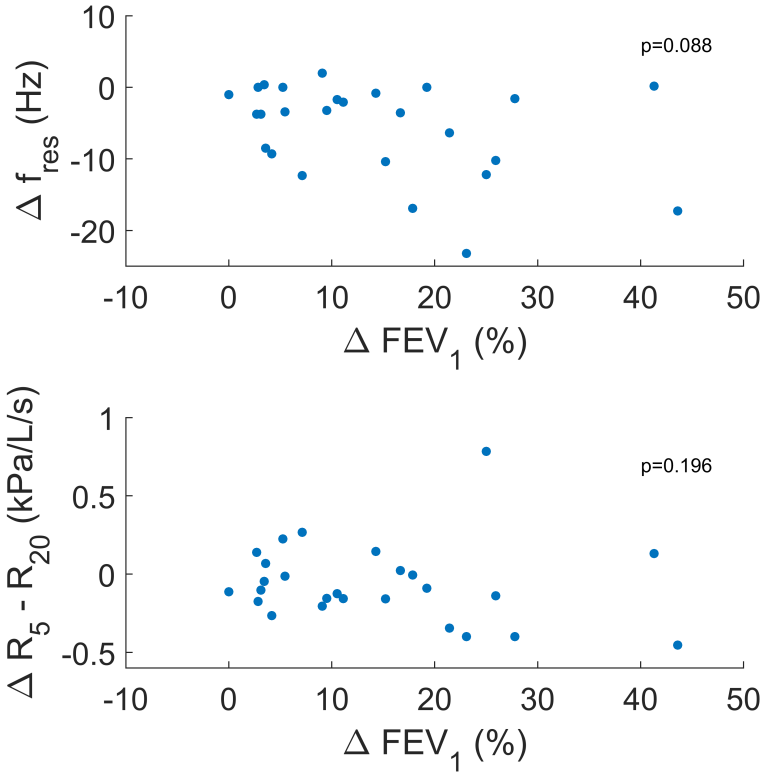


Figure 2.26: Difference in FOT parameters f_{res} and $R_5 - R_{20}$ against the percentage change in FEV_1 for the asthma patient group. Pearson's correlation coefficient was calculated for each parameter with p = 0.088/0.196 for $f_{res}/R_5 - R_{20}$ respectively.

2.7 Conclusion

A phantom study and a patient were undertaken to investigate FOT. The phantom study had three aims: firstly, to verify the validity of the Nottingham FOT system; secondly, to explore the effect of a change in resistance or compliance on FOT parameters; and thirdly, to compare three different FOT systems (including the Nottingham system).

The Nottingham FOT system was calibrated using a known standard resistance. The reactance of the system was validated using a 50L barrel which could be treated as a Helmholtz resonator. As the experimental data matched the theoretical reactance of a Helmholtz resonator of the same dimensions as the Barrel phantom we can have confidence in the reliability of the Nottingham FOT system's measurements.

The effect of lung compliance and obstruction on FOT measures was investigated using a phantom consisting of a 3-D printed airway containing the first seven generations of the upper airways housed in a plastic cylinder with a rubber sheet at the base representing the diaphragm. The tension in the diaphragm could be adjusted to vary the compliance of the lung whilst airway openings could be occluded to simulated obstructive airways disease. It was found that there was a strong correlation between lung compliance and the FOT parameters f_{res} and C_p (evaluated by fitting the aRIC model to the data). The phantom was systematically occluded to simulate the effects of lung obstruction. It was found that increased obstruction had an affect on resistive measures of impedance, particularly R_c, R_5, R_{20} and $R_5 - R_{20}$, particularly after 40 occlusions for R_c, R_5 and R_{20}. There was no observed change in the reactive component of impedance as a result of the obstructions. This demonstrates that the resistive and reactive FOT parameters are not random but do directly relate to the resistance and compliance (respectively) of a system.

A comparison was made between three different FOT devices across two sites (an in-house device in Nottingham, an Erich Jaeger MasterScreen IOS and a tremoFlo C-100 airwave oscillometry system both in Leicester). These devices were used to measure the reactance of a 3L syringe as well as the 3-D printed airway system at different levels of obstruction. The continuous wave devices (Nottingham and tremoFlo) operated in different ways with the tremoFlo device using a fan to produce the oscillations rather than a loudspeaker. However this difference in technique produced no significant difference in measurements between the two systems for both the reactive measure (the 3L syringe) and the resistive measure (the obstructed printed airway). This similarity was highlighted by a measurement taken using the tremoFlo device on the Barrel Phantom. Although more rigorous testing needs to be performed, the initial value for f_{res} was 8.59 Hz for the tremoFlo which closely matches the measurement of $f_{res} = 8.32$ Hz measured using the Nottingham device. On the other hand, the Jaeger system was an IOS system using impulses instead of continuous waveforms and showed marked differences between the other two devices in both resistive and reactive measures. One explanation for this difference could be that there is a non-linear relationship between the measured impedance and the peak pressure of the applied sound waves that causes Z to decrease as pressure increases. An IOS system can be expected to have a higher peak pressure than a continuous waveform in which the peak pressure can be adjusted by varying the phase difference between the component sinusoids. Further investigation into the peak pressures applied by IOS and FOT devices would be needed to confirm this explanation.

A patient study was undertaken to investigate the effects of SABA on the parameters measured using FOT, in comparison to spirometry. The main aims were to confirm that FOT can differentiate between different disease states; investigate the differences in values of measured FOT and spirometric parameters

pre- and post-BD; and to determine whether the different measured parameters were detecting different patient response to SABA.

57 patients (26 asthma, 21 COPD and 10 healthy volunteers) had spirometry and FOT measurements taken before and after a SABA was administered. The measured parameters looked at in the patient study were: FEV_1, FVC, FEV_1/FVC (measured using spirometry), R, I and C_p (evaluated by fitting the aRIC model to FOT data) and f_{res}, $R_5 - R_{20}$ (evaluated using the Mead model fitted to FOT data). The aRIC model provided the most meaningful fitting data, whilst the Mead model provided the best fit and so was used to evaluate f_{res} and $R_5 - R_{20}$.

It was found that all of the measured parameters were effective at discriminating between patient groups. The most significant differences were seen between the Healthy group and the COPD group ($p<0.001$ all measured parameters except I and $R_5 - R_{20}$ where $p=0.002$). This demonstrates that FOT is as effective as spirometry in differentiating between these disease states.

The patient response to SABA for all measured parameters was investigated by performing spirometry and FOT measurements pre- and post-BD. The difference between these measurements was investigated. For the asthma group it was found that there was a significant change ($p<0.001$) for all parameters except FVC, I and $R_5 - R_{20}$ ($p = 0.928$,0.053 and 0.242 respectively). This demonstrates that FOT and spirometry are both effective in measuring response to SABA. A heterogeneity was seen in BD response between the patient groups with respect to measured parameter. This was most notably manifested in the FOT parameters C_p and f_{res} for which the most significantly different patient groups (according to BD response) were asthma and COPD respectively. This difference suggests that these parameters are measuring different patient response to SABA that potentially cannot be investigated using spirometry.

The difference in patient response between spirometric and FOT parameters was further explored by plotting the difference in FOT parameters against the percentage change in FEV_1. It was found that R_c was most similar to FEV_1 (p=0.006) whilst I was the least correlated (p=0.771). The variety in correlation between the FOT parameters and FEV1 suggests that there is a difference in observed response as a response was seen by all FOT parameters in the patient group. This has clinical significance as understanding how a patient will respond to SABA allows for treatment to be tailored to a patients specific requirements. It was observed that although FOT provided information about patient response that was not observable using spirometry, the opposite was also true. Therefore, in order to gain the largest amount of information about a patients condition, both FOT and Spirometry would have to be carried out.

Chapter 3

Hyperpolarised Gas Magnetic Resonance Imaging

3.1 Introduction

Lung imaging has always been difficult due to the diffuse nature of lung tissue. Although it is possible to image some features of the lungs using X-ray CT or ultrashort echo time (UTE) ^{1}H MRI, this is only diagnostically useful for developed lung diseases. Various techniques are being developed to try to image the lungs in different ways in the hope of achieving an earlier diagnosis. One of these techniques is to apply a gaseous contrast agent in the form of a hyperpolarised (HP) gas such as ^{3}He or ^{129}Xe (both of which are considered in this thesis).

The main use of HP gas MRI is in ventilation imaging in which the distribution of the gas through the lungs during or after inhalation is imaged. This

distribution should be relatively homogeneous in a healthy set of lungs; however, if the patient has obstructed airways the gas will be unable to reach all areas of the lung resulting in dark regions of no signal appearing on a ventilation image. The lung disease can then be categorized by observing the morphology, distribution, and time dependence of these obstructed regions. Another common form of lung imaging using HP gas MRI is diffusion weighted imaging. This utilizes the fact that a gaseous contrast agent will move around the lung after inhalation. If the lung has a large number of small structures (in the form of undamaged alveolar sacs) then diffusion will be limited, in contrast to lungs in which there is a breakdown in lung structure when diffusion is higher. Measuring the diffusion within the lung can be clinically significant without forming an image. A third imaging modality, called dissolved phase imaging, is unique to HP ^{129}Xe MRI. Xe gas dissolves into the bloodstream along the same pathways as oxygen and is visible in both the blood and the parenchyma. This allows the gas exchange surface to be imaged which provides additional information over ventilation imaging as it is possible for a region to be ventilated without gas exchange occurring.

Two ongoing studies are discussed in this chapter, one using HP ^{3}He and one using HP ^{129}Xe. The ^{3}He study focussed on measuring lung diffusion in healthy adolescents and comparing the results to data from the same subjects scanned at a second site, the University of Sheffield. The main aim of this study was to compare the similarities in ADC measurements at two different time scales between the two sites but a secondary objective was to investigate a potential link between lung diffusion and age. The ^{129}Xe study is still in the early development stages and aims to investigate various imaging techniques, such as dynamic imaging, to verify the reliability of the modality before the study can be expanded into imaging patients with lung disease.

3.2 Theory

3.2.1 Nuclear Magnetic Resonance

Larmour Frequency

Protons and neutrons have an intrinsic magnetic moment due to their spin. It is therefore the case that nuclei with a non-zero spin (including ^{1}H, ^{3}He, ^{13}C and ^{129}Xe) have a net magnetic moment. In the presence of a large magnetic field (B_0), this moment will experience a torque causing the magnetic moment to rotate around the axis of the B_0 field. The angle between the magnetic moment and B_0 will remain constant unless another force acts on the system [61]. This process is called precession and is illustrated in figure 3.1.

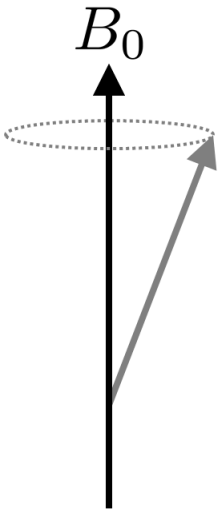


Figure 3.1: Precession of a nuclear magnetic moment in a strong magnetic field (B_0)

The angle between B_0 and the magnetic moment is dependant on the spin polarisation when the B_0 field is introduced. If the polarisation was exactly along or against B_0 when it was introduced then there will be zero angle, whereas

if the B_0 field is perpendicular to the moment then the precession will occur at a 90° angle to B_0, in a flat circle rather than in a conical shape. The frequency of precession is called the Larmor frequency (ω_0) and is is given by

$$\omega_0 = \gamma B_0, \tag{3.1}$$

where γ is the gyromagnetic ratio. The important thing to notice is that the Larmor frequency is proportional to the magnetic field strength [61].

Polarisation

The magnetic moment of each nucleus in the system (once the B_0 field has been applied) will exist in one of two states: either it will be parallel with the B_0 field or it will be anti-parallel. This is dependant on whether the moment is in the spin-up ($S = +\frac{1}{2}$) or spin-down ($S = -\frac{1}{2}$) energy level where the difference in energy between these two states is directly proportional to the strength of the B_0 field. At any time a nucleus can move from one state to the other by receiving or releasing energy [61].

As one of the spin states is more energetically favourable, it will be the case that there will be a difference in the number of nuclei in each spin state. This difference means that the system has a polarisation. Although this polarisation will occur naturally it can be greatly increased by methods such as optical pumping that can cause the majority of the nuclei to be in one state. When the system is in this enhanced state it is referred to as being hyperpolarised (HP) [62].

Net Magnetisation and Spin-Lattice Relaxation

When the B_0 field is first applied to the system, the net magnetisation is very low as there will be relatively uniform spin distribution however this distribution

is not stable as all the separate magnetic moments interact with each other. These interactions are small and fluctuate due to thermal motion, but are still large enough to cause the angle between the magnetic moment of each nuclei to change over a period of time. As it is more energetically favourable for the magnetic moment to be parallel with B_0, the net distribution of spins will gradually shift to be in line with B_0. This process is known as spin-lattice relaxation. This, coupled with the polarising effect described earlier, gives rise to a small net magnetic moment along the field which is known as the longitudinal magnetic moment.

The build up over time (t) of the net magnetisation (M) when the B_0 field is applied to a system at equilibrium is described by the following equation [61].

$$M_z(t) = M_{eq}(0)\left(1 - \exp\left(\frac{-t}{T_1}\right)\right), \tag{3.2}$$

where z is the direction of the B_0 field and T_1 is the spin-lattice relaxation time constant. Similarly when the B_0 field is removed then the net magnetisation will decay in the following manner,

$$M_z(t) = M_{eq}(0)\exp\left(\frac{-t}{T_1}\right). \tag{3.3}$$

The relaxation time T_1 depends on the nuclear isotope as well as the state of the sample, including parameters such as temperature and viscosity [63].

Transverse Magnetisation

The longitudinal magnetic moment is many orders of magnitude smaller than the B_0 field and therefore is very difficult to detect. For this reason the net magnetisation of the sample is detected perpendicular to the field during NMR spectroscopy. In order to "tip" the longitudinal magnetic moment into the

transverse plane, a second magnetic field (B_1) is applied to the system. The B_1 field oscillates at the same frequency as the Larmor frequency of the sample, thus providing a large amount of energy despite the fact that B_1 has a weaker field strength than B_0. The time when the B_1 field is acting on the system is known as the radio frequency (r.f.) pulse [64].

Once the net magnetisation has been tipped into the transverse plane, it will continue to precess around the z axis. The precession frequency of the transverse magnetic moment is the same as the Larmor frequency of the component spins.

Transverse Relaxation

It was previously remarked that there are small fluctuations in the field strength that result in spin-lattice relaxation. These fluctuations cause the individual magnetic moments that make up the transverse magnetic moment to precess at different rates. As a result they go out of phase with each other causing the transverse magnetic moment to decay. This process is called transverse relaxation. The transverse magnetisation, M, at a time, t, after an r.f. pulse in the x and y directions are given by equations 3.4 and 3.5 [61].

$$M_y = -M_{eq} \cos(\omega_0 t) \exp\left(\frac{-t}{T_2}\right). \tag{3.4}$$

$$M_x = M_{eq} \sin(\omega_0 t) \exp\left(\frac{-t}{T_2}\right). \tag{3.5}$$

Where ω_0 is the Larmor frequency and T_2 is know as the "transverse relaxation time constant" or the "spin-spin relaxation time constant". Transverse relaxation is irreversible as it is due to microscopic fluctuations in field strength, however there are often macroscopic variations in field strength that cause the transverse magnetic moment to decay at a faster rate than expected. It is therefore the case that an effective T_2 parameter is used (denoted T_2^*) to describe the

situation where the effect of macroscopic inhomogeneities in field strength are included in the time constant. This effect is reversible in some situations (see Section 3.2.2).

Free-induction Decay

After an r.f. pulse there is a net transverse magnetisation that precesses around the z axis. The signal amplitude is still small (relative to B_0) as tipping the magnetisation from the longitudinal plane to the transverse plane has no effect on the amplitude of the signal. However, as the signal is now oscillating at a known frequency, it can be detected through a coil placed near the sample. This is the NMR signal or free-induction decay (FID) [64].

This signal decays through both spin-lattice and transverse relaxation simultaneously, but it is the transverse relaxation that is usually the more dominant effect, especially if there are macroscopic inhomogeneities. Spin-lattice relaxation is also known as T_1 recovery as this process recovers the longitudinal magnetisation; this allows repeat signals to be acquired through the application of further r.f. pulses. Images taken using this technique can be weighted towards T_1 or T_2 by varying the recovery time, pulse time and detect times.

NMR Spectroscopy

The form of the NMR signal seen after an r.f. pulse is shown in Figure 3.2.

By carrying out a Fourier transform on this signal we get a simple Lorentzian peak with the centre of the peak at ω_0 as shown in Figure 3.3.

In the case of a sample containing multiple nuclei of the same isotopes, but in different environments, the nuclei will have different Larmor frequencies in the same B_0 field, and so the NMR spectrum will have multiple peaks relating

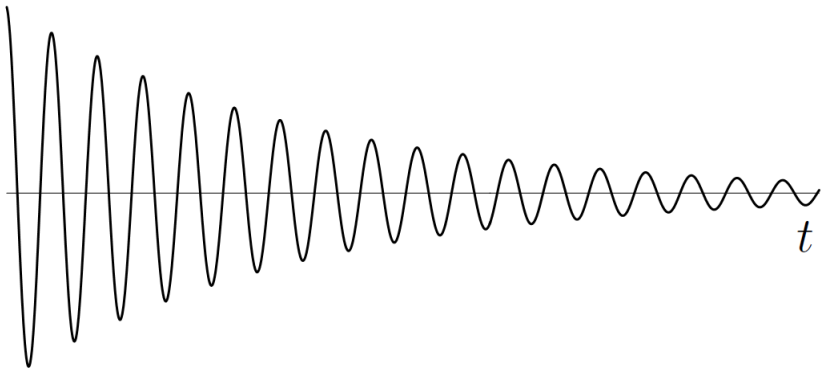


Figure 3.2: NMR Signal decaying over time

to the different environments in which the nuclei exist. Spectra produced using NMR can be used to identify unknown substances [64, 61, 63].

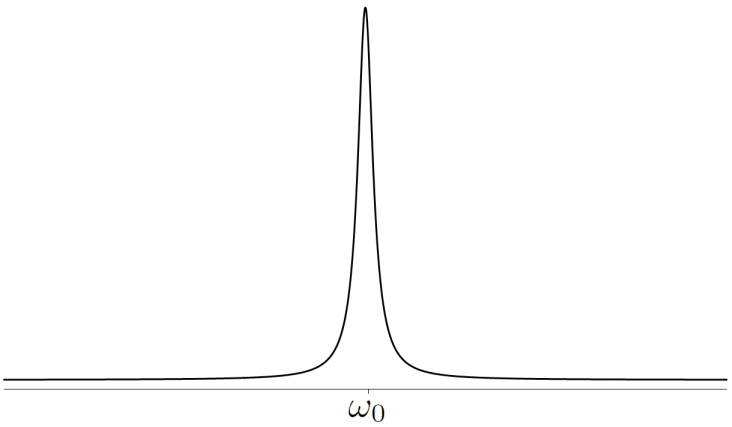


Figure 3.3: Fourier transform of simple NMR signal

3.2.2 Magnetic Resonance Imaging

Gradient Coils

An important feature of NMR spectroscopy is that if the B_0 field is not homogeneous, then the Larmor frequency of the nuclei in a sample will no longer be independent of position. This can be exploited by adding a gradient to the otherwise homogeneous B_0 field such that

$$\omega_0(x) = \gamma B_0(x), \tag{3.6}$$

assuming the gradient has been applied in the x direction. The addition of gradient coils in all three planes allows a 3D image to be formed using NMR [63].

Frequency Encoding

In order to produce an image the gradient coils need to be switched on and off at the correct times during a scan. A gradient applied during the r.f. pulse will have a different effect to a gradient applied during signal acquisition. By

combining these different effects an image can be created.

Frequency encoding refers to the situation in which a gradient has been applied during signal acquisition. This splits the detected NMR signal into a spectrum that is dependant on the location of the precessing nuclei. As a result all spacial frequency information in one dimension can be acquired simultaneously as the presence of the gradient coil causes the transverse magnetisation to precess at different frequencies along the gradient.

Frequency encoding can only be used to acquire spacial information in one dimension as, if the same technique were applied in a second dimension, there would be no way of knowing in which direction the frequency offset from the gradient came from. Instead a second dimension is added using phase encoding [63].

Phase Encoding

Whilst frequency encoding arises from a gradient during signal acquisition, phase encoding comes from applying a gradient immediately before acquisition. The purpose of this gradient is to cause the precession of the nuclei along the gradient to go out of phase with each other. When the gradient is switched on, the precessions go out of phase; then, when the gradient is switched off, the precessions remain "locked" in the same phase. The sample has been phase encoded. This process is illustrated in Figure 3.4.

The severity of how much the signal will go out of phase is determined by the strength of the phase encoding gradient (G_{PE}). If G_{PE} is small there will only be a small variation in phase along the gradient, whereas a large G_{PE} will cause a larger variation in phase. A large variation in phase will result in a drop in signal amplitude. The closer a nuclei is to the isocentre of the magnet, the smaller the effect of the gradient on that nuclei, irrespective of the

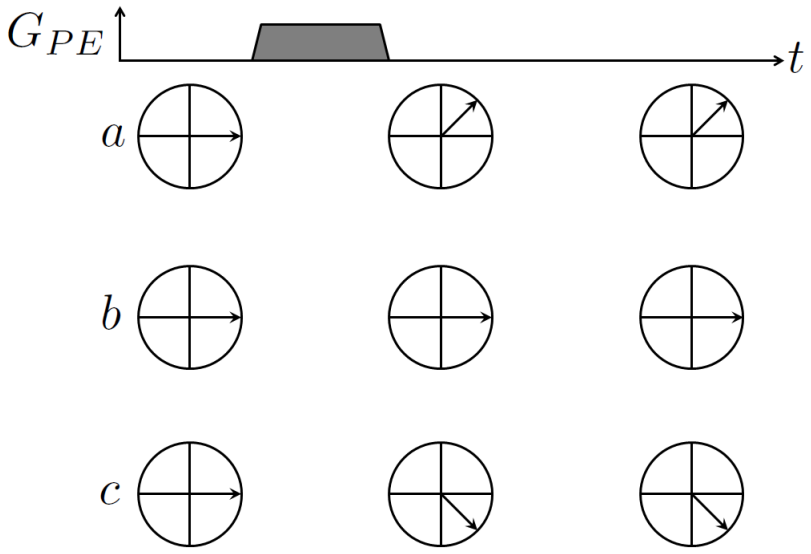


Figure 3.4: The process of phase encoding where a, b and c are nuclei in a line in the direction of the phase encoding gradient (G_{PE}). Initially a, b and c are precessing in phase. When G_{PE} is switched on a, b and c precess at different rates causing them to go out of phase. When G_{PE} is switched off the nuclei process at the same frequency again and so remain in the same phase.

strength of G_{PE}. This allows spacial information to be acquired by comparing the phase difference at different strengths of G_{PE}. This is done by carrying out a Fourier transform that converts the change in phase, due to the gradient coil, to the relative difference in phases between different strengths of G_{PE}. As the difference in phase between the different applied gradient strengths is directly related to the relative location of the nuclei to the isocentre of the magnet, the Fourier transform provides spatial information in one dimension.

The spatial resolution of the image produced is dependant on the number of phase encoding gradients applied. A large number of gradient strengths need to be applied in order to acquire an image with good spacial resolution. As the

phase encoding gradient is applied between the r.f. pulse and signal acquisition, the entire process needs to be repeated for each acquisition (i.e. for 256 bits of information, 256 r.f. pulses are required). By combining phase encoding with frequency encoding a 2D image can be created, as frequency encoding provides spacial information in one dimension. Phase encoding could be used to create a 2D image (without frequency encoding) by repeating the process in a different direction however this would be very slow in comparison to frequency encoding as the required number of r.f. pulses would be equal to the number of pixels in the image (i.e. a 256x256 image would require 65,536 r.f. pulses rather than the 256 r.f. pulses required if frequency encoding is used) [61].

Slice Selection

The addition of a third dimension, to go from pixels to voxels, is done using a slice select gradient applied during the r.f. pulse. Once again this gradient causes the nuclei to precess at different frequencies. As a result any nuclei precessing outside of the bandwidth of the r.f. pulse will be off resonance and therefore will not be excited and as such will not produce a signal. Therefore the image produced using the other two gradients will be of a slice of the sample.

The slice select gradient provides no additional spacial information other than to dictate the thickness of the slice being imaged. To create a fully 3D image a series of slices need to be imaged sequentially and then recombined later. In some cases, this gradient is not applied so that the thickness of the slice is infinite, which provides a projection of the entire sample in 2D.

A graphical summary of the timings of the three gradients is shown in Figure 3.5. It can be seen that the slice select gradient (G_{SS}) activates first, during the r.f. pulse, with the phase encoding gradient (G_{PE}) activating second before the signal acquisition when the frequency encoding gradient (G_{FE}) is active.

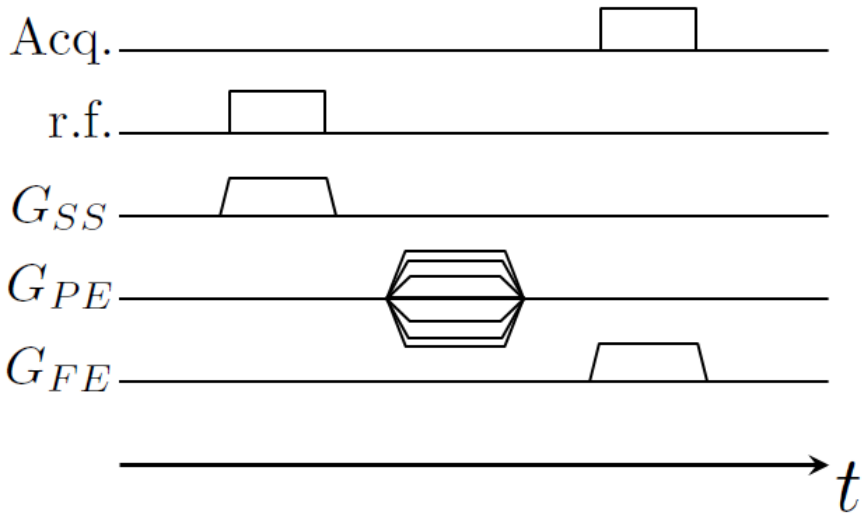


Figure 3.5: A graphical representation of the timing of the slice select (G_{SS}), phase encoding (G_{PE}) and frequency encoding (G_{FE}) gradients in relation to the r.f. pulse and signal acquisition.

In order to produce an image, a sequence of r.f. pulses and gradients is used. Some sequences are more complicated than others and some sequences are better suited to certain forms of imaging than others. Whilst there are many different sequences they can all be grouped into two categories: spin echo sequences and gradient echo sequences [63].

The Spin Echo Sequence

It was previously mentioned that any macroscopic inhomogeneities in the magnetic field strength will cause transverse decay to occur at a faster rate than expected requiring the use of the notation T_2^* (referring to the shortened T_2 time). The spin echo sequence reverses this effect and allows the true T_2 value to be evaluated.

Immediately after the initial 90° r.f. pulse, the magnetic moments of the excited nuclei are all in phase with each other causing a net transverse magnetic moment. Inhomogeneities in the B_0 field cause some magnetic moments to precess at a faster frequency and some to precess at a slower frequency. This brings them out of phase causing the signal to rapidly disappear as the faster precessing moments lead and the slower precessing moments lag.

If a further 180° r.f. pulse is applied, the magnetic moments will be flipped. As a result the faster precessing moments will lag, and the slower precessing moments will lead. As all magnetic moments will continue to precess at the same frequency they were precessing before the 180° r.f. pulse (as the inhomogeneities are fixed), they will momentarily come back into phase. This will bring back the signal that was lost due to T_2^* but, as T_2 decay is irreversible, the amplitude of the signal will be lower than it was previously. As time continues the magnetic moments will proceed to go out of phase again as they are still precessing at different frequencies. However the 180° flipping process can be repeated multiple times until the signal is lost due to T_2 decay and T_1 recovery [65]. The process of recovering the true T_2 value using a spin echo sequence is shown in Figure 3.6.

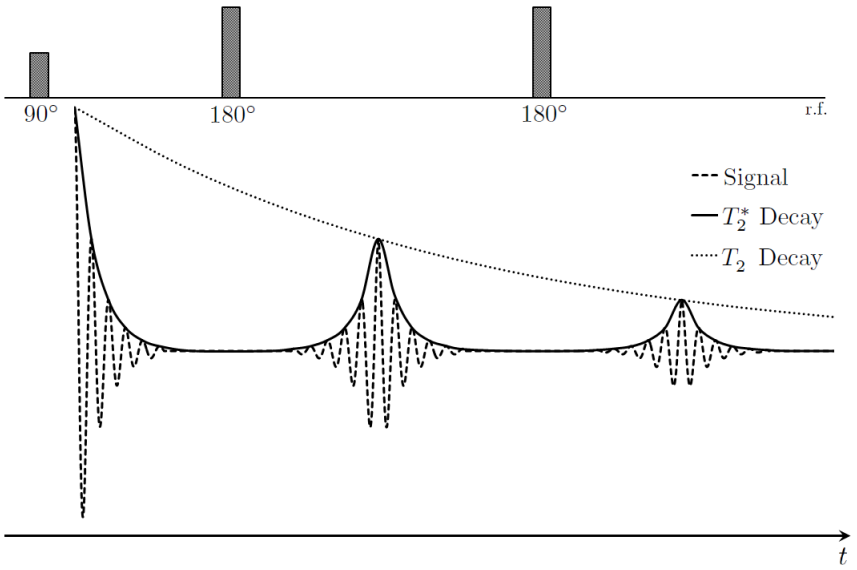


Figure 3.6: Acquisition of the true value of T_2 using a spin echo sequence

The Gradient Echo Sequence

The other main form of sequences are gradient echo sequences. These sequences begin with an r.f. pulse with a slice select gradient applied (unless a projection is wanted). A dephasing gradient is then applied in the frequency encoding plane before acquisition (at the same time as a phase encoding gradient). This dephasing gradient causes the magnetic moments out of phase at a significantly faster rate than transverse relaxation alone. The dephasing gradient is then inverted to bring the moments back into phase (in the same way as the 180° pulse in the spin echo sequence) producing an echo. The timing of this sequence is shown in Figure 3.7. As the rephasing gradient only recovers the signal loss from the dephasing gradient and not field inhomogeneities the rate of transverse relaxation will be dependant on T_2^* instead of T_2.

A significant feature of the gradient echo sequence is that the flip angle of the r.f. pulse can have any value, not just 90°. By using a smaller flip angle the

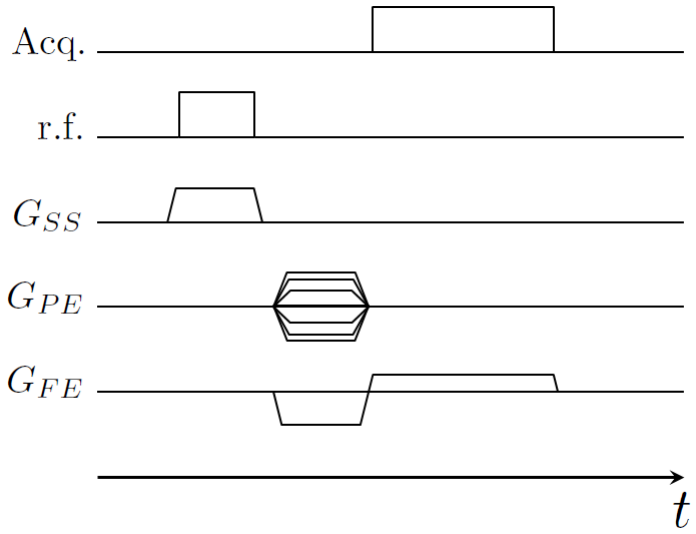


Figure 3.7: The gradient echo sequence

longitudinal magnetic moment will recover faster allowing for faster imaging. This is also essential for hyperpolarised imaging where the longitudinal magnetisation is non recoverable. More images can be acquired per sample by using a smaller flip angle [64, 61, 63].

3.2.3 Gas Polarisation

Motivation for Polarisation

The majority of clinical MRI looks at the ^{1}H in the body. This is because ^{1}H is present in water, fat, protein and all other fluids and parts of the body in abundance. The large quantity of ^{1}H in different states gives a large NMR signal allowing for detailed images to be created. However one area of the body that presents great difficulties in imaging in detail using ^{1}H MRI is the lungs as the lungs should be full of air which does not produce an NMR signal. In order to image the lungs using MRI, a contrast agent must be introduced which must be a non-toxic gas with a non-zero nuclear spin ground-state with a short T_2

time. Both ^{3}He and ^{129}Xe fit this description.

The issue with using these gases is that their low density (in comparison to solids or liquids) means that, in a clinical setting, the signal produced is too small to be of value. Whilst the density could be increased by increasing the gas pressure, a process that can be performed using a phantom, this is not a viable technique for *in vivo* studies.

It was previously mentioned that the strength of the net magnetic moment (and therefore the NMR signal intensity) is dependant on the polarisation of the sample. This can be increased beyond its equilibrium state (hyperpolarised) to increase the NMR signal. In the case of ^{3}He and ^{129}Xe the gas density is approximately three orders of magnitude smaller than that of organic tissue. However, the processes of hyperpolarisation can increase the signal intensity by a factor of 10^{5}. There are two methods of hyperpolarising the gases used: spin exchange optical pumping (SEOP) [62] and metastable exchange optical pumping (MEOP) [66, 67]. Both gases can be hyperpolarised using SEOP whereas MEOP can only be used to hyperpolarise ^{3}He.

Although HP ^{3}He and ^{129}Xe have incredible potential in lung imaging they are not without their disadvantages. The most notable disadvantage of HP gas MRI is that it is requires a polariser and multi-nuclear scanner, neither of which are readily available. Furthermore the costs of ^{3}He are greatly increasing due to a global shortage which has resulted in a shift towards using ^{129}Xe instead. Initially, the majority of studies used ^{3}He as it is easier to polarise to a higher level resulting in in higher image quality. The precession frequency of ^{3}He is also closer to ^{1}H than ^{129}Xe which makes it easier to produce multi-nuclear equipment (coils and pulse sequences). However, ^{129}Xe has the advantage over ^{3}He of enabling dissolved phased imaging (as well as being more readily available) [68].

Spin Exchange Optical Pumping

The technique of polarising the electron spin states of gaseous alkali metals (such as Rb) using optical pumping has been around since the 1950's [69]. It was later discovered that spin exchange allowed ^{3}He, ^{129}Xe and other noble gases to be polarised by spin exchange with the polarised gaseous Rb [70, 71, 62]. The process of polarising ^{129}Xe with SEOP using Rb is as follows.

A beam of circularly polarised light (with either a positive or negative helicity) enters an optical cell containing the Rb and ^{129}Xe. The cell is kept at a high enough temperature for the Rb to be a vapour for the duration of the polarisation buildup. The laser light excites Rb electrons from the ground state of $5^2S_{\frac{1}{2}}$ to the excited state of $5^2P_{\frac{1}{2}}$. The optical cell is kept in the presence of a static magnetic field that causes splitting of the electron sublevels according to the value of their magnetic quantum number (m_j). In this case $m_j = \pm\frac{1}{2}$. As the laser is circularly polarised only electrons in one sublevel will be excited depending of the helicity of the light. For example if the laser light has a positive helicity then the $m_j = -\frac{1}{2}$ ground state sublevel will be excited.

The excited electrons then proceed to decay back down to the ground state with an equal distribution between energy sublevels. As the laser is still on, any excited electron that decays into the $m_j = -\frac{1}{2}$ ground state sublevel will be excited again almost immediately, whereas any electron decaying into the $m_j = +\frac{1}{2}$ ground state sublevel will temporarily remain there. As a result there is a buildup of electrons in the $m_j = +\frac{1}{2}$ ground state sublevel. This process happens very quickly with almost 100% Rb polarisation occurring within the order of 10^{-5} seconds. The build-up of polarisation in Rb electrons pumped by laser light with a positive helicity is shown in Figure 3.8.

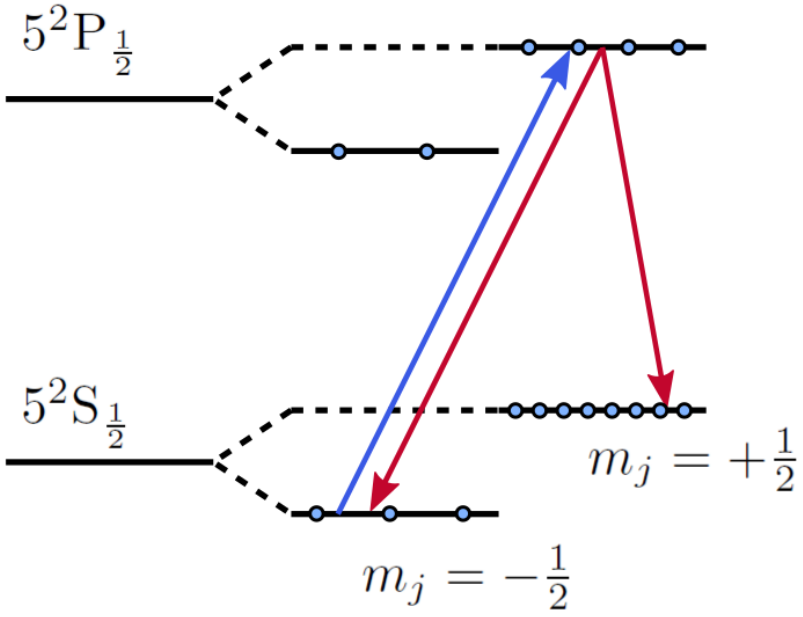


Figure 3.8: Process of polarisation of Rb electrons by optical pumping. Circularly polarised laser light excites electrons from the $5^2S_{\frac{1}{2}}$, $m_j = -\frac{1}{2}$ ground state sublevel (blue) to the $5^2P_{\frac{1}{2}}$ excited state. Electrons decay back into both sublevels with an equal distribution (red) resulting in an increased number of lectrons in the $m_j = +\frac{1}{2}$ ground state sublevel.

Collisions between the ^{129}Xe and Rb result in spin exchange. This is where a spin-up Rb electron will transfer its spin to a spin-down ^{129}Xe nucleus due to hyperfine interactions. This causes the Rb electron to become spin-down and the spin-down ^{129}Xe nucleus to become spin-up. The Rb electron will then go on to be excited again by the laser light and so there will always be spin-up Rb electrons causing an buildup in the polarisation of the ^{129}Xe nuclei. Nitrogen and helium are often used as buffer gases in SEOP. Nitrogen has the function of facilitating the collisional mixing of the Rb sublevels and preventing a loss of polarisiation in the Rb due to a relaxation of the excited states through optical

emission. The He is used to improve the thermal conductivity of the gas mixture within the cell as He is 25 times more thermally conductive than Xe [72].

Once the ^{129}Xe has been polarised to the desired level, it is cooled to condense out the Rb vapour (which is toxic) and then pumped out of the cell for use in experiments. Once the ^{129}Xe leaves the static magnetic field there will be no splitting of energy sublevels and the polarisation will decay rapidly over a time period of minutes. It is therefore important to keep the HP ^{129}Xe in a large magnetic field as much as possible to maximise the available signal.

Metastable Exchange Optical Pumping

MEOP is a technique of polarising ^{3}He nuclei by using an excited metastable state of ^{3}He instead of an alkali metal intermediary. In order to excite a portion of the ^{3}He electrons from their ground state to the 2^3S_1 energy level, a weak r.f. discharge is applied across the optical cell. This is done at low pressure to preserve the long lasting metastable state of ^{3}He. This process can only be used to polarise ^{3}He as ^{129}Xe does not have a suitable metastable state.

Circularly polarised laser light is then applied causing further excitation of electrons from the 2^3S_1 energy level into the 2^3P_0. Once again the circularly polarised light will only excite electrons in a specific sublevel based on the spin state of the electron. These electrons will then decay back down into the two metastable sublevels. As the laser light is still present there will be a buildup in the polarisation of the electrons in the metastable state ^{3}He in the same manner as the Rb in SEOP. There is strong coupling between the nucleus and electrons of ^{3}He resulting in spin exchange between the polarised electrons in the metastable state and the ^{3}He nuclei in the ground state. This occurs during collisions between the ^{3}He in a process which depolarises the polarised metastable ^{3}He allowing it to be repolarised in order to propagate the polarising

process. This results in a buildup of polarisation in the ^{3}He nuclei.

MEOP has a very high photon efficiency with one ^{3}He nucleus polarised for each photon absorbed in the optical pumping process. This is significantly more efficient than SEOP and as a result the polarising time of MEOP is in the order of tens of seconds rather than the tens of minutes required for SEOP. This high speed overcomes the disadvantage that the polarised ^{3}He needs to be compressed from the low pressure (~1 mB) required to maintain the metastable state, to atmospheric pressure to allow a sufficiently large sample for imaging.

3.3 ^{3}He MRI Study

3.3.1 Method

Healthy volunteers were recruited from the Leicester area before being scanned in Nottingham and Sheffield. The inclusion criteria for volunteers were: aged 20 years old or under; no diagnosis of respiratory disease; never smoked. Exclusion criteria were: inability to undergo MRI (due to surgical implants, pacemakers, claustrophobia etc.); inability to provide written consent; inability to travel.

One of the useful features of HP ^{3}He is that its gaseous nature results in fast diffusion throughout the lung. This diffusion can be investigated by calculating a value for the Apparent Diffusion Coefficient (ADC) to provide information about lung morphology. The ADC can be measured at various different time-scales in order to investigate different effects. For example long time-scales, of the order of seconds, correspond to diffusion across several acinar airways whilst short time-scale measurements investigate diffusion inside a single alveolus or acinus [73]. ADC has been found to be a useful measure of lung pathology, particularly for monitoring emphysema where several studies have found a an elevation in the short time-scale ADC of ^{3}He in patients with emphysema [74, 75, 76, 77].

A short study was carried out to compare measurements of the ADC at two different time scales in healthy adolescents between two sites: the University of Nottingham and the University of Sheffield.

Volunteers were picked up from the Leicester area and taken to the University of Nottingham for their first scan before heading up to the University of Sheffield for their next scan before returning to Leicester. Patients were scanned at both sites in the same day.

In Nottingham all scans were performed using an Intermagnetics General Corporation 0.15T permanent magnet system with an MR Research Systems console. The HP gas administered was to the patient from a 1l Tedlar bag containing a gas mixture consisting of a small amount of HP ^{3}He (<10%) mixed with a buffer of ^{4}He. The ^{3}He within the gas mixture was hyperpolarised using a custom made MEOP polariser system whilst a custom made r.f. coil was used for signal acquisition for all ^{3}He scans [78]. ADC measurements in Nottingham were taken at 13ms.

Due to the rapid decay rate of the polarisation of HP ^{3}He, the HP gas had to be produced locally to the scanner. As a result the University of Sheffield produced and administered the gas used for their measurements. At the University of Sheffield the gas was polarised using a commercial SEOP polariser (GE Healthcare, Amersham, UK), and scans were performed using a GE Signa HDx 1.5T scanner (GE Healthcare, Milwaukee, Wisconsin, USA). ADC measurements in Sheffield were taken at 2ms.

3.3.2 Pulse Sequences

FSE-GD

Two pulse sequences were used to measure the global diffusion of HP ^{3}He in healthy adolescents. The first was a Fast Spin Echo (FSE) sequence based on the Carr-Purcell-Meiboom-Gill (CPMG) sequence which is a form of spin echo sequence (described in Section 3.2.2) that was originally proposed by Carr and Purcell in 1954 [79]. The sequence introduced the idea of an echo train in which a series of 180° r.f. pulses are performed on the with a regular period of 2τ between each 180° pulse with an initial spacing of τ after the initial 90° pulse. This produces echoes with a maximum signal intensity every 2τ after the initial 90° pulse. The time interval of 2τ is known as the echo time, T_E. One side effect of the Carr-Purcell train is that the echoes are inverted after each 180° pulse because the rephasing happens the same direction (e.g. along the $-y$ axis) each time [65].

In 1958, Meiboom and Gill made a modification to the Carr-Purcell echo train by alternating the phase of the 180° pulse by 90° with regard to the initial 90° pulse [80]. For example if the initial 90° pulse acts along the $+x$ axis then the 180° pulses will act along the $\pm y$ axis. This prevents the echoes from inverting as they are always formed in the same direction.

The CMPG sequence was modified for diffusion measurements with the addition of diffusion gradients which are gradient "lobes" which introduce a phase shift before and after the 180° pulse. The purpose of these lobes is to cause the nuclei to go out of phase with each other before rephasing them [81]. This is useful as only the nuclei which are in the same location for both lobes will have no net phase shift. As a result the signal intensity within a voxel will decay with successive r.f. pulses according to:

$$\frac{S}{S_0} = \exp\left(-bADC\right) \exp\left(\frac{T_E}{T_2}\right), \tag{3.7}$$

where S_0 is the unattenuated signal intensity, ADC is the Apparent Diffusion Constant and b is known as the "b-value", a variable which represents the degree of diffusion weighting given to a scan as a result of the diffusion gradients. The b-value is determined by the strength and timing of the gradient lobes in the following way:

$$b = \gamma^2 G^2 \delta^2 \left(\Delta - \frac{\delta}{3}\right), \tag{3.8}$$

where γ is the gyromagnetic ratio, G is the strength of the gradient field, δ is the duration of a gradient lobe, and Δ is the time between lobes. ^{3}He in the lungs at 0.15T has a T_2 relaxation time of approximately 5 seconds [82]. It is therefore the case that signal loss due to diffusion dominates signal loss due to T_2 decay such that Equation 3.7 becomes:

$$\frac{S}{S_0} = e^{-bADC} \tag{3.9}$$

for the purposes of data analysis in this study. A diagrammatic representation of the adapted CPMG sequence used for calculating ADC in HP ^{3}He Scans is shown in Figure 3.9.

It can be seen from Figure 3.9 that the diffusion gradients are present during signal acquisition for each echo. This causes the acquired signal to be frequency encoded in one dimension which allows the ADC for each position to be calculated in the same way as the global ADC. The signal and ADC can therefore be plotted against position as shown in Figures 3.10 and 3.11 in which the two peaks are from the two lungs.

ADC values calculated a different positions were then placed into a histogram in order to calculate the mean ADC. This has the advantage over the global ADC

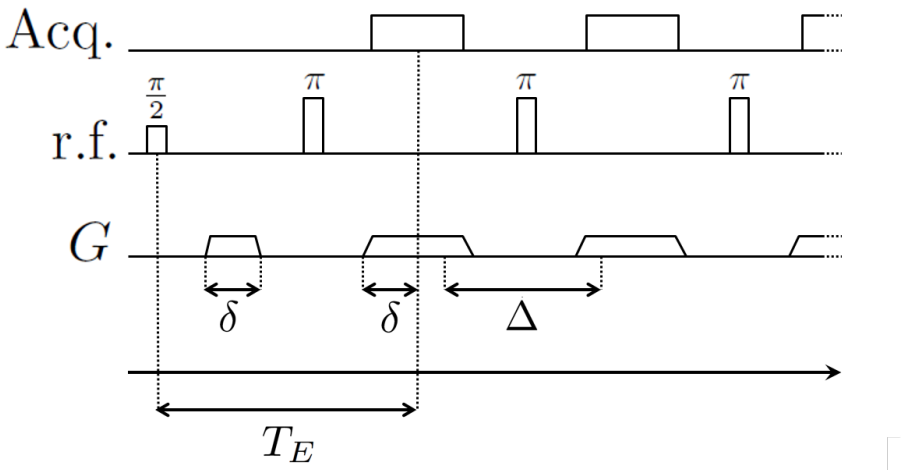


Figure 3.9: The fast spin echo sequence based off the CPMG sequence used for calculating global ADC in HP ^{3}He Scans.

that ADC values that are not from the lungs can be removed. It has previously been observed that, at short time scales, ADC has a strong positive correlation with lung inflation [83] and so a correction for volume must be applied to the measured ADC values. This was done using the following equation developed by Ball [84]:

$$ADC = ADC_v + 0.36 ADC_v \left(\frac{V_B}{V_{FRC}} \right) \tag{3.10}$$

where ADC_v is the non-corrected ADC, V_B is the volume of the gas mixture inhaled by the patient, and V_{FRC} is the Functional Residual Capacity (during this study the gas mixture was inhaled at FRC).

The same parameters were used for all ^{3}He scans performed using the FSE-GD sequence described in this thesis: 64 echoes and sampling points with a 30μs sample period, a T_E of 14ms, a T_R of 4000ms, a δ of 1ms, a Δ of 13ms, and a gradient strength of 2.23x10^{-5} Tcm^{-1} which gave a b-value of 0.29scm^2.

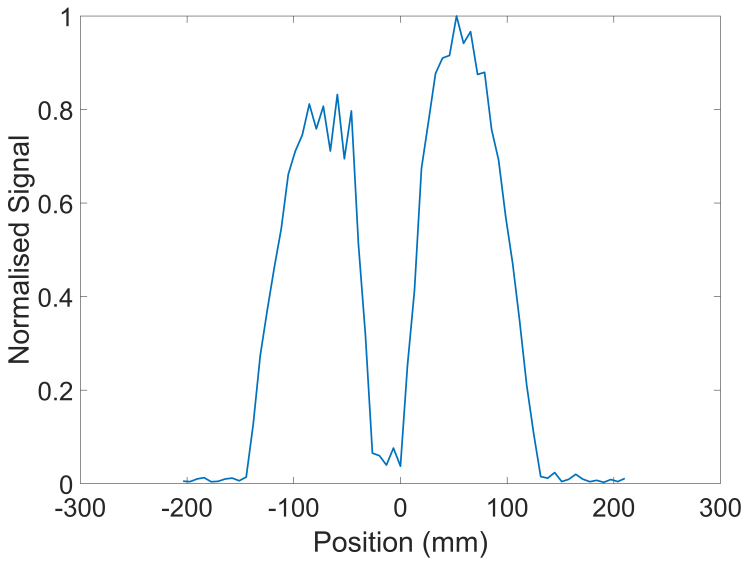


Figure 3.10: Normalised signal against position for set of adolescent lungs scanned using the Global Diffusion pulse sequence

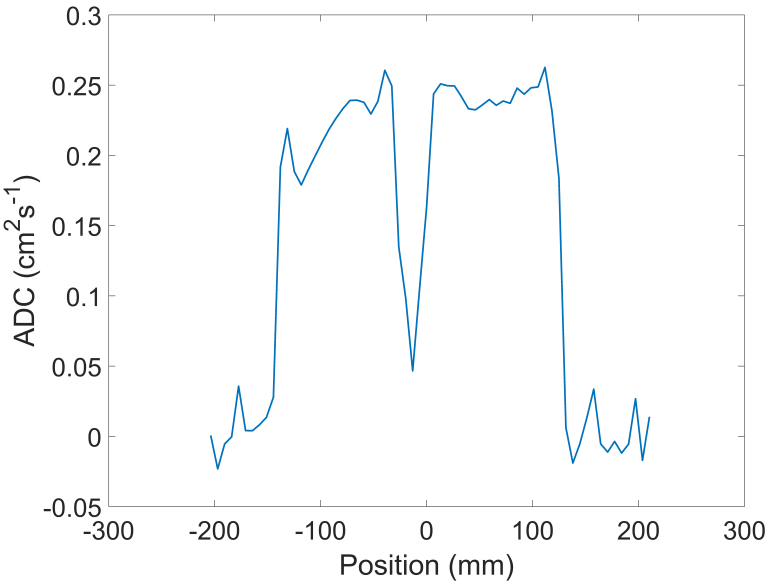


Figure 3.11: ADC against position for set of adolescent lungs scanned using the Global Diffusion pulse sequence

STE

The FSE-GD sequence based on the CPMG sequence was used for calculating ADC at 13ms after inhalation whilst a different sequence was used for calculating ADC after seconds had passed. The sequence used for this was called the Stimulated Echo (STE) sequence which is similar to the global STE sequence used by Wang et al. [85]. The STE sequence consisted of three sections: the calibration stage, the set up stage, and the read out stage. Firstly, in the calibration stage, there are five consecutive flip angle pulses (with a low flip angle) immediately followed by FID acquisitions with a crusher gradient at the end of each repeat to remove any residual net transverse magnetic moment between each pulse. During this stage the signal intensity is attenuated in the following manner:

$$S_{(n)} = S_0 \sin(\alpha) \left(\cos(\alpha) \exp\left(\frac{-T_R}{T_1} \right) \right)^{n-1}, \tag{3.11}$$

where S_0 is the initial signal intensity with no attenuation, α is the flip angle and n is the number of excitations. For the purposes of this study a typical T_R of 150 ms was used. Given the T_1 has an approximate value of 25 seconds we can approximate the signal attenuation to:

$$S_{(n)} = S_0 \sin(\alpha) \cos^{n-1}(\alpha). \tag{3.12}$$

The calibration stage is followed by the set up stage which consists of two 90° r.f. pulses along with a single diffusion gradient lobe between the two r.f. pulses. The set up stage is not repeated. After the set up stage is the read out stage in which a further small r.f. pulse (with the same flip angle as the r.f. pulses in the calibration stage) followed by an acquisition of the formed echo in the presence of a diffusion gradient lobe. The read out stage is repeated a further 44 times with a crusher gradient present before each repeat. The signal intensity of the

echo formed during the read out stage is attenuated in the following way:

$$S_{(n)} = \frac{1}{2} S_0 \sin(\alpha) \left(\cos(\alpha) \exp\left(\frac{-T_R}{T_1} \right) \right)^{N_C+n-1} \exp\left(-b_{(n)} ADC_{(n)} \right), \quad (3.13)$$

where n is the read out stage repetition number, S_0 is the original signal intensity with no attenuation, N_C is the number of repetitions in the calibration stage, ADC_n is the Apparent Diffusion Constant for the n^{th} repetition of the read out stage and $b_{(n)}$ is the b-value. As $T_R << T_1$ this simplifies to

$$S_{(n)} = \frac{1}{2} S_0 \sin(\alpha) \cos^{N_C+n-1}(\alpha) e^{-b_{(n)} ADC_{(n)}}, \quad (3.14)$$

in which $b_{(n)}$ is given by:

$$b_{(n)} = \gamma^2 G^2 \delta^2 \left[\left(\Delta_{(n)} - \frac{\delta}{3} \right) + \tau \left(\delta^2 - 2\Delta_{(n)}\delta + \Delta_{(n)}\tau - \frac{7}{6}\delta\tau + \frac{8}{15}\tau^2 \right) \right], \quad (3.15)$$

where γ is the gyromagnetic ratio, G is the strength of the gradient field, τ is the ramp time of the diffusion gradients, δ is the duration of the diffusion gradient lobe in the set up stage, and $\Delta_{(n)}$ is the time between the diffusion gradient lobe in the set up stage and the diffusion gradient in the n^{th} read out repetition. Overall a diagram of the three sections of the STE pulse sequence is shown in Figure 3.12.

When using the STE pulse sequence, as the number of repetitions and flip angle are known, and $b_{(n)}$ can be calculated, it is possible to calculate the value of ADC by comparing the decay in the calibration stage with the decay in the read out stage. This removes the element of attenuation that is not caused by diffusion allowing the ADC at each readout acquisition to be calculated using:

$$ADC_{(n)} = \frac{-\ln(S_{(n)})}{b_{(n)}}. \quad (3.16)$$

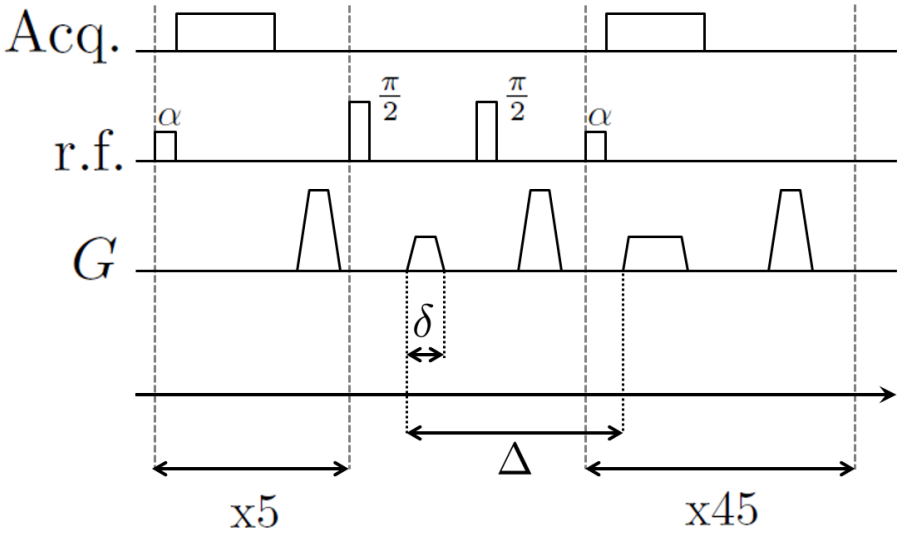


Figure 3.12: Diagram of the STE sequence

A set of typical values for ADC against time for an adolescent set of lungs evaluated using the STE pulse sequence over a time scale of several seconds is shown in Figure 3.13.

For all scans performed in the ^{3}He study used a flip angle, α, of 5°, 1024 sample points with a 20 μs sample period, a δ of 2.2ms, and a gradient strength of 3.708x10^{-6} Tcm^{-1}. The calibration stage lasted 150ms per repetition with 12ms between the two $\frac{\pi}{2}$ pulses in the set up stage and 18ms between the last $\frac{\pi}{2}$ pulse and the start of the read out section. Each repetition of the read out stage also lasted 150ms.

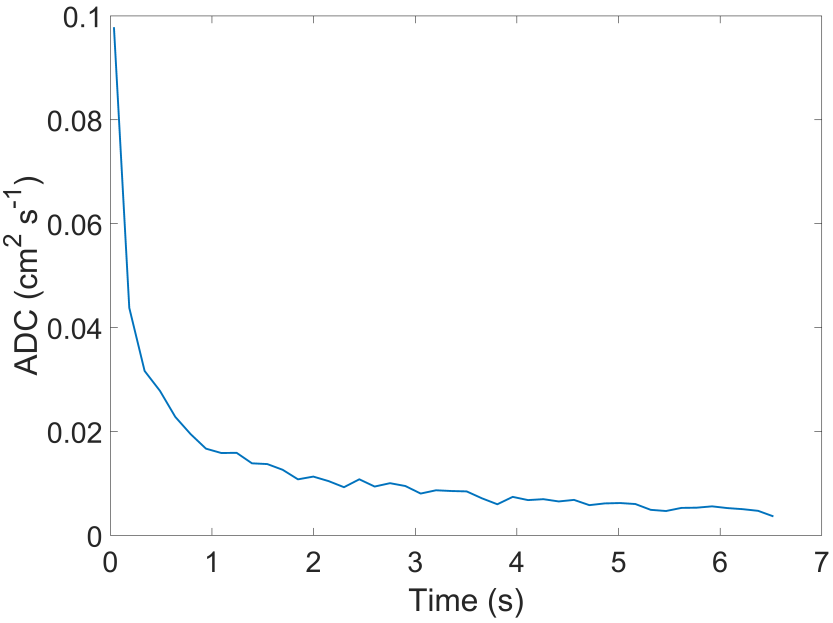


Figure 3.13: Typical plot of ADC against time for adolescent lungs

3.3.3 Results

A short study using HP ^{3}He was carried out to compare measured ADC results from the University of Nottingham and the University of Sheffield at two different time scales (13ms and 2ms respectively). At the University of Nottingham ADC was measured at 13ms for 7 healthy volunteers, ranging in age from 12 to 20, using a Global Diffusion FSE sequence, and at several points between 1 and 6 seconds using the STE sequence (both sequences are described in Section 3.3.2). Figure 3.14 shows ADC measured at 13ms against age for the healthy volunteers scanned in this study as well as volunteers measured during a previous study at the University of Nottingham using the same pulse sequence, scan parameters and MRI scanner.

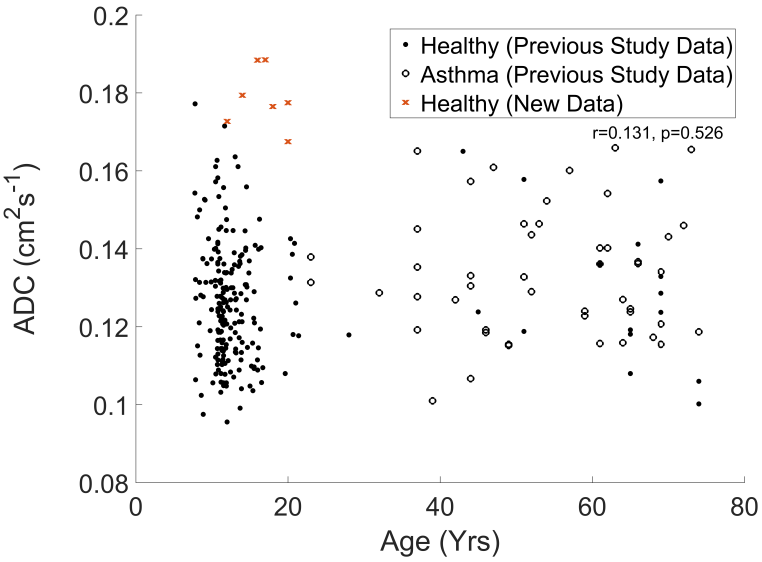


Figure 3.14: ADC at 13 ms against age for healthy volunteers and asthma patients measured at the University of Nottingham from previous studies [86, 87] as well as new healthy volunteer data.

There is no obvious correlation between age and ADC shown in Figure 3.14 for either the new data or the data from a previous study, healthy or asthmatic ($p=0.526$). This is unexpected as there have been studies in the past which have suggested that there is a link between age and ADC among healthy children and adults [88, 89] even over the age range of 5 to 20 years. The ADC measurements in the new study were found to be significantly higher than the ADC measurements from the old study ($p<0.001$). Although the reason for this difference is unknown, the values of the new data are more in line with measurements from other studies [89].

Figure 3.15 shows a bland-Altman plot of the short time-scale ADC data for Nottingham and Sheffield. This demonstrates that there is no significant correlation between these two measurements ($p=0.707$), however there are not

enough data points to draw any significant conclusions. More data points are needed. Furthermore the difference in time-scale between the short time-scale measurements of the two sites that will have an affect on the anatomical region assessed at the two sites [76, 90, 91, 92]. At the University of Nottingham the time-scale of 13 ms was long enough for the diffusion measured to be occur through an acinus, whereas the shorter time-scale of the University of Sheffield, 2 ms, was short enough for diffusion to be limited to a single alveolus rather than an entire acinus. No comparison could be drawn between long time-scale ADC data for Nottingham and Sheffield as no long time-scale measurements were taken at the University of Sheffield. It is possible that there might be more of a similarity in measurements of ADC at a longer time-scale.

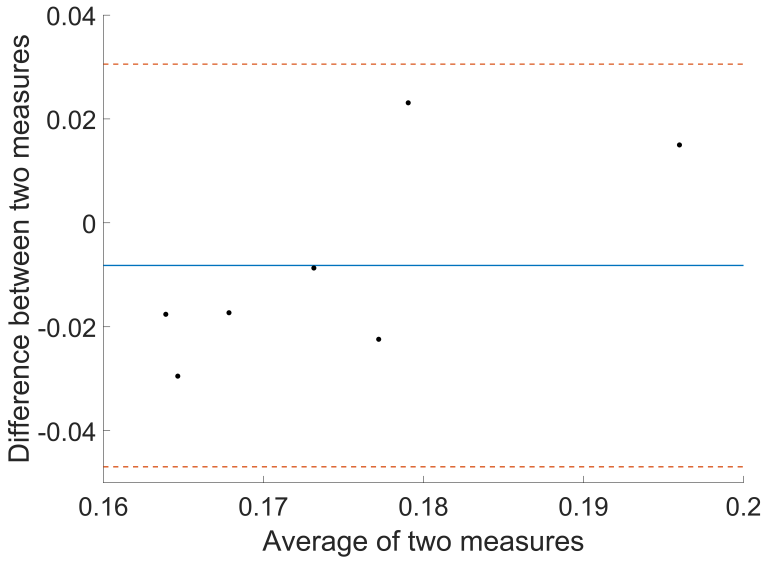


Figure 3.15: Bland-Altman plot of the ADC at 13ms measured at the University of Nottingham and at 2ms at the University of Sheffield with mean and 1.96 SD highlighted.

3.4 ^{129}Xe Study Method

3.4.1 Collaborators

The ^{129}Xe study was a collaborative study with contributions from the following people:

- Prof Ian Hall - Designed Study. Principle investigator.
- Dr. Shahideh Safavi - Screened and recruited volunteers. Performed clinical monitoring of patients during scan visits.
- Sarah Wolfe - Screened and recruited volunteers. Performed clinical monitoring of patients during scan visits.
- Dr Michael J Barlow - Qualified Manufacturer (QM). Produced HP ^{129}Xe gas.
- Dr Brett Haywood - Qualified Assurer (QA) for HP ^{129}Xe polarised gas. Assisted with scan acquisition and administration of gas. Assisted in r.f. coil safety tests.
- Dr Arthur Hill - Qualified Person (QP). Responsible for certifying each batch of HP ^{129}Xe gas.
- Steven Hardy - Created broad-banded sequences. Carried out safety tests of RAPID coil. Performed MRI scans and data analysis.
- James Thorpe - Performed MRI Scans and data analysis. Developed a standard protocol beginning with a coronal sliced projection. Carried out safety tests of CMRS coil.
- Christoph Arthofer - Developed image processing software including automated SNR measurement algorithm.

MHRA approval was granted for the polariser system (EudraCT: '2013-004336-30', CTA: '03057/0061/001-0001') and ethical approval was granted for the pilot study by the NRES Committee (East Midlands, Nottingham 2 Ethics Committee, NRES Ref: '13/EM/0401'). Only healthy volunteers were recruited for the pilot study.

3.4.2 Equipment

Xe Polariser and Scanner

A GE 2000 Xe-Rb continuous flow polariser was used to hyperpolarise all the ^{129}Xe used for imaging in this thesis. This could be used to produce gas to fill either 0.6 L or 1 L Tedlar bags. The gas mixture used in polarisation contained natural abundance (NA) Xe, of which 26.4% is ^{129}Xe. As well as NA Xe the gas mixture also contained N_2 and ^{4}He in a ratio of 2% NA Xe / 10% N_2 / 80-87% ^{4}He. The gas mixture exiting the optical cell (the site of SEOP) passed through a liquid nitrogen cold finger to condense out the Xe from the other gases. The cold finger was then heated to thaw out the Xe for collection. As the polariser was continuous flow rather than stopped-flow the volume of gas produced was based on the time spent polarising rather than being a fixed volume. As a result the exact volume of gas produced each run was unknown. The polarisation of each bag produced was measured immediately after production with an average of 8.72%.

A GE 1.5T Signa HDx MRI scanner was used for all HP ^{129}Xe scan visits discussed in this report. The body coil of this scanner was used for 3-plane localisation as well as ^{1}H co-registration imaging. A separate r.f. coil was used to produce the ^{129}Xe images.

^{129}Xe r.f. Coils

Two ^{129}Xe r.f. coils were used in this study. Initially an eight channel RAPID Biomedical RF coil was used for imaging before a newer Clinical MR Solutions (CMRS) coil was acquired. The RAPID coil is shown in Figures 3.16 and 3.17. This is an elliptical coil of hard plastic designed such that when placed on the patient bed the coil is a close fit to the bore of the magnet. The coil consists of a transmit coil, located within the the outer plastic shell, and a separate, two part, eight channel receive coil of which the top receive array visible in Figure 3.17 while the bottom receive array is attached to the outer shell (and therefore concealed by the pillow phantom in Figure 3.17). In these Figures a pillow is being used as a place-holder for a human thorax. Due to the shape of the coil the patient can be in one of two positions within the coil, either the patient must have their arms tightly to their sides inside the coil or else the patient must extend their arms above their head. Whilst the latter places great strain on the patients shoulders which causes discomfort over even a short time period, the former constrains the study to patients with a small enough chest to fit both thorax and arms within the coil. In both cases the tightness of the coil caused patient to feel more "trapped" than usual for an MRI scanner which caused a high rejection rate among patients with claustrophobia.

In contrast, the CMRS r.f. coil has a much more patient friendly design shown in Figures 3.18 and 3.19. This coil is designed to be worn by the patient in a similar manner to a life jacket with cut-out sections (visible in Figure 3.18) to allow the arms and shoulders freedom to move outside the coil. As with the RAPID coil, the CMRS coil contains a transmit coil in the outer part of the jacket, as well as separate top and bottom receive arrays visible in both Figures 3.18 and 3.19. There are several advantages to the CMRS coil design over that of the RAPID coil. Firstly, the CMRS coil is significantly lighter than the RAPID coil to allow it to be worn as a jacket increasing patient comfort.



Figure 3.16: RAPID Biomedical 8-channel lung r.f. coil with pillow phantom



Figure 3.17: RAPID Biomedical 8-channel lung r.f. coil viewed from inferior end with a pillow phantom. The top receive array can be seen resting on top of the phantom

Another significant advantage of the CMRS coil is that it fits closer to the body of the patient (shown through the pillow phantom) giving an increased filling factor that increases image quality. This closer fit is due to the flexible nature of the coil with its adjustable straps rather than the fixed, hard plastic of the RAPID coil. This allows for larger patients to be scanned who would not fit inside the RAPID coil. A further advantage of the CMRS coil is that it allows feet first scanning to occur. This combined with the lighter weight, freedom of arms and absence of an enclosed feeling makes the CMRS significantly more patient friendly which helps to reduce patient rejection from the study.

The CMRS coil had a significantly greater patient comfort however a comparison of image quality of the two r.f. coils needs to be carried out in full to ensure that the CMRS coil is a suitable replacement for the RAPID coil in terms of performance.

Both coils were safety tested and had underwent Flip Angle calibration tests. The CMRS coil was safety tested using a sample of animal tissue that was placed in the coil inside the scanner with temperature probes monitoring the temperature within and on the surface of the sample. The pulse sequence used for the Xe study (bbfgre) was then run for a prolong period of time (40 mins) with parameters set to maximise the r.f. output of the coil. No significant temperature change was seen in the sample over the duration of the scan. A comparison was drawn with the scanner body coil by repeating the test using pulse sequence with the highest SAR levels on the system for a further 40 mins. Once again tehre was no significant temperature change in the sample.

As the CMRS coil was bespoke it had to be Flip Angle calibrated to determine the relationship between the gain of the amplifier and the resultant Flip Angle of the r.f. pulses for a specific sequence (bbfgre). This was done by scanning



Figure 3.18: Clinical MR Solutions 8-channel lung r.f. coil with pillow phantom



Figure 3.19: Clinical MR Solutions 8-channel lung r.f. coil viewed from inferior end with a pillow phantom

a bag of HP ^{129}Xe with no gradients present such that the entire sample was interrogated with each r.f. pulse. The signal intensity decays according to:

$$S = S_0 \cos(\alpha)^{n-1}, \tag{3.17}$$

where S_0 is the initial signal, n is the excitation pulse index and α is the flip angle. A non-linear least squares best fit algorithm was used to calculate α from the measured signal decay at various levels of transmit gain.

3.4.3 Pulse Sequences

Fast Gradient Echo

In HP ^{129}Xe MRI there is no T_1 relaxation back to a highly polarised state after each r.f. pulse for any imaging sequence. As a result it was undesirable to use any sequence that required a large number of r.f. pulses. For this reason a gradient echo sequence was chosen for all ^{129}Xe scans. The duration of the scan was also a critical factor to be considered in choosing a sequence as the patient was required to hold their breath for the duration of the scan. For this reason a fast gradient echo sequence (FGRE) was chosen. A single acquisition of this sequence is shown in Figure 3.20. This is a standard FGRE sequence produced by GE that was broad-banded in order to be usable as a ^{129}Xe sequence. This broad-banded sequence is called *bbfgre*. The most common image taken was a simple ventilation image looking at the distribution of inhaled gas within the lung. This can be used to identify any obstructions within the lung that result in blank regions in the image where there is no gas. Other images that can be taken using HP gas MRI include diffusion imaging and dissolved phase imaging.

An FGRE sequence was also used for two ^{1}H sequences: the 3-Plane localiser, used to ensure the lungs where in the centre of the magnet, and the co-registration imaging sequence, used to compare ^{129}Xe images with anatom-

ical features seen using ^{1}H MRI. These sequences were modified to reduce the SAR by increasing T_R and reducing the flip angle. This was done to prevent any damage occurring to the ^{129}Xe coil which, by necessity, was around the volunteer at all times during the scanning process.

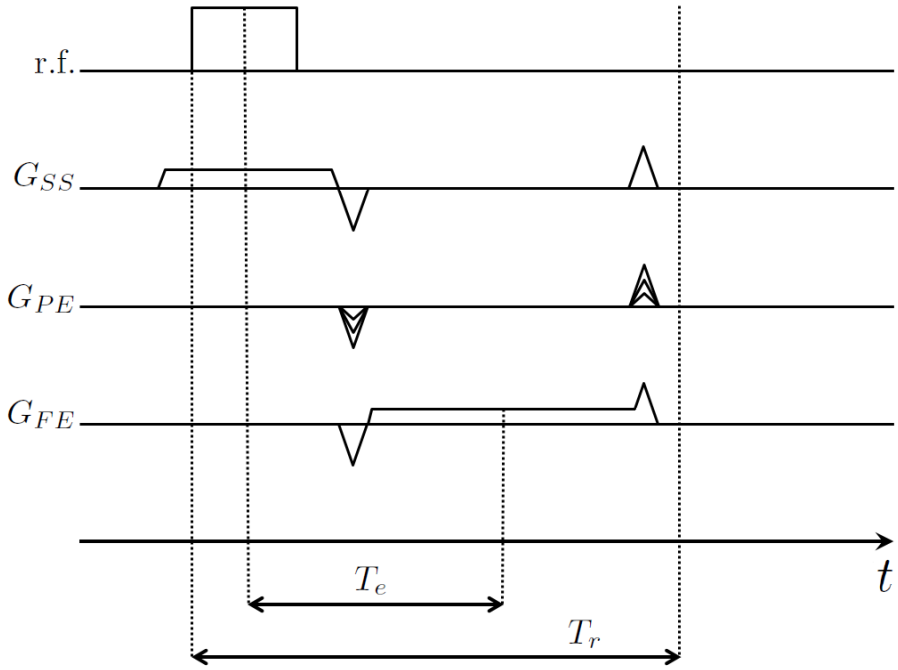


Figure 3.20: The fast gradient echo sequence used for the 3-Plane localiser, ^{1}H co-registration and (after broad-banding) the ^{129}Xe scan.

3.4.4 Scan Visit Protocol

The main aim of HP ^{129}Xe study was to develop a standard method of imaging the lungs. A standard protocol was to be established using healthy volunteers before applying this protocol to patients with lung disease. Various techniques where trialled to investigate their reliability in lung imaging. The only standard to be fully maintained as a standard was to begin each scan session with a

coronal projection. This imaged the entirety of the inhaled gas simultaneously which allows for intra- and inter-patient comparisons to be drawn. Development is still ongoing to determine the optimal slice thickness and imaging plane to obtain an image with high spatial resolution without compromising signal strength.

Each volunteer could visit up to four times, with a maximum of four scans per visit. At the start of each visit the volunteer would first have some standard observations taken (oxygen saturation, blood pressure etc.) before any scanning could take place. Then, on the first visit only, the volunteer inhaled 1L of unpolarised ^{129}Xe in order to verify that the patient had no adverse reaction to breathing in the gas; as well as to familiarise the volunteer with the inhalation process and the effect of Xe. The volunteer was then observed for half an hour, with measurements taken at 0, 5, 10, 15 and 30 minutes after exhalation, to ensure that no adverse effects were felt and that oxygen saturation remained high. After this initial set of observations had been made the patient could have their first scan (on the subsequent three visits this initial test was not required).

The polarisation process of the ^{129}Xe began before the volunteer arrived at the MRI suite. This was done as it took up to an hour to produce the first bag with subsequent runs taking shorter times. Once the bag was ready it was stored within the high magnetic field of the bore of the MRI scanner. This was necessary for a hyperpolarised sample as, although there is no T_1 recovery of the net magnetic moment, there is T_1 decay from the hyperpolarised state back to equilibrium. In Earth's magnetic field, HP ^{129}Xe has a T_1 time of a matter of minutes whilst at 1.5T this time is greatly extended.

Prior to each scan, measurements were taken of the volunteers oxygen saturation and blood pressure after which the volunteer could be placed into the r.f. coil used for the scan (either RAPID or CMRS) and loaded into the scanner.

Whilst in the bore of the magnet the patient wore a pulse oximeter in order to allow continued observation for the duration of the scan. This was to ensure that the patient could receive immediate medical attention if they became hypoxic.

All scans used a gradient echo sequence for reasons discussed earlier and began with a 3-Plane localiser (looking at ^{1}H rather than ^{129}Xe) to ensure the patient was correctly positioned within the scanner. Once it was confirmed that the volunteer was correctly positioned, the ^{129}Xe scan could take place. The volunteer orally inhaled the HP ^{129}Xe from a Tedlar bag through a tube and held their breath (if required). Due to the limited space available in the bore of the MRI scanner, a member of the research team was required to guide the tube of the Tedlar bag into the volunteers mouth. This person could then be used to confirm that the volunteer had successfully inhaled all the ^{129}Xe before scanning, as well as monitoring the well-being of the volunteer.

It was decided that the first scan of each volunteer visit would be taken in the coronal plane with no y gradient present, thus giving an image with an infinite slice thickness. This was done so that the entirety of the inhaled gas was interrogated simultaneously. This ensured that both the scanner and polariser were functioning correctly as well as allowing for comparisons to be made between each patient visit and between different patients. During this first scan, the volunteer was asked to take a further partial "flushing breath" of air immediately after they inhaled the ^{129}Xe in order to prevent any inhaled ^{129}Xe remaining in the volunteers' upper airway and mouth. A series of tests was done to determine whether an image taken with this flushing breath gave more information than an image taken with no flushing breath.

Immediately after scanning, the patient was taken to an observation bed for a further thirty minutes of observations (including oxygen saturation, blood

pressure etc.). As with the previous observations, measurements were taken at 0, 5, 10, 15 and 30 minutes after the patient was moved to the observation bed. As soon as the first polarised bag of ^{129}Xe was placed in the scanner, the process of polarising a second bag of ^{129}Xe began. As this process took approximately an hour, the polariser was run in parallel with both the scanning and the subsequent observations. Once the next bag was prepared and stored in the bore of the MRI scanner, a further set of observations (oxygen saturation, heart rate, and blood pressure) were taken of the volunteer before they re-entered the scanner.

The exact details of the subsequent ^{129}Xe scans (of which there could be up to three) varied depending on the experiment, but each scan in which the slice select gradient was active was preceded by a ^{1}H co-registration scan. This was done to ensure that the slicing was positioned correctly and covered the entirety of the lung, as well as to provide anatomical information to compare to the acquired Xe image. This required the volunteer to inhale 1L of air and hold their breath for the duration of the scan (approximately 12 seconds).

After the final scan was completed a further thirty minutes of observation were required before the volunteer could be released. The volunteer received a follow up phone call 24 hours later to ensure no there were no longer term adverse effects to the ^{129}Xe. It was required that each volunteer had at least a one week period between each visit in order to ensure there were no long term effects from a build-up of Xe.

Unfortunately there have been many technical issues with this project primarily revolving around the polariser. The polariser has been out of action for two years which has hindered the project and resulted in no clinical scans being achieved.

3.5 Image Processing

3.5.1 Image Reconstruction

The MRI scanner used in the Xe study could be programmed to save the spatial frequency domain (better known as k-space) data for each scan. This raw data could then be converted into frequency space by Fourier transformation. This formed an image as precession frequency is directly related to spatial location due to the gradient coils. The formed image could be improved with further processing such as adding a filter (e.g. median, gaussian, etc.) to smooth the image, or by gradient unwarping. The GE 1.5T scanner had built in software to convert from k-space into image space which was extractable as a Digital Imaging and Communications in Medicine (DICOM) file format. Alternatively the raw data file (called a "P-file") could be saved and extracted to allow the image to be reconstructed without the unknown processing performed by the GE software. Both file types were extracted for data analysis.

One of the main corrections to an image during reconstruction is gradient unwarping. This is the removal of distortions to the image caused by inhomogeneities in the magnetic field caused by the gradient coils. At lower field strengths this is less of a problem however at 1.5T there can be noticeable curvature of straight lines caused by this effect. As the gradient coils are not changed between scans the inhomogeneities remain relatively constant which allows a map to be created of the distortions by imaging a phantom. This map can then be used to correct the image. The process of gradient unwarping is done automatically by the GE reconstruction software however there are situations in which this process is unwanted as gradient unwarping can affect the uniformity of noise distribution across the image.

An example of gradient unwarping in a HP ^{129}Xe ventilation projection is shown in Figure 3.21 where (a) shows the warped image and (b) the unwarped image. The distortion in the noise caused by the unwarping process can be seen in (b) with a higher intensity present in the corners of the image with a more rarefied middle-top and middle-bottom. In contrast the noise in (a) is relatively uniformly distributed.

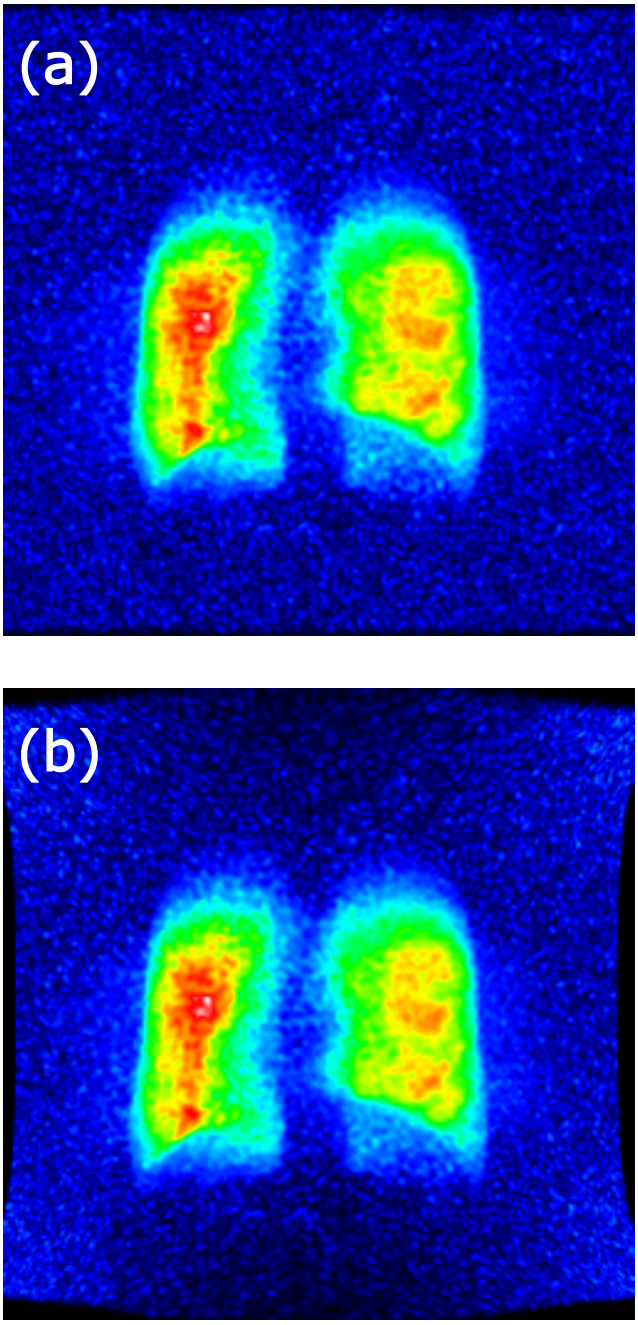


Figure 3.21: HP ^{129}Xe ventilation projection before and after gradient unwarping where (a) shows the warped image and (b) the gradient unwarped image.

3.5.2 Signal-to-Noise Ratio Analysis

Motivation for SNR Analysis

The effectiveness of an image as a diagnostic tool is related to the quality of the image. It is therefore essential (in both clinical and experimental settings) to quantify image quality to ensure that there is good consistency and reproducibility between scans. This allows a comparison to be drawn between MRI systems, r.f. coils and pulse sequences or as an inclusion/exclusion criterion for images taken in clinical trials or other experiments. The image quality of a HP ^{129}Xe or ^{3}He scan is affected by many factors, some of which are related to the patient (e.g. anatomy and breathing patterns) and some are systematic (e.g. gas polarisation and gain).

The main method of assessing image quality in MRI is signal-to-noise ratio (SNR) which can be calculated by either comparing multiple acquisitions or by selecting regions of interest (ROIs) [93, 94]. Taking multiple repeat acquisitions is a popular technique as it allows a difference image to be formed from two repeated (identical) acquisitions. However this is not possible with HP gas imaging as there is no polarisation recovery and so each r.f. pulse (as well as field inhomogeneities and the presence of oxygen) will cause the gas to depolarise making it impossible to acquire two identical images in succession [95]. An alternative method of calculating SNR from a series of sequential acquisitions is to model signal decay over a shorter time-scale. However, in the case of sliced MR imaging, each slice is selected independently due to the slice select gradient and so only specific slices of the lung are excited at any given time. The nature of the HP gas imaging allows the diffusion of any formerly exited (and therefore depolarised) gas from an interrogated slice into regions where excitation has not yet occurred, and vice versa. This leads to regional signal variations as some gas is excited on numerous occasions, even after it has lost

its hyperpolarisation, whilst other gas remains hyperpolarised by never being interrogated. This issue can be resolved by removing the slice select gradient and exciting the entire sample at once resulting in a projection image. However, although the removal of gradients allows SNR (and other parameters such as flip angle) to be measured, it does not provide the necessary level of detail for clinical diagnosis. Therefore the preferred method of calculating the SNR of a sliced HP gas image is to select one ROI containing signal and one containing noise, and compare the two ROIs where the SNR can be calculated as

$$SNR = \frac{S_{mean}}{N_{std}} = \frac{\bar{S}(r)}{\sqrt{\frac{2}{4-\pi}}\sigma(r)}, \tag{3.18}$$

where $r \in ROI$; $\bar{S}(r)$ is the mean of S in the signal ROI; $\sigma(r)$ is the standard deviation of S in the noise ROI, and $\sqrt{\frac{2}{4-\pi}}$ is a correction factor [93].

The selection on ROIs can either be done manually or automatically. Traditionally selection has been done manually however this is time-consuming and suffers from inter- and intra-operator variability. This issue is particularly prevalent in ^{129}Xe imaging where the SNR can be low and there can be partial volume effects, as opposed to ^{1}H imaging where there is usually high contrast between different tissues allowing regions to be more clearly defined. The noise ROI can be selected from signal acquired from regions in which there is no xenon. This includes air surrounding the body as well as regions containing tissue with no ^{129}Xe (e.g. the liver). This requires background noise to be uniformly distributed across the image which might not be true if gradient unwarping has occurred. It is therefore wise to perform SNR measurements on the warped images as this gives a truer representation of the distribution of the signal (despite warping anatomical features). Partial volume effects arise when there are regions which, due to the finite thickness of the slicing, contain both ^{129}Xe and tissue in unknown quantities.

Automatic ROI Selection

It is preferable to select ROIs automatically to avoid operator error/bias. There is currently no consistent ROI selection in HP gas MRI in operation, nor are there any available clinical protocols in the literature. The automated procedure for region selection used in the HP gas MRI study described in this thesis was done in the following way. Firstly, an image was reconstructed from the raw data to avoid any unknown processing being implemented. This was done by transforming each channel using Fast Fourier Transform before constructing a composite image using a sum-of-squares algorithm. A non-local means (NLM) filter was then applied to the image to increase the contrast between the signal region and the noise region. The NLM approach takes the entire image into consideration when removing noise, rather than just the local area around each voxel [96]. This opperates on the idea that the relationship between a voxel and its neighbours will have a similar appearance to patches of the same size at other positions within the image [97].

In the case of ^{1}H imaging there is a large difference between the minimum signal from tissue and the maximum signal from noise, which makes thresholding a trivial task. However, the signal peak for HP ^{129}Xe scans is not clearly defined and so it is difficult to define a threshold for signal. This issue was solved by producing a histogram from the NLM-filtered image that was used to characterise the features of the noise region. This could then be used to segment the noise area, leaving the signal region as the residual. A region growing algorithm was used with a random voxel selected as the initial seed position in the NLM-filtered image. The initial seed voxel was checked to ensure it lay within the upper and lower thresholds of noise provided by the histogram evaluation. This check was recursively applied to each voxel in the neighbourhood to segment the entire noise region (and consequently the signal region as the residual). For low signal images, any holes which occurred were morphologically

closed. A buffer zone was then added, from which no samples were extracted for SNR calculations. This was done to reduce the number of mis-classified voxels. Figure 3.22 shows the automated ROI selection process with the original image shown in (a), and the residual signal ROI (the orange region) and buffer zone (the white region) are shown in (b).

A random sample of points was then selected from the signal region, and the same number of random points was selected from the noise region. These two samples were then used to calculate the SNR using equation 3.18. The SNR value was then normalised by the polarisation of the gas used in acquiring the image.

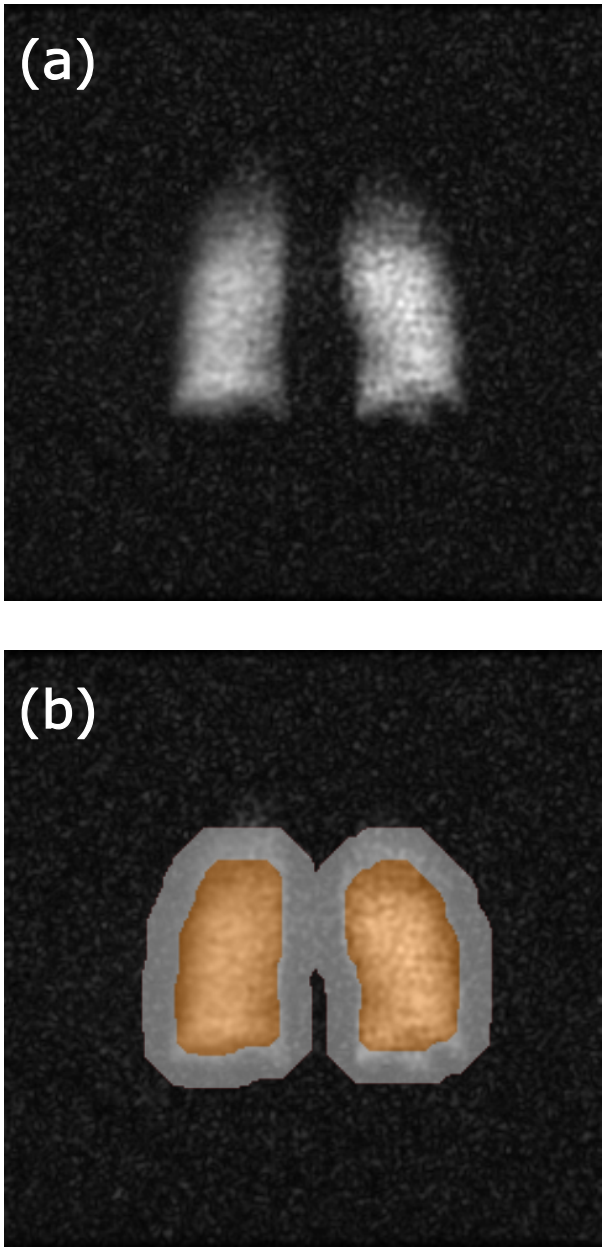


Figure 3.22: Automated ROI selection process where (a) shows the original image and (b) shows the selected signal ROI with a surrounding buffer zone. FOV = 48cm, Res = 128x128, T_E = 5.0ms, T_R = 7.6ms, flip angle = 20°.

3.5.3 Super Resolution

There is often a difference in the spatial resolution in the different planes of an MRI scan. This is due to the differences in gradients used to create a 3-D image. In certain situations a scan can be set up such that each voxel in an image is equidimensional. However this takes time and so requires the object being scanned to remain stationary. This is possible for anatomy such as the brain which can be kept still for extended periods of time. However, imaging the thorax must be done in a short period of time as the heartbeat and motion of breathing cause a significant amount of movement. It is often necessary for the patient to hold their breath for the duration of a scan during HP gas imaging which requires the scan time to be as short as possible. This issue is made worse by the fact that HP gas MRI scans are for patients with lung disease who already have breathing difficulties. There is also a limited amount of signal available in a HP gas scan due to the finite volume of gas breathed and the lack of polarisation recovery. It is therefore the case that large voxels are used to increase signal intensity. This is done by having a relatively large slice thickness in comparison to the in-plane resolution.

Super resolution is a technique for increasing spatial resolution by comparing multiple low resolution images taken from multiple viewpoints rather than improving the resolution of a single scan. This idea was first proposed as a technique for MRI in 2002 by Greenspan, Kiryati and Peled as a way of increasing spatial resolution in the slice select gradient in cases where 3-D imaging was not an option [98]. Several research groups implemented different forms of super resolution to MRI over the subsequent years with a review of these techniques produced by Van Reeth et al. in 2012 [99], who covered both in-plane and through-plane super resolution. There are two main forms of through-plane resolution: parallel stack acquisition and multi orientation scans.

Parallel stack acquisition where a series of low resolution scans are taken in the same plane but with a spatial offset that is smaller that through-plane resolution of each scan. These scans will all contain subtly different information which can be combined into a higher resolution image by averaging over the set of scans. This has been implemented in phantom studies and brain imaging [100, 101, 102, 103] but never before in HP gas MRI. As it's name suggests, multiple orientation scans work by comparing low resolution scans, with a significant difference in in-plane and through-plane resolution, of the same object taken in different orientations. Again, this has been implemented in brain imaging [104].

A simulation was run to test the efficacy of parallel stack acquisition in increasing the spatial resolution images on the scales required for HP ^{129}Xe imaging. This was done using a 3-D brain image (provided by Christoph Arthofer) with equidimensional voxels. The original slices were then averaged into slices of 9 times the thickness of the original slicing to produce a low resolution image. This was done three times with a spatial offset of one third of the new slice thickness, increasing by one third for each low resolution image, to produce three low resolution images with overlapping information. These low resolution images where then averaged to produce a high resolution reconstruction of the original image. As the three low resolution images had a slice thickness of nine times the thickness of the original image, the high resolution reconstruction had a significantly lower resolution than the original image. This process is shown in Figure 3.23 where (a) is the original image, (b), (c) and (d) are the overlapping low resolution images, and (e) is the high resolution reconstruction. There is a significant increase in resolution between the low resolution and high resolution images with details visible in (e) that are not present in (b), (c) and (d).

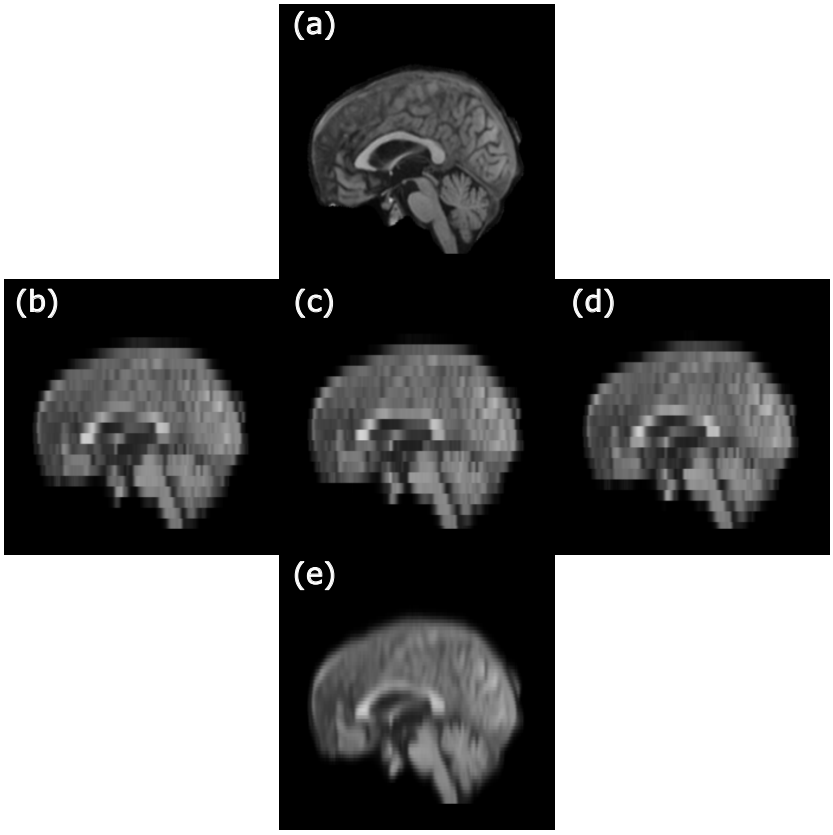


Figure 3.23: Super resolution simulation using a high resolution brain image where (a) is the original image, (b), (c) and (d) show the simulated low resolution images and (e) shows the averaged image.

The super resolution technique has previously not been used in HP gas MRI. One of the key difficulties for this is that the separate low resolution scans must be taken after the patient has been removed from the scanner for examination, and then returned to the scanner. A shift in the patient position, such as a rotation or some other movement, is expected which would cause the low resolution images to be misaligned. This issue can be resolved by taking a high resolution ^{1}H image before each low resolution HP ^{129}Xe image. These high resolution ^{1}H images can then be compared to evaluate the shift in the patients position by applying a transformation to the images. The same transformation can then be applied to the low resolution HP ^{129}Xe images to align them. The transformation can also be applied to an ^{1}H co-registration images taken with the same resolution as the HP ^{129}Xe images.

3.6 ^{129}Xe MRI Development Results

3.6.1 Polarisation

In order for HP ^{129}Xe MRI to be used in a clinical setting the validity and repeatability of various imaging techniques had to be developed. The majority of the test carried out had the aim of developing ventilation imaging however there was also a test to determine the capability of the available set up for perfusion imaging. All of the tests described in this thesis were performed using healthy adult volunteers. The polarisation of every bag of HP ^{129}Xe was measured before each scan. This is shown in Figure 3.24. Overall polariser operated relatively consistently with a mean polarisation was 8.71% with a standard deviation of 1.27%.

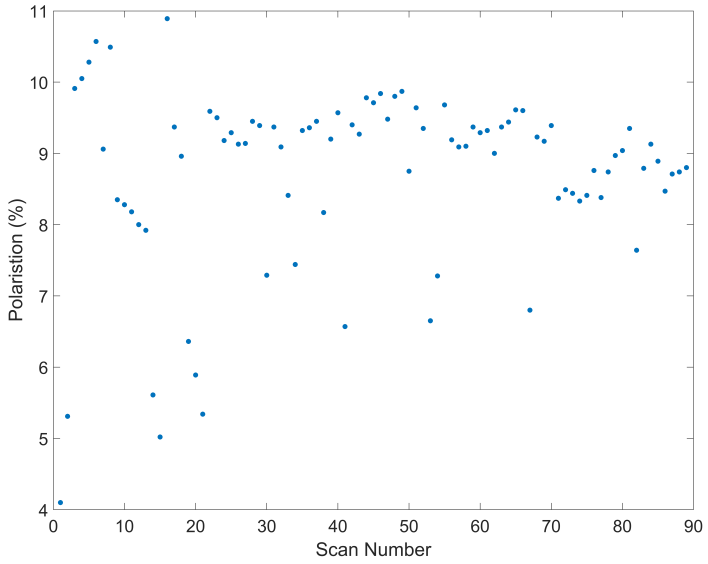


Figure 3.24: Polarisation of the bag of Xe used in each scan.

3.6.2 Dynamic Imaging

One of the earliest techniques to be tested at this site was dynamic imaging. This is where the patient undergoes multiple scans whilst inhaling and exhaling the HP ^{129}Xe in order to see where the gas flows to in the lung during breathing. The volunteer was scanned according to protocol described in Section 3.4.4. The bbfgre sequence was used with a FOV of 48 cm, a resolution of 128x128, a T_E of 5ms, a T_R of 7.5ms and a Flip Angle of 20°. Scans were taken at one second intervals. One of the advantages of dynamic imaging is that no breath hold is required which eases patient comfort. Figure 3.25 shows a dynamic series of images of inhalation and exhalation for a healthy adult male. The large airways are clearly visible with the branching of the main right bronchus visible in (c). However although the upper airways are visible the same is not true for the smaller airways. One explanation for this is that HP ^{129}Xe within the lungs for each sequential scan was depolarised to the extent that it provided limited

signal for subsequent scans. As a result we are only able to see the gas that is inhaled in one second by the volunteer as only new gas is polarised for each scan. It was therefore decided that subsequent scans would be taken during a breath hold in order to allow the lungs to be fully ventilated.

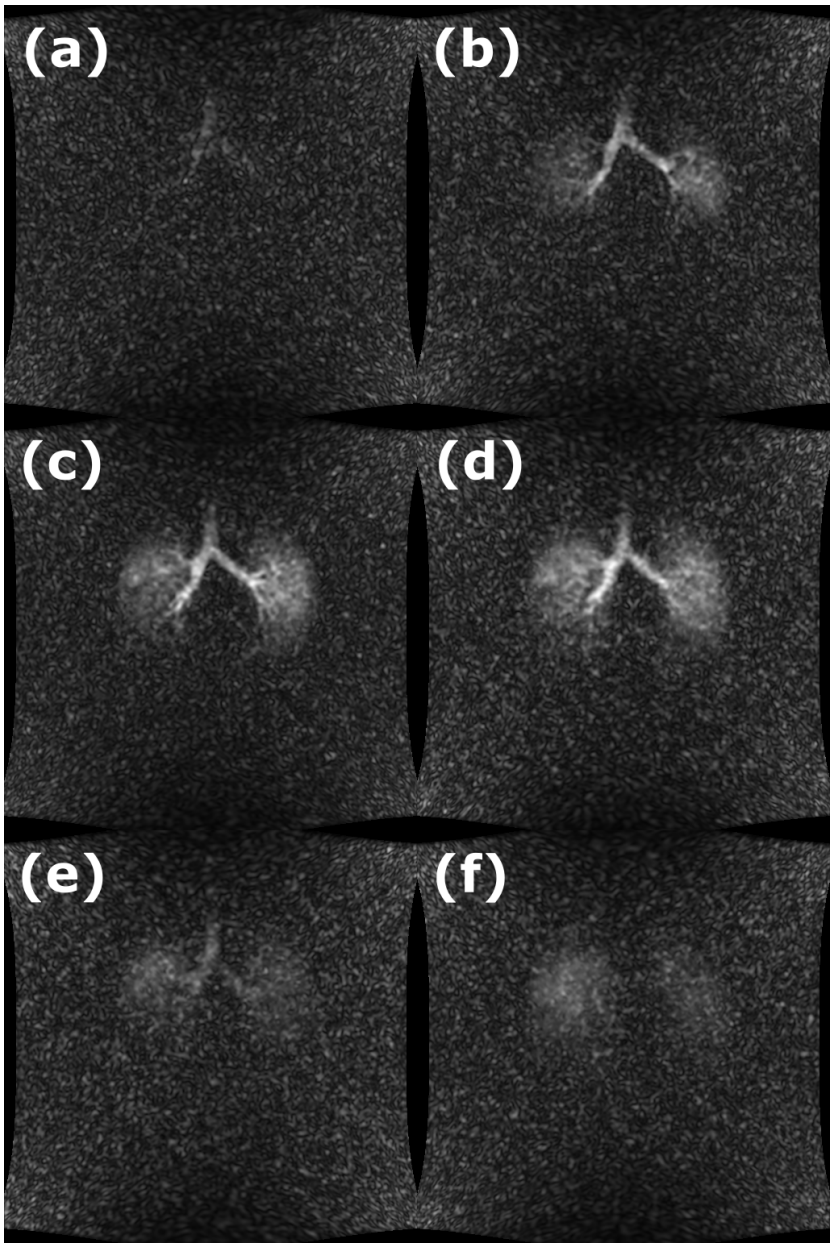


Figure 3.25: Sequential dynamic HP ^{129}Xe images of healthy adult male. FOV = 48cm, Res = 128x128, T_E = 5.0ms, T_R = 7.5ms, flip angle = 20°.

3.6.3 Coronal Projections

Once a scan protocol had been fully established and a few different scan types (such as dynamic imaging) had been tested it was decided that the first scan for each volunteer would be a projection of the lungs in the coronal plane. This was done by deactivating the y gradient to give an infinitely thick slice. This was done with a flushing breath to ensure that the entirety of the inhaled ^{129}Xe was located within the lungs instead of being trapped in the mouth and pharynx. This allowed for direct comparison between different patients and visit days to ensure that all equipment was functioning correctly. All coronal projections were acquired using the bbfgre sequence with the same settings: a 48cm FOV, a 128x128 resolution, a 5ms T_E, a 7.6ms T_R and a 20° Flip Angle. Figure 3.26 shows two examples of coronal projections for three healthy volunteers. Aside from shadowing from the pericardium (which is visible in all of these images) there are no significant defects in the form of dark regions to be seen in these lungs which is to be expected as these are healthy volunteers. However there is a significant difference in image quality between patients and between images of the same patient. For example, in Figure 3.26, the images of patient 004 are relatively similar in contrast to the difference between the two images of patient 012.

The difference in image quality inter- and intra-patient was investigated by calculating the SNR for each image using the automated method described in Section 3.5.2. This is shown in Figure 3.27 where the SNR has been multiplied by a normalised value of polarisation. This highlights a significant heterogeneity between different volunteers and also different scans of the same volunteer. For example the SNR values for volunteers 15067-005 and 15070-020 are relatively consistent between visits whilst volunteers 15065-004 and 15068-012 have a much larger range of values. However, overall volunteer 15065-004 had an higher value for SNR than the other volunteers. The means and standard deviations for each

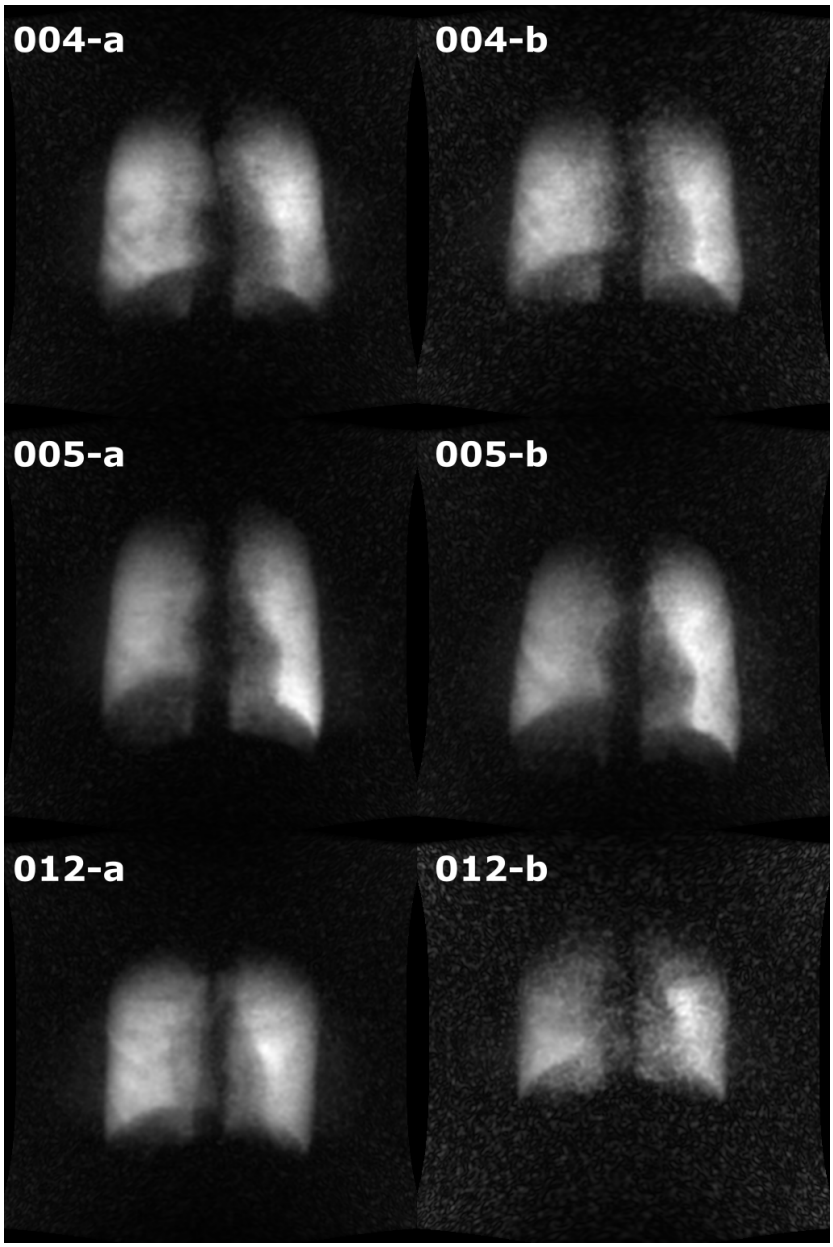


Figure 3.26: Two coronal projections of the lungs of three volunteers. FOV = 48cm, Res = 128x128, T_E = 5.0ms, T_R = 7.6ms, flip angle = 20°.

patient as well as inter-patient and for all data points is shown in Table 3.1. This demonstrates the variability in SNR measurement with some intra-patient measurements having a larger SD than the inter-patient SD or even the SD of all measurements, whilst other volunteer, such as volunteer 15067-005 having a significantly lower SD. From Table 3.1, it can also be seen that volunteer 15069-006 had a much higher mean SNR whilst volunteer 15080-021 had a significantly lower mean SNR.

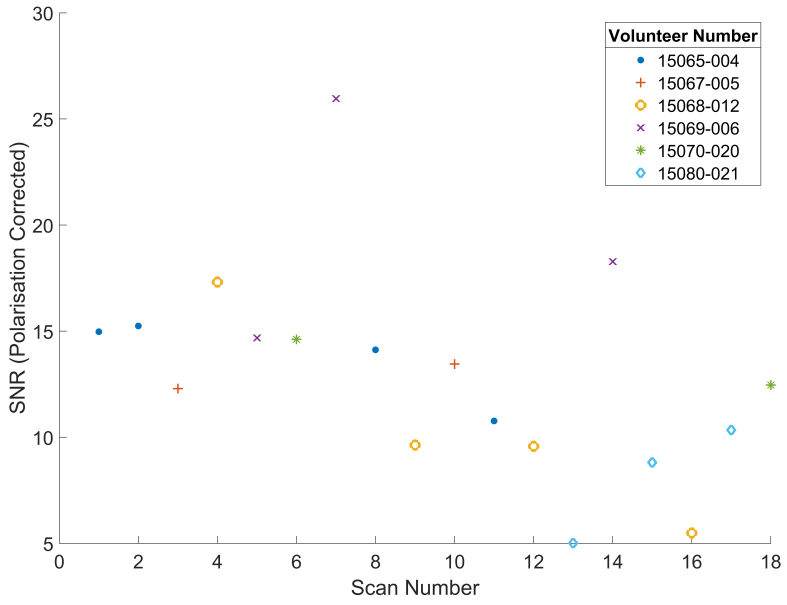


Figure 3.27: SNR (corrected for relative polarisation) of coronal projections for each volunteer.

The exact cause of this variation is unknown but it one possibility is that it is caused by variation in volunteer breathing patterns. One potentially significant variable is the amount of air inhaled during the flushing breath which is currently an unknown quantity. A larger amount of air will increase the dilution factor of the HP ^{129}Xe, as well as causing the gas to depolarise at a faster rate within

Patient	SNR (Mean/SD)
15065-004	13.78/2.06
15067-005	12.88/0.82
15068-012	10.51/4.93
15069-006	19.64/5.76
15070-020	13.54/1.53
15080-021	8.06/2.75
Inter-patient	13.07/3.89
All Data	12.95/4.87

Table 3.1: Mean/SD SNR (polarisation corrected) for each patient, inter-patient and all SNR measurements.

the lung, thus decreasing the SNR. A respiratory gating monitor was used for a few experiments to investigate this factor, however the monitor only measured the expansion of the chest rather than airflow and therefore was not precise enough to give meaningful information about the volunteer's breathing. This is because the volunteer was asked to breath in 1L of ^{129}Xe which does not fill the lungs to their maximum capacity. This was an issue because the process of inhalation is a combination of expanding the chest muscles and contracting the diaphragm with both aspects needed to fully inflate the lungs. Ordinarily a person will primarily use their diaphragm for inhalation, however in the supine position during experimental conditions this can vary with the patient using their chest muscles to a greater extent. This variation in breathing technique is exacerbated when the patient is not fully inflating their lungs. As the respiratory gating monitor was not able to detect the contraction of the diaphragm, it could not be accurately used to measure the volume of air inhaled by the volunteer during the scan.

A further suggestion relating to breathing technique was that it is possible some volunteers were subconsciously breathing air through their noses during the oral inhalation of the ^{129}Xe. This would also cause an increase in the dilution factor and decrease the polarisation of the gas. Furthermore there is the potential for a loss of ^{129}Xe if the patient exhaled through the nose prior to the flushing breath but after the inhalation of the HP ^{129}Xe. This theory was tested through the application of a nose clip during inhalation however no effect was observed other than a decrease in patient comfort.

On one occasion it was observed that the volunteer briefly orally exhaled immediately after inhaling the ^{129}Xe prior to taking a flushing breath of air. As this would reduce the volume of ^{129}Xe present in the lungs during the scan it would explain a decrease in the SNR. This was noticed by the member of the research team present in the magnet hall with the volunteer and so it is unknown whether or not this has occurred on during other experiments. In order to discourage volunteers from exhaling unnecessarily the breathing protocol was changed. Initially the volunteer was asked to fully exhale before inhaling the ^{129}. An additional forced exhalation and inhalation of air was included before the volunteer fully exhaled and inhaled the ^{129}Xe. Further experiments are required to verify the effectiveness of this change.

3.6.4 Slice Thickness

The signal provided by a HP sample is significantly larger than a sample at equilibrium. However, in the case of HP gas MRI the volume of the applied gas is limited as the patient is required to inhale the sample without becoming hypoxic. It was therefore the case that the volunteers in all studies described in this thesis inhaled volumes of HP gas of 1L or less. This low volume combined with the lack of polarisation recovery resulted in a low total available signal for each scan. It is therefore important to identify the limits, in terms of signal

intensity, of the slice thickness as a thicker slice will contain a larger amount of gas and therefore a larger amount of signal. Although it is desirable to have the largest possible signal it is also important to be able to identify structures or defects present in an image. The size of an object that can be identified from an image is related to the slice thickness with a thinner slice revealing more detail. Therefore a balance must be struck with the slice thickness between signal and detail.

Figure 3.28 shows two 25mm coronal slices of volunteer 15069-006 in which 1a and 1b show the ^{1}H co-registration images, 2a and 2b show the ^{129}Xe image and 3a and 3b show a combination of both imaging modalities with ^{129}Xe shown in blue. The colour change was performed using the photo manipulation software "GIMP". As the ^{129}Xe image was taken without a flushing breath, a residual volume of Xe can be seen in the trachea. In this instance the signal in the trachea is useful as it demonstrates the alignment between the two images with the dark region of the trachea in image 1b perfectly matching the bright region of the trachea in image 2b. Although there are no defects visible in these lungs (as the volunteer was healthy) image 3a highlights that the apex of the lungs are not being ventilated with ^{129}Xe. This was something that was observed in most of the healthy volunteers which suggests that there is nothing unusual about this. Overall the observable difference in ventilation between the two imaging modalities demonstrates that 25mm is a thin enough slice thickness to observe certain physiological features of the lung that would be missed without the use of HP ^{129}Xe (i.e. ^{1}H MRI or other imaging modalities such as x-ray CT).

Two 10mm coronal slices of volunteer 15069-006 are shown in Figure 3.29 where, as with Figure 3.28, 1a and 1b show the ^{1}H co-registration images, 2a and 2b show the ^{129}Xe image and 3a and 3b show a combination of both imaging modalities with ^{129}Xe shown in blue. Again these images were taken without a

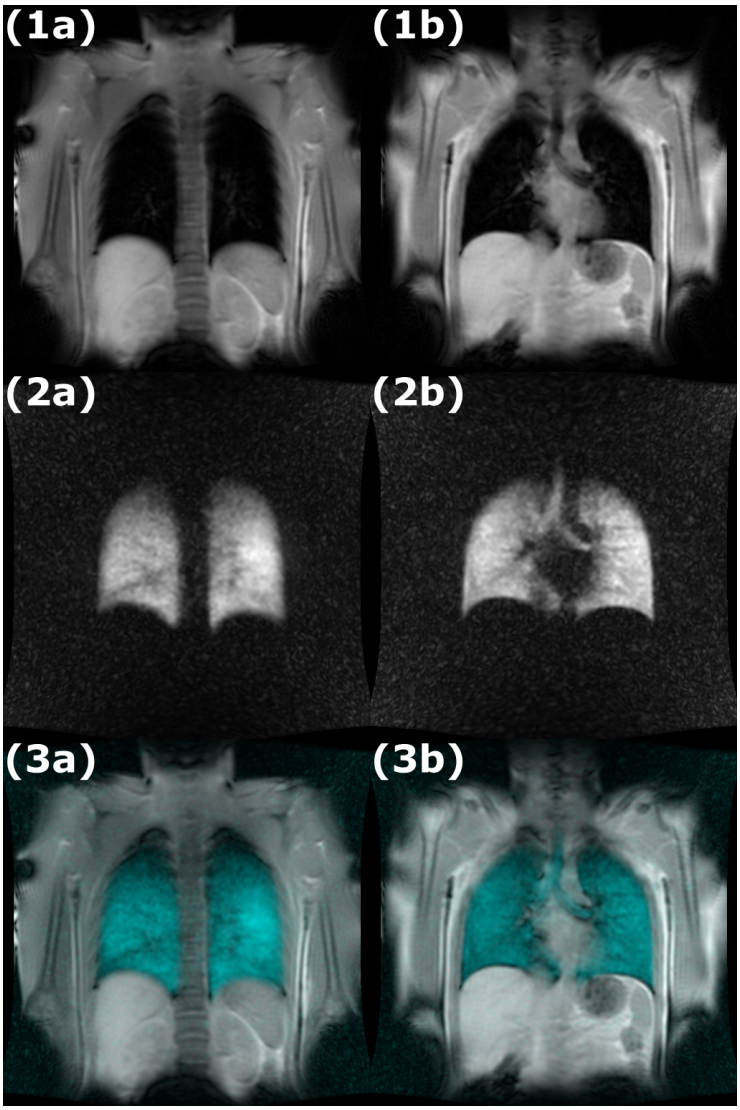


Figure 3.28: Two 25mm coronal slices of volunteer 15069-006 taken without a flushing breath in which 1a and 1b show the ^{1}H co-registration, 2a and 2b show the ^{129}Xe image and 3a and 3b show a combination of both imaging modalities with ^{129}Xe shown in blue. FOV = 48cm, Res = 128x128, T_E = 5.0ms, T_R = 7.6ms (^{1}H)/ 60ms (^{129}Xe), flip angle = 20°.

flushing breathing resulting in a visible trachea in the Xe image. The difference in SNR between the two slice thicknesses is significant however the level of detail in the 10mm slicing has also significantly increased. This is demonstrated by the dark regions near the sternum of both lungs in image 2a which have the appearance of being obstructions to the lung that were not visible in the 25mm slicing. However the proton co-registration image (1a) shows that there is vasculature in this region rather than lung which explains why this region appears dark on the xenon scan. Overall it would be preferable to continue to operate at the 10mm slice thickness however the SNR is still slightly two low resulting in a high rejection rate of images. One way this could be improved is by increasing the polarisation of the gas mixture.

The fgre and bbfgre sequences were used for the ^{1}H and ^{129}Xe scans respectively for the images in Figures 3.28 and 3.29. The settings for the 25mm proton scan were: FOV = 48cm, resolution = 128x128, T_E = 5 ms, T_R = 7.6ms and Flip Angle = 30° whilst the Xe scan had the same settings except for the T_R which was 60ms. For the 10mm slicing, the ^{1}H co-registration had the same settings except for a T_R of 70ms whilst the Xe scan had two changes from the 25mm Xe scan: the T_R was 8.4ms and the Flip Angle was 35°.



Figure 3.29: Two 10mm coronal slices of volunteer 15069-006 taken without a flushing breath in which 1a and 1b show the ^{1}H co-registration, 2a and 2b show the ^{129}Xe image and 3a and 3b show a combination of both imaging modalities with ^{129}Xe shown in blue. FOV = 48cm, Res = 128x128, T_E = 5.0ms, T_R = 70ms (^{1}H)/ 8.4ms (^{129}Xe), flip angle = 30° (^{1}H) /35° (^{129}Xe).

3.6.5 Transverse Plane Imaging

It is common procedure for CT scans of the lungs to be taken in the transverse plane rather than the coronal plane as this allows for the entirety of the extremities of the lungs to be viewed in a single slice. HP ^{129}Xe imaging was therefore performed in the transverse plane for comparison. However, the difference in the cross sectional area of the lung in the transverse plane compared to the coronal plane (the transverse being smaller) gave rise to a few issues.

Firstly the SNR of the transverse images was significantly lower per slice than the SNR of the coronal plane images. This was due to the reduction in volume of ^{129}Xe in a transverse slice. This was particularly noticeable at a slice thickness of 10mm where many of the images produced had extremely limited clinical value. The other large issue with transverse imaging related to the shape of the lung in that it took a larger number of slices to cover the entirety of the lung. This required the scan time to be increased which caused difficulties as it required the volunteer to hold their breath for a longer period of time and the polarisation of the gas decreases over time. Although this was not a significant issue for the healthy volunteers it is expected to be an issue for patients with lung diseases.

Initially all scans were performed with sequential slicing however, when this was done in the transverse plane, it was observed that the first slice had the highest SNR with the signal rapidly decaying over subsequent slices ultimately resulting in no visible image in the final few slices despite the presence of ^{129}Xe. This phenomenon was apparent irrespective of whether the lungs where sliced from superior to inferior or inferior to superior. One explanation for this effect is the diffusion of the ^{129}Xe through the lung. When the first slice is interrogated by the r.f. pulse the HP ^{129}Xe in that slice depolarises. This depolarised ^{129}Xe then diffuses into the next slice whilst some of the HP ^{129}Xe in the next slice

diffuses into the scanned slice. As a result the polarisation, and therefore signal, in each subsequent slice is reduced resulting in the signal decay. This is shown in Figure 3.30 which shows a 25mm transverse slicing from inferior to superior of volunteer 15080-021 without a flushing breath. This phenomenon was not observed in the coronal slicing which suggests that anatomy of the lungs allows gas to diffuse at a faster rate through the coronal plane than in the transverse plane. Figure 3.31 shows the same slice thickness of the same volunteer also without a flushing breath but in this case the slicing was interleaved rather than sequential. In slices 7 - 9 the trachea is clearly visible showing that there is information missing from the same slices done sequentially in Figure 3.30.

The scans shown in Figures 3.30 and 3.31 were both taken using the bbfgre sequence with an FOV of 48cm, a resolution of 128x128, a T_E of 5ms and a Flip angle of 35°. The sequential scan had a T_R of 7.6ms whilst the interleaved scan had a T_R of 80ms.

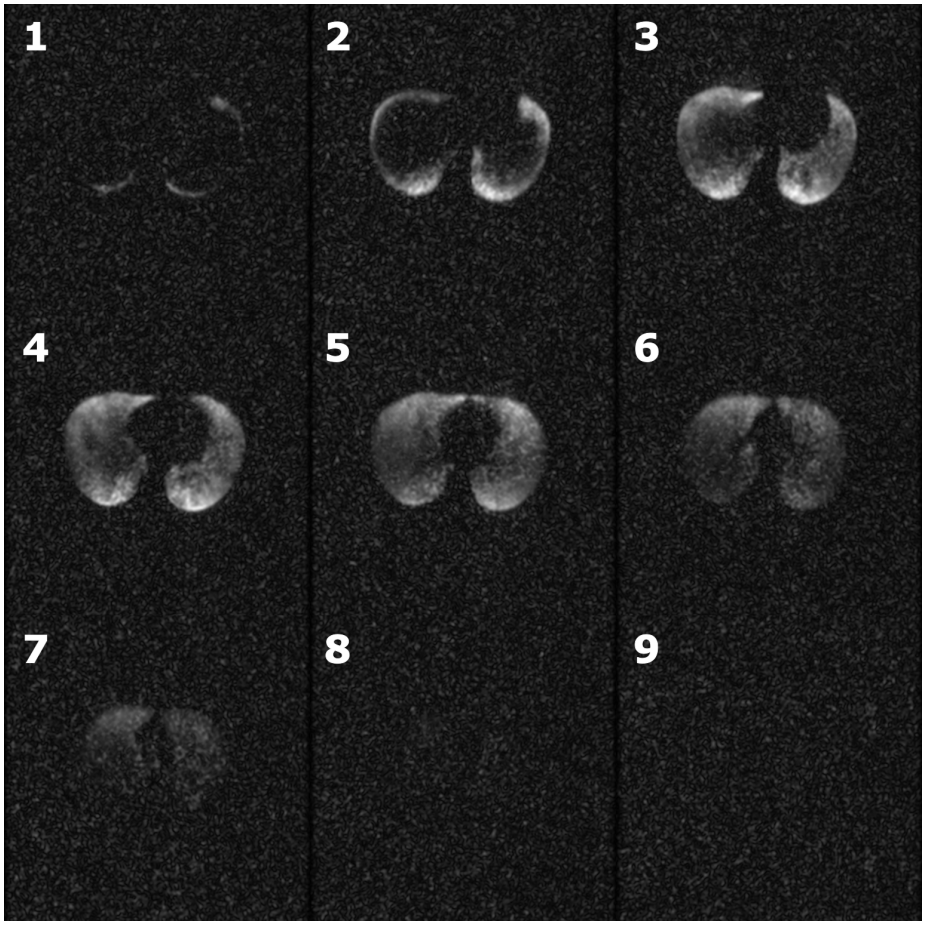


Figure 3.30: Sequentially acquired series of 25mm axial slices of volunteer 15080-021 without a flushing breath. Slices 1 to 9 go from inferior to superior. FOV = 48cm, Res = 128x128, T_E = 5.0ms, T_R = 7.6ms, flip angle = 35°.

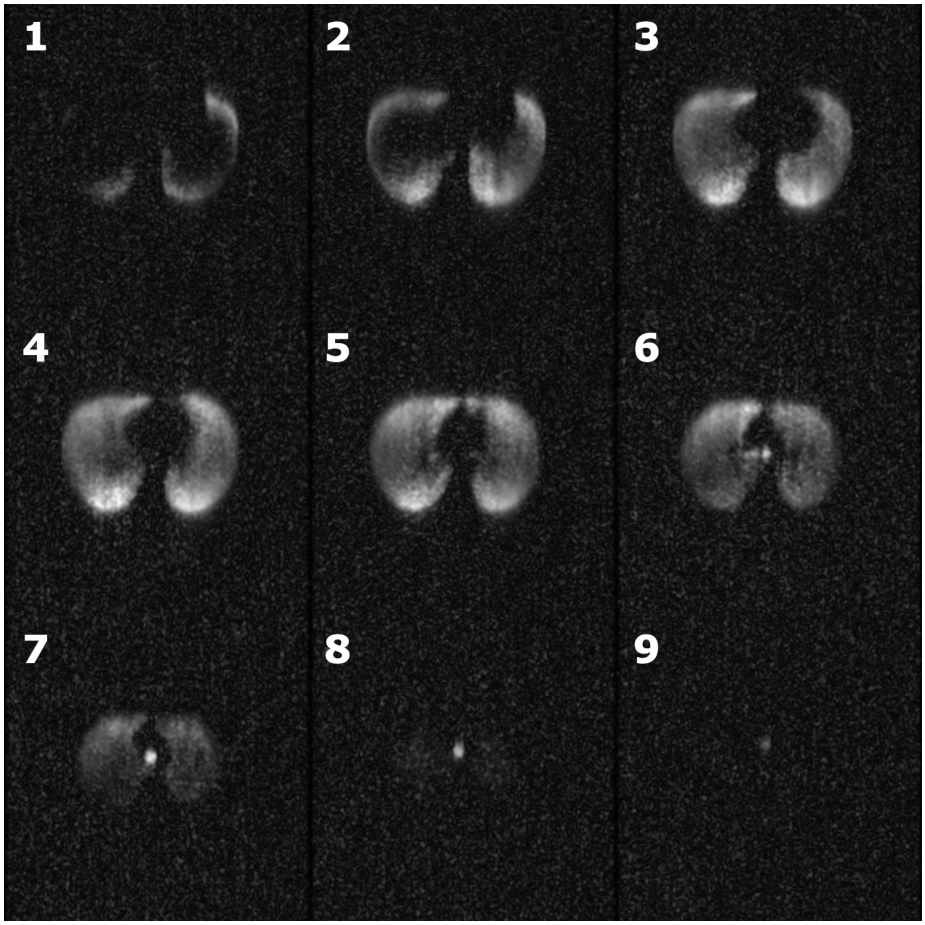


Figure 3.31: Interleaved series of 25mm axial slices of volunteer 15080-021 without a flushing breath. Slices 1 to 9 go from inferior to superior. FOV = 48cm, Res = 128x128, T_E = 5.0ms, T_R = 7.6ms, flip angle = 35°.

3.6.6 Flushing Breath

For the coronal projections a flushing breath was necessary to ensure that the entirety of the HP ^{129}Xe was in the lungs at the time of the scan to allow direct comparisons to be drawn between visits. However for more detailed anatomical slicing this was not essential. Experiments were therefore carried out to investigate the potential benefits of a flushing breath. Whilst the flushing breath has the advantage of filling the lungs to a greater capacity (which allows measurements of TLC to be taken with a greater accuracy), and increasing signal in potentially more clinically interesting areas (i.e. the extremities of the lungs), it has also, in previous sections, been suggested that the variability in the flushing breath could cause variation in SNR.

Figure 3.32 and Figure 3.33 show a series of 25mm coronal slices going from posterior (1) to anterior (5) of the same volunteer (15069-006). The same scan parameters were used for both scans with an FOV of 48cm, a resolution of 128x128, a T_E of 5ms, a T_R of 7.6ms and a Flip angle of 30°. Figure 3.32 was taken without a flushing breath whilst Figure 3.33 was taken with a flushing breath. The most noticeable difference between these sets of images is in slice 3, where the trachea and bronchi can clearly be seen on the series of images with no flush whereas this detail is lost on the images with a flushing breath. This demonstrates the effectiveness of the flushing breath in flushing all the ^{129}Xe into the lungs from the upper airways. Whilst the trachea and bronchi are interesting to observe and can be used to identify the location of a slice, the clinical significance of this information is minor. The presence of the trachea within an image has the advantage of verifying that the patient is correctly positioned with in the coil. This demonstrates that any absence of signal in the apices of the lungs is not an artefact caused by the patient's position within the coil but the true signal.

Another key difference between these images is the size of the lungs, which are noticeably larger in the flushing breath images. This most noticeable in slice 1 as well as slices 4 and 5 where the lungs can be seen to fit more tightly around the heart however, although the lungs are larger, in the flushing breath images the SNR is lower. This is to be expected as both images are taken with 1L of ^{129}Xe and so the flushing breath has caused the gas to become more diluted within the lungs causing a decrease in SNR. This dilution factor is more significant among healthy volunteers with large lung capacities. It is expected that when this study progresses onto patients with airways disease the dilution factor will be less of an issue due to reduced lung capacity.

One practical advantage of the flushing breath is patient comfort. The volunteers were required to hold their breath for the duration of each scan for obvious reasons. This could take up to 12 seconds which would ordinarily not be an issue for the majority of healthy individuals, but as the volunteer must fully exhale before inhaling 1L of ^{129}Xe instead of air, it can be a challenge for some to maintain a breath hold for the duration of the scan without the addition of a small amount of air. There have been no failed scans due to volunteers being unable to maintain a breath hold so far but as the study progresses into patients with airways disease this is likely to become more of an issue.

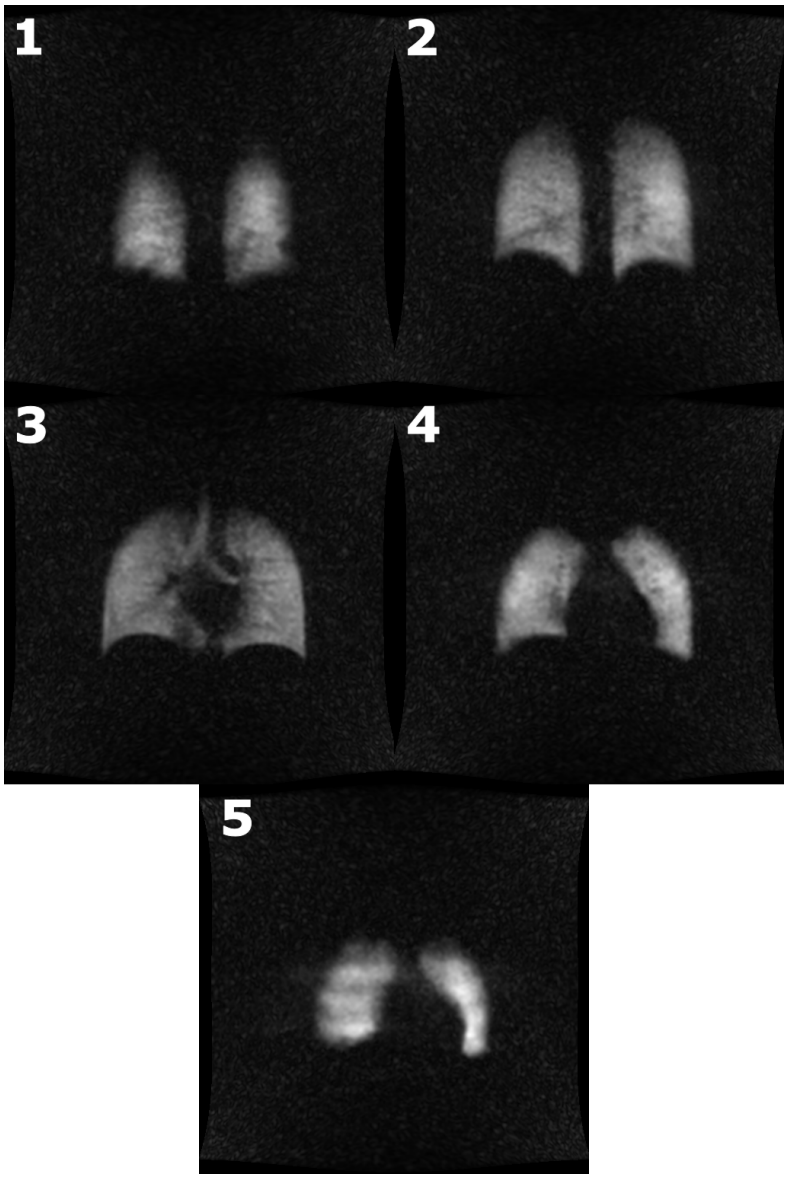


Figure 3.32: Series of 25mm coronal slices of volunteer 006 without a flushing breath. Slices 1 to 5 go from posterior to anterior. FOV = 48cm, Res = 128x128, T_E = 5.0ms, T_R = 7.6ms, flip angle = 30°.

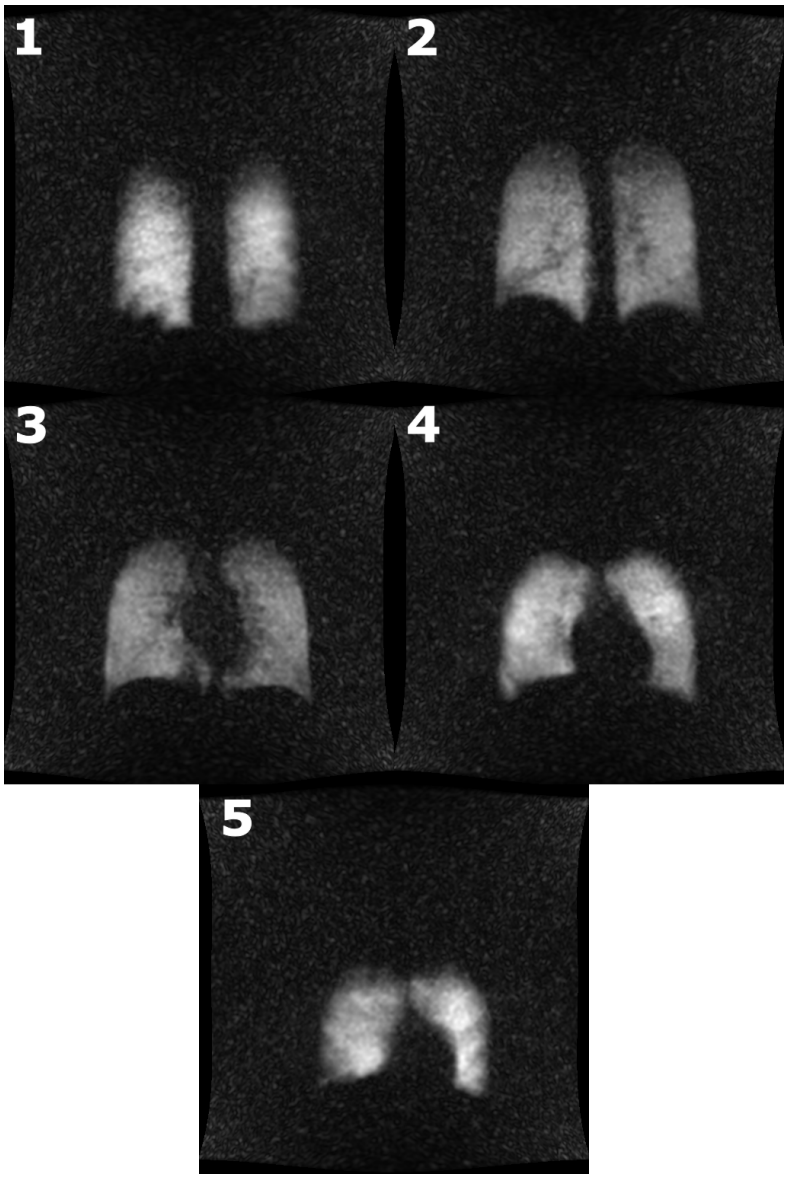


Figure 3.33: Series of 25mm coronal slices of volunteer 006 without a flushing breath. Slices 1 to 5 go from posterior to anterior. FOV = 48cm, Res = 128x128, T_E = 5.0ms, T_R = 7.6ms, flip angle = 30°.

3.6.7 Dissolved Phase Imaging

One of the advantages of using ^{129}Xe for imaging is that ^{129}Xe dissolved into the blood follows the same pathway as oxygen. As this causes a chemical shift it is possible to specifically image ^{129}Xe dissolved in the blood around the lungs. This is known as the dissolved phase image. Figure 3.34 shows the spectrum of ^{129}Xe shortly after inhalation by volunteer 016. The large peak at 200 ppm corresponds to the gaseous ^{129}Xe within the lungs of the volunteer. The peak with two components at 0 ppm corresponds to the dissolved ^{129}Xe with the two components corresponding to ^{129}Xe dissolved in blood (left peak) and ^{129}Xe dissolved in tissue fluid (right peak).

Dissolved phase imaging allows physiological information about gas exchange within the lung on top of the ventilation imaging that has already been discussed. However it can be seen from Figure 3.34 that the signal intensity of the dissolved phase ^{129}Xe is significantly lower than that of the gaseous ^{129}Xe. In order to maximise the signal and produce and image the slice select gradient was deactivated to give a coronal projection. Several images were then taken over a ten second period and then averaged to produce a single image shown in Figure 3.35.

For the spectrum shown in Figure 3.34 the scan parameters used were as follows: number of samples = 4096, number of acquisitions = 25, T_R = 360ms and Spectral Width = 7042Hz. The dissolved phase image shown in Figure 3.35 was taken using the following scan parameters: FOV = 48cm, resolution = 64x64, T_E = 1.5ms, T_R = 15ms and Flip Angle = 30°.

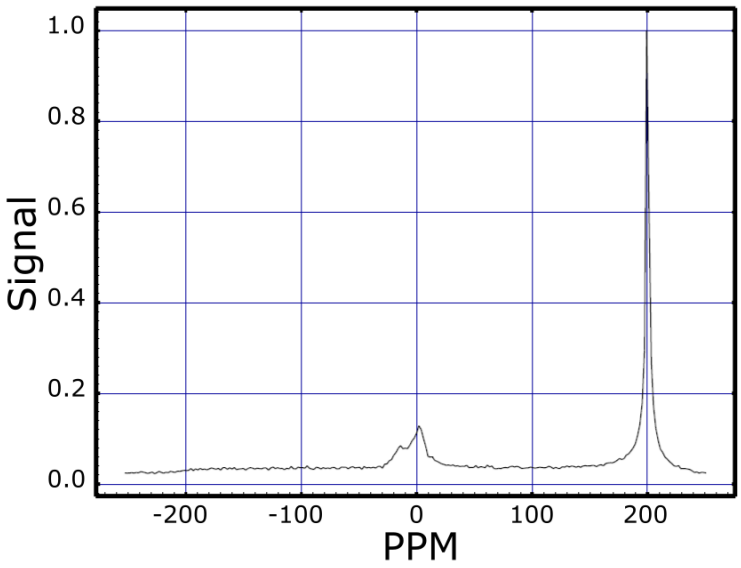


Figure 3.34: ^{129}Xe spectrum of Volunteer 15071-016 with dissolved phase peak visible at 0 ppm and gas phase peak visible at 200 ppm. Scan parameters: No. of samples = 4096, No. of acquisitions = 25, T_R = 360ms, Spectral Width = 7042 Hz.

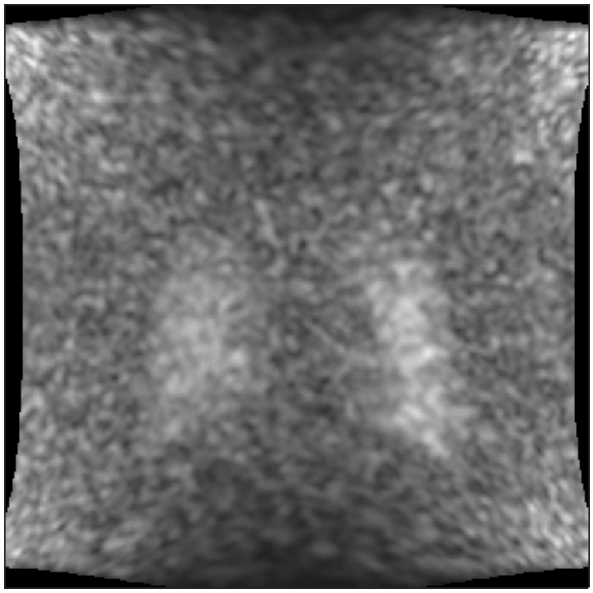


Figure 3.35: Volunteer 15065-004 coronal projection of dissolved phase ^{129}Xe. This image is the average of 5 images taken over a 10 second period. FOV = 48cm, Res = 64x64, T_E = 1.5ms, T_R = 15ms, flip angle = 30°.

3.7 Conclusion

There were two studies performed on healthy volunteers using HP gas MRI, one using ^{3}He and one using ^{129}Xe. The ^{3}He study sought to compare ADC measurements at two different time scales between two sites, the University of Nottingham (13ms) and the University of Sheffield (2ms) as well as investigate the relationship between age and ADC. Seven healthy adolescents were scanned at both sites with ages ranging from 12 to 20 years and a male/female ratio of 6/1. The results of this study were inconclusive with no obvious relation between the two sites (p=0.707) or between age and ADC (p=0.526). The main reason for these low correlations is most likely the small sample size. A significant number of additional measurements would be needed to confirm a lack of correlation between the two sites. The age data was compared with data from a previous study to increase the sample size. No significant correlation was seen between age and ADC at this larger sample size.

The ^{129}Xe study is an ongoing collaborative study with the aim of developing HP ^{129}Xe MRI techniques to the extent that reliable, reproducible and clinically relevant data can be readily acquired. Several different imaging techniques were investigated including dynamic imaging, coronal projections, and coronally and axially sliced images taken with a slice thickness of 25mm and 10mm. The quality of these images has varied however consistently useful images have been acquired with a slice thickness of 25mm. The advantages of interleaved scanning and breathing patterns (such as a flushing breath) have also been investigated. It has been observed that it is beneficial to use interleaved slicing when slicing axially whilst the presence of a flushing breath is something that should be determined on a case by case basis. For example if the patient is likely to be unable to maintain a breath hold for the duration of the scan without a flushing breath then they should be asked to do a flushing breath. Alternatively if the

SNR of an image is expected to be low then a flushing breath will only reduce it.

The ^{129}Xe project is still being developed with focus needed on increasing SNR, particularly at a lower slice thickness, and increasing the number of coronal projections and other repeat scans to better evaluated the repeatability of different techniques. The dissolved phase imaging also needs improving as the SNR of dissolved phased images is currently extremely low rendering the scans clinically useless despite their high potential for providing unique physiological data.

Due to technical issues with the polariser there has been no HP ^{129}Xe for the past two years. As a result the project was unable to expand into clinical scanning. Instead, developments were made in image processing techniques including the development of an automated SNR calculation algorithm, and the simulations of new ideas such as super resolution. Unfortunately the lack of HP gas has prevented these ideas from being fully tested.

Chapter 4

Conclusions and Future Work

4.1 Conclusions

Lung diseases are one of the leading causes of death, responsible for 20.1% of deaths in the UK in 2012 [8] and affecting the lives of many more. It is therefore important to continue to develop techniques for the diagnosis and treatment of various lung disease. This thesis explored two diagnostic techniques: Forced Oscillation Technique and Hyperpolarised gas MRI. Each technique has advantages and disadvantages and is suited for different purposes.

4.1.1 FOT

The non-imaging technique of FOT is a relatively inexpensive, quick and safe technique for assessing certain parameters about the respiratory system that describe the resistance of the airways as well as the reactance in terms of the compliance and inertance of the lungs. In this thesis the main parameters investigated were f_{res}, $R_5 - R_{20}$ and three parameters evaluated by fitting a

mathematical model (the aRIC model) to acquired data: R_c, I and C_p. A phantom study and a patient study have been presented in this thesis.

The phantom study tested the hypothesis that the Nottingham FOT system was a reliable system that accurately measured acoustic respiratory impedance. The aims of this study were to 1): to establish the validity of the Nottingham FOT system; 2): explore how physical changes to the resistance and compliance of a phantom affected FOT measurements; and 3): compare the Nottingham FOT system to two commercial systems at another site.

The first of these aims was achieved in part through calibration using a standard resistor which allowed the resistive component of the impedance measurement to be validated. A 50L Barrel phantom was used to establish the validity of the reactive measurement of the FOT system. The Barrel phantom could be treated as a Helholtz resonator undergoing forced oscillations. A theoretical reactance was then calculated for the Barrel and compared to the experimental data. It was found that the experimental data was an extremely good match to the theoretical data which confirms the validity of the Nottingham FOT system.

The second aim of the phantom study was achieved by using a 3-D printed lung phantom housed within a cylinder with a rubber diaphragm base. The compliance of the diaphragm could be adjusted to investigate the effect of changes in the overall compliance of a system on FOT parameters. Similarly the printed airways could be obstructed to investigate the effect of changes to the overall resistance of a system on measured FOT parameters. As expected, it was observed that adjusting the stiffness of the rubber diaphragm affected the reactive parameters f_{res} and C_p whilst obstructing airways had an effect on several resistive parameters such as R_c and $R_5 - R_{20}$. These results confirm that the FOT parameters are measuring appropriate aspects of lung condition.

The final aim of the phantom study was to compare three different FOT devices across two sites (The University of Nottingham and Glenfield Hospital, Leicester). This was done using a 3L syringe as well as the 3-D printed phantom. It was found that the tremoFlo C-100 airwave oscillometry system (located in Leicester) and the in-house Nottingham device were very similar in measurements despite producing the oscillations in two different ways (using a fan and a loudspeaker respectively). The Erich Jaeger MasterScreen IOS device (also located in Leicester) produced slightly different results to the other two systems. As the validity of the Nottingham system has already been examined through the Barrel phantom (and further confirmed through similarities with the tremoFlo system) it can be assumed that the difference in device measurements arises from the Jaeger system. It has been suggested that one possible source of this difference is that the Jaeger device operates using impulses rather than continuous sinusoidal waveforms. This could resulted in larger peaks in pressure that could affect the impedance of the system.

The patient study tested the hypothesis that FOT is a technique that provides complementary information to spiromtery about BD-reversibility. The aims of this study were to 1): confirm that FOT can distinguish between disease states in a similar manner to spirometry; 2): establish the differential effects of a BD on specific FOT parameters; and 3): establish whether patients with spirometric bronchodilator reversibility had BD response in FOT parameters. 57 patients (10 healthy, 26 asthmatic, 21 with COPD) underwent spirometry and FOT measurements pre- and post-BD.

The first aim of the patient study was achieved by comparing measured parameters between patient groups pre-BD. It was found that FOT and spirometry were both effective techniques for differentiating between the disease states of asthma and COPD, and healthy volunteers. The most significant differences

were seen between the Healthy group and the COPD group ($p<0.001$ all measured parameters except I and $R_5 - R_{20}$ where $p=0.002$). This demonstrates that FOT is comparable to spirometry in differentiating between these disease states.

The second aim of the patient study was investigated by comparing spirometry and FOT measurements pre- and post-BD. For the asthma group it was found that there was a significant change ($p<0.001$) for all parameters except FVC, I and $R_5 - R_{20}$ ($p = 0.928$,0.053 and 0.242 respectively). This demonstrates that FOT and spirometry are both effective in measuring response to SABA. A heterogeneity was seen in BD response between the patient groups with respect to measured parameter. This was most clearly seen in the FOT parameters C_p and f_{res} for which the most significantly different patient groups (according to BD response) were asthma and COPD respectively. This difference suggests that these parameters are measuring different patient response to SABA that potentially cannot be investigated using spirometry.

The final aim of the patient study was to investigate the response to SABA as seen by the two different measurement techniques. This was done by plotting the difference in FOT parameters against the percentage change in FEV_1. A variety in correlation between the FOT parameters and FEV1 was seen with some FOT parameter responses correlating more to FEV_1 than others. It was found that R_c was most similar to FEV_1 ($p=0.006$) whilst I was the least correlated ($p=0.771$). However, all FOT parameters (with the exception of $R_5 - R_{20}$) detected a significant response to SABA in the asthma group. This suggests that a variety of different responses were observed using FOT compared to spirometry. This has clinical significance as understanding how a patient will respond to SABA allows for treatment to be tailored to a patients specific requirements. It was observed that although FOT provided information about

patient response that was not observable using spirometry, the opposite was also true. Therefore, in order to gain the largest amount of information about a patients condition, both FOT and Spirometry would have to be carried out.

Overall, strong evidence was found for both tested hypotheses. The validity of the Nottingham system was confirmed through: a close match between experimental and theoretical data; a strong relationship between the physical conditions of a system and the corresponding FOT measurements; and a similarity between the Nottingham system and commercial systems. FOT was shown to provide complementary information to spiromtery about BD-response as it: differentiated between patient states in a comparable manner to spirometry; detected changes in the asthma group in a comparable manner to spirometry; and, some FOT parameters measured a response to SABA that did not correlate with FEV_1 suggesting alternative responses were being measured.

4.1.2 Hyperpolarised Gas MRI

HP gas MRI can be used as both a non-imaging technique and as an imaging technique. Both of these modalities were investigated in this thesis using two different noble gases. HP ^{3}He was used to measure global diffusion within the lungs for healthy volunteers, whilst HP ^{129}Xe was used for lung imaging.

The aim of the ^{3}He study was to compared the ADC of healthy volunteers measured at two different time scales (13ms and 2ms) two different sites: the University of Nottingham and the University of Sheffield. A secondary aim of this study was to investigate a potential relationship between age and ADC. No significant correlation was seen between the different time scale measurements from the two sites ($p=0.707$), however the sample size was very small ($n=7$) and so more volunteers would need to be scanned to confirm a difference between the two sites. There was also no correlation seen between age and ADC ($p=0.526$)

for volunteers scanned at the University of Nottingham including data taken during a previous study with a significantly larger sample size (n=269). This was unexpected as previous studies have suggested a link between age and ADC [88, 89].

Lung imaging was done using HP ^{129}Xe MRI as part of an ongoing study aiming to develop this technique to the point where it is sufficiently reliable, repeatable and interpretable for use in a clinical setting. In the future, the study will then progress to look at various disease states with a focus on patients with COPD and IPF. The aspects of HP ^{129}Xe MRI investigated were: dynamic imaging, coronal projections, the limitations of slice thickness, transverse plane imaging, patient breathing patterns and dissolved phase imaging. Significant improvements to the technique have been made since the initial scans were attempted.

Each patient will continue to undergo a coronal scan of an infinite slice thickness at the start of each scan session. This has already been done for many of the volunteers scanned so far with the SNR of these measurements displaying a surprising heterogeneity, both inter-, and intra-patient. It is thought that one of the main causes of this variation is patient breathing patterns with some patients inadvertently exhaling some of the gas mix before the scan commenced. A larger number of volunteers will have to be tested to fully explore the inter-patient variation of these measurements. It has also been found that images of a slice thickness of 10mm provide a good level of information however images of this slice thickness have issues with low SNR making many of the acquired images unusable. On the other hand images taken with a slice thickness of 25mm were reliably acquired however the increased thickness decreased the clinical usefulness of the image.

The majority of x-ray CT scans are performed in the transverse plane which has the advantage of being able to capture the entirety of the extremities of the lungs in one image. One issue with transverse plane HP gas MRI is that, due to the shape of the lungs, a larger number of scans are required to image the whole lung. As a result the patient is required to maintain a breath hold for a longer period of time, which could be an issue for patients with lung disease. Another issue with transverse plan imaging that was discovered is that the diffusion of the gas throughout the lung affected the images if they were scanned sequentially. This resulted in the first image being the brightest image with signal decaying for each subsequent slice until information was lost. This can be alleviated by scanning in an interleaved fashion rather than sequentially. Several scans were performed to explore the benefits and difficulties of introducing a flushing breath to the patients breathing to ensure there was no HP gas remaining in the upper airways. This allows for better measurements of TLC at the expense of SNR caused by an increased dilution factor.

It was found that both dynamic and dissolved phase imaging are currently not viable imaging techniques. For dynamic imaging this is due to the fact that the gas was being depolarised, due to the r.f. pulses of the scan, at the same rate it was being inhaled. As a result the extremities of the lung could not be imaged. It is possible this could be addressed by adjusting the scan parameters in order to reduce the rate of depolarisation. However, this will also decrease the SNR of the acquired images. The signal intensity from the dissolved phase peak is significantly smaller that the gaseous phase and therefore the SNR of dissolved phased images is currently too small to be clinically useful. As the HP ^{129}Xe gas MRI technique improves it should be possible to produce better quality dissolved phased images that have clinical value.

The main aim of the HP $^{1}29$Xe MRI study is to investigate patient disease states using ventilation imaging. This requires a standard scan protocol to be developed that maximises image quality by striking a balance between reducing slice thickness to increase spatial resolution and increasing slice thickness to increase SNR. Progress has been made with the implementation of a standard coronal projection at the start of each scan session, as well as exploration of different scan techniques (e.g. dynamic imaging, transverse plane imaging etc.). Unfortunately, there were technical issue with the polariser that prevented some of the ideas presented in this thesis from being fully tested including super resolution. These technical issue also prevented any clinical scans from being acquired.

4.1.3 Comparison of Modalities

Overall the two techniques investigated in this thesis are very different with very different applications despite both being lung function tests. The relative ease and low cost of FOT makes it a more viable test to be carried out as a standard lung function test alongside other tests such as spirometry and Peak Flow Tests. However, although both techniques can provide information about obstructive airways disease, FOT (and spirometry) cannot provide any information about the spatial location of obstructions within the lungs or the mobility of these obstructions over time. For this information, HP gas MRI is desirable despite its relatively high cost and risks associated with high strength magnetic fields. Ultimately, airways diseases are still being understood and the wide variety of conditions that can affect them requires a large variety of tests to investigate the different aspects of lung disease. As a result there is no one investigation that will provide all the necessary information for patient specific treatment to be performed but rather different investigations should be applied on a case by case basis.

4.2 Future Work

4.2.1 FOT

One interesting finding of the FOT study was the difference in measurements of the same phantom between the in-house Nottingham device and the Jaeger IOS system from Leicester. This difference could be further explored by performing FOT on the barrel phantom using the two Leicester devices and comparing these results to the measurements taken with the Nottingham device. It was suggested that one of the causes of difference between the systems was a difference in peak pressure due to the impulsive nature of the IOS system. The relationship between Z and peak pressure should be further investigated through a series of measurements taken using different amplitudes of a range of phantoms in order to fully explore this idea. Alternatively the Nottingham device could be reprogrammed to produce an impulsive waveform instead of a continuous sinusoid in an attempt to replicate the IOS measurements.

Further work could also be done using the barrel phantom to fully explore the difference between adiabatic and isothermal systems when measured using FOT. One suggestion for how this could be done is to fill the barrel phantom with a substance such as fibreglass to change the system from being adiabatic to being isothermal. The addition of fibreglass to change the nature of the system is currently being implemented by Thorasys (the company that produces the tremoFlo device) [60]. Alternatively, a series of measurements on phantoms of various volumes could be performed to investigate how the volume affects the nature of the system. The barrel phantom could also be improved by developing the resistive component of impedance to be frequency dependant.

The FOT study described in this thesis only considered patients with asthma and COPD. One direction the study could go in, in future, would be to look at

a larger variety of disease states to identify the range of disease states that FOT can distinguish between. This could be done in tandem with the HP gas MRI studies to allow the FOT and MRI measurements of different disease states to be directly compared.

4.2.2 Hyperpolarised Gas MRI

The results of the ^{3}He study were extremely inconclusive. This is mostly due to the small samples size and so the main way to move forward with this project is to perform further scans on a significant number of volunteers. Furthermore, it would be beneficial for the University of Sheffield to scan the volunteers who have already visited and measure ADC values at a larger time-scale in order to provide a better comparison of values. Once the study is established with a comparison drawn between healthy volunteers it could then be expanded to patients with lung disease.

As well as implementing some of the techniques described in this thesis such as super resolution, there are also many other developments that can and will be made to the Xe study in the near future, particularly regarding equipment. Firstly the new Clinical MR Solutions r.f. coil will be used on volunteers. As previously discussed this coil is expected to have a reduced rejection rate due to its more user friendly design. It is also hoped that the larger filling factor and higher gain will give an increased SNR allowing for better image quality, particularly at the 10mm slice thickness.

As well as a new r.f. coil there will also be a new ^{129}Xe polariser in use that is expected to be functioning within the next year. This will be a stopped-flow polariser with the potential to increase the polarisation of the ^{129}Xe administered to volunteers by a factor of two or three which will again increase the SNR of the images. The new polariser will also give the potential for both polarisers to

be run in parallel allowing for faster rate of scanning by reducing the duration of scan sessions.

A new MRI scanner has recently been installed in the QMC which will be also available for use in HP ^{129}Xe lung imaging in approximately one year. This is a 0.5 T upright Paramed Medical Systems MRI scanner shown in Figure 4.1. This will allow patients to be scanned in a variety of novel positions including seated. This will provide interesting new information about ventilation whilst upright and the effects of gravity on ^{129}Xe within the lung, as well as also allowing the imaging of patients with airways disease too severe to allow imaging in the supine position. It can also be seen from Figure 4.1 that the Paramed scanner has a much more open and friendly design to allow patients to be in a variety of positions within the scanner. This will allow the study to include volunteers with claustrophobia who would reject conventional scanning.

Along with the new hardware of a new r.f. coil, polariser and MRI scanner there is also due to be a change in the gas mixture administered to the patients from 2% natural abundance xenon to 50% natural abundance xenon. As well as this a further change will be made switching from natural abundance xenon to enriched xenon which contains a significantly higher proportion of ^{129}Xe. These changes will increase the polarisation of the administered gas and therefore increase image SNR.

Another option for future scanning is to perform ADC measurements using ^{129}Xe that could be compared against ^{3}He ADC measurements of the same patients. One advantage of using ^{129}Xe for ADC measurements is that ^{129}Xe diffuses at a slower rate than ^{3}He, which makes it better suited to measuring small scale structures. However the absorption of ^{129}Xe into the bloodstream would need to be considered in the ADC measurement.

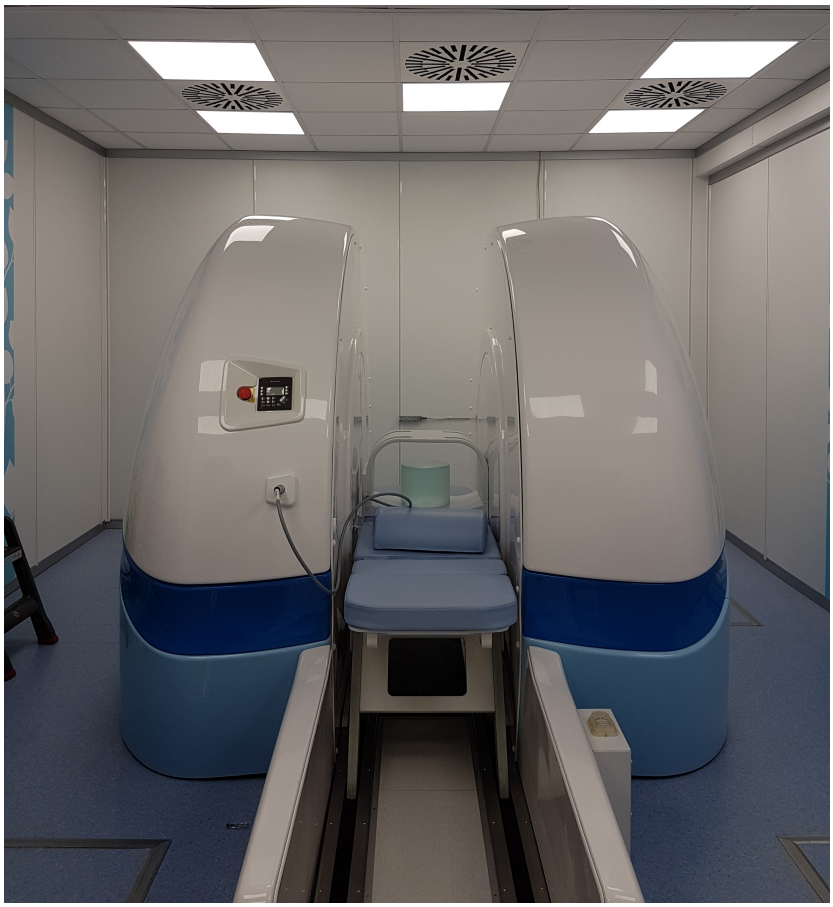


Figure 4.1: 0.5 T upright Paramed Medical Systems MRI scanner.

A particularly significant development to this research will be the shift to performing scans on patients with airways disease as well as healthy volunteers. The first addition will be patients with chronic obstructive pulmonary disease (COPD) starting with less severe cases to ensure that there are no adverse reactions to the ^{129}Xe that are exacerbated by the experimental set-up. Once the study is well established with COPD patient it will then be extended to include patients with idiopathic pulmonary fibrosis. These scans will be of significantly more clinical use than the previous scans of healthy volunteers.

Bibliography

[1] Andrew Turley Pippa McGowan, Angus Jeffries. *Crash Course: Respiratory System*. Mosby, 2nd edition edition, 2003.

[2] Arthur Dalley Keith Moore, Anne Agur. *Essential Clinical Anatomy*. Lippincott William & Wilkins, 4th edition edition, 2011.

[3] K. Horsfield. The relation between structure and function in the airways of the lung. *British journal of diseases of the chest*, 68:145–160, 1974.

[4] B. Haefeli-Bleuer and E. R. Weibel. Morphometry of the human pulmonary acinus. *The Anatomical Record*, 220(4):401–414, 1988.

[5] P. S. Hasleton. The internal surface area of the adult human lung. *Journal of anatomy*, 112(Pt 3):391, 1972.

[6] P. K. Jeffery and D. Li. Airway mucosa: secretory cells, mucus and mucin genes. *European Respiratory Journal*, 10(7):1655–1662, 1997.

[7] M. Salathe. *Cilia and Mucus: From Development to Respiratory Defense*. CRC Press, 2001.

[8] British Lung Foundataion. Lung disease in the uk. url: statistics.blf.org.uk, visited: 2017-07-27.

[9] M. S. Dunnill. The pathology of asthma, with special reference to changes in the bronchial mucosa. *Journal of clinical pathology*, 13(1):27–33, 1960.

[10] B. R. Wiggs and J. C. Higg. Small· airways dimensions in asthma and in chronic obstrudive pulmonary disease. 1993.

[11] Andrew G Nicholson Bryan Corrin. *Pathology of the Lungs*. Elsevier, 3rd edition edition, 2011.

[12] John Burnard West. *Pulmonary physiology and pathophysiology: an integrated, case-based approach*. Lippincott William & Wilkins, 2nd edition edition, 2007.

[13] B. E. Heard, V. Khatchatourov, H. Otto, N. V. Putov, and L. Sobin. The morphology of emphysema, chronic bronchitis, and bronchiectasis: definition, nomenclature, and classification. *Journal of clinical pathology*, 32(9):882, 1979.

[14] W. V. Cardoso, H. S. Sekhon, D. M. Hyde, and W. M. Thurlbeck. Collagen and elastin in human pulmonary emphysema. *American Review of Respiratory Disease*, 147:975–975, 1993.

[15] O. Auerbach, E. C. Hammond, L. Garfinkel, and C. Benante. Relation of smoking and age to emphysema: whole-lung section study. *New England Journal of Medicine*, 286(16):853–857, 1972.

[16] E. D. Bateman, Helen K Reddel, Richard N van Zyl-Smit, and Alvar Agusti. The asthma–copd overlap syndrome: towards a revised taxonomy of chronic airways diseases? *The Lancet Respiratory Medicine*, 3(9):719–728, 2015.

[17] Ganesh Raghu, Harold R Collard, Jim J Egan, Fernando J Martinez, Juergen Behr, Kevin K Brown, Thomas V Colby, Jean-François Cordier, Kevin R Flaherty, Joseph A Lasky, et al. An official ats/ers/jrs/alat statement: idiopathic pulmonary fibrosis: evidence-based guidelines for

diagnosis and management. *American journal of respiratory and critical care medicine*, 183(6):788–824, 2011.

[18] T. M. Maher, A. U. Wells, and G. J. Laurent. Idiopathic pulmonary fibrosis: multiple causes and multiple mechanisms? *European Respiratory Journal*, 30(5):835–839, 2007.

[19] J. Park, D. S. Kim, T. S. Shim, C. M. Lim, Y. Koh, S. D. Lee, W. S. Kim, W. D. Kim, J. S. Lee, and K. S. Song. Lung cancer in patients with idiopathic pulmonary fibrosis. *European Respiratory Journal*, 17(6):1216–1219, 2001.

[20] M. Selman, T. E. King, and A. Pardo. Idiopathic pulmonary fibrosis: prevailing and evolving hypotheses about its pathogenesis and implications for therapy. *Annals of internal medicine*, 134(2):136–151, 2001.

[21] T. J. Williams and J. W. Wilson. Challenges in pulmonary fibrosis: 7· novel therapies and lung transplantation. *Thorax*, 63(3):277–284, 2008.

[22] British Thoracic Society. *Spirometry in Practice*, second edition, april 2005.

[23] E. D. Bateman, S. S. Hurd, P. J. Barnes, J. Bousquet, J. M. Drazen, M. FitzGerald, P. Gibson, K. Ohta, P. O'byrne, S. E. Pedersen, et al. Global strategy for asthma management and prevention: Gina executive summary. *European Respiratory Journal*, 31(1):143–178, 2008.

[24] A. B. Otis, W. O. Fenn, and H. Rahn. Mechanics of breathing in man. *Journal of applied physiology*, 2(11):592–607, 1950.

[25] J. Mead and J. L. Whittenberger. Evaluation of airway interruption technique as a method for measuring pulmonary air-flow resistance. *Journal of applied physiology*, 6(7):408–416, 1954.

[26] A. B. DuBois, A. W. Brody, D. H. Lewis, and B. F. Burgess. Oscillation mechanics of lungs and chest in man. *Journal of Applied Physiology*, 8(6):587–594, 1956.

[27] E. Oostveen, D. MacLeod, H. Lorino, R. Farre, Z. Hantos, K. Desager, F. Marchal, et al. The forced oscillation technique in clinical practice: methodology, recommendations and future developments. *European Respiratory Journal*, 22(6):1026–1041, 2003.

[28] M. D. Goldman, C. Saadeh, and D. Ross. Clinical applications of forced oscillation to assess peripheral airway function. *Respiratory physiology & neurobiology*, 148(1):179–194, 2005.

[29] K. R. Lutchen, K. Yang, D. W. Kaczka, and B. Suki. Optimal ventilation waveforms for estimating low-frequency respiratory impedance. *Journal of Applied Physiology*, 75(1):478–488, 1993.

[30] K. Desiraju and A. Agrawal. Impulse oscillometry: The state-of-art for lung function testing. *Lung India: official organ of Indian Chest Society*, 33(4):410, 2016.

[31] J. Hellinckx, M. Cauberghs, K. De Boeck, and M. Demedts. Evaluation of impulse oscillation system: comparison with forced oscillation technique and body plethysmography. *European Respiratory Journal*, 18(3):564–570, 2001.

[32] S. Sato, T. Hirai, K. Tanimura, K. Hasegawa, S. Muro, and M. Mishima. Comparison of three devices for respiratory impedance measurement using forced oscillation technique: Basic study using phantom models. In *A58. ASSESSING PULMONARY FUNCTION: SPIROMETRY AND BEYOND*, pages A2100–A2100. Am Thoracic Soc, 2015.

[33] E. D. Michaelson, E. D. Grassman, and W. R. Peters. Pulmonary mechanics by spectral analysis of forced random noise. *Journal of Clinical Investigation*, 56(5):1210, 1975.

[34] H. J. Smith, P. Reinhold, and M. D. Goldman. Forced oscillation technique and impulse oscillometry. *European Respiratory Monograph*, 31:72, 2005.

[35] K. R. Lutchen, J. R. Everett, and A. C. Jackson. Impact of frequency range and input impedance on airway-tissue separation implied from transfer impedance. *Journal of Applied Physiology*, 74(3):1089–1099, 1993.

[36] T. Woo, B. Diong, L. Mansfield, M. Goldman, P. Nava, and H. Nazeran. A comparison of various respiratory system models based on parameter estimates from impulse oscillometry data. In *Engineering in Medicine and Biology Society, 2004. IEMBS'04. 26th Annual International Conference of the IEEE*, volume 2, pages 3828–3831. IEEE, 2004.

[37] B. Diong, A. Rajagiri, M. Goldman, and H. Nazeran. The augmented ric model of the human respiratory system. *Medical & biological engineering & computing*, 47(4):395–404, 2009.

[38] C. P. Criée, S. Sorichter, H. J. Smith, P. Kardos, R. Merget, D. Heise, D. Berdel, D. Köhler, H. Magnussen, W. Marek, et al. Body plethysmography–its principles and clinical use. *Respiratory medicine*, 105(7):959–971, 2011.

[39] A. Horsley. Lung clearance index in the assessment of airways disease. *Respiratory medicine*, 103(6):793–799, 2009.

[40] B. Friis, M. Eiken, A. Hornsleth, and A. Jensen. Chest x-ray appearances in pneumonia and bronchiolitis. *Acta Paediatrica*, 79(2):219–225, 1990.

[41] M. Puderbach, M. Eichinger, J. Haeselbarth, S. Ley, A. Kopp-Schneider, S. Tuengerthal, A. Schmaehl, C. Fink, C. Plathow, M. Wiebel, et al.

Assessment of morphological mri for pulmonary changes in cystic fibrosis (cf) patients: comparison to thin-section ct and chest x-ray. *Investigative radiology*, 42(10):715–724, 2007.

[42] Public Health England. Patient dose information: Guidance. url: https://www.gov.uk/government/publications/medical-radiation-patient-doses/patient-dose-information-guidance, visited: 2017-08-08.

[43] P. M. Silverman, C. J. Cooper, D. I. Weltman, and R. K. Zeman. Helical ct: practical considerations and potential pitfalls. *Radiographics*, 15(1):25–36, 1995.

[44] A. Taylor, D. Harnden, C. Arlett, S. Harcourt, A. Lehmann, S. Stevens, and B. Bridges. Ataxia telangiectasia: a human mutation with abnormal radiation sensitivity. *Nature*, 258(5534):427, 1975.

[45] K. M. Johnson, S. B. Fain, M. L. Schiebler, and S. Nagle. Optimized 3d ultrashort echo time pulmonary mri. *Magnetic resonance in medicine*, 70(5):1241–1250, 2013.

[46] K. Kwong, J. Belliveau, D. Chesler, I. Goldberg, R. Weisskoff, B. Poncelet, D. Kennedy, B. Hoppel, M. Cohen, and R. Turner. Dynamic magnetic resonance imaging of human brain activity during primary sensory stimulation. *Proceedings of the National Academy of Sciences*, 89(12):5675–5679, 1992.

[47] S. Ogawa, R. Menon, D. Tank, S. Kim, H. Merkle, J. Ellermann, and K. Ugurbil. Functional brain mapping by blood oxygenation level-dependent contrast magnetic resonance imaging. a comparison of signal characteristics with a biophysical model. *Biophysical journal*, 64(3):803–812, 1993.

[48] R. R. Edelman, H. Hatabu, E. Tadamura, W. Li, and P. V. Prasad. Noninvasive assessment of regional ventilation in the human lung using oxygen–enhanced magnetic resonance imaging. *Nature medicine*, 2(11):1236–1239, 1996.

[49] P. Zanzonico. Principles of nuclear medicine imaging: planar, spect, pet, multi-modality, and autoradiography systems. *Radiation research*, 177(4):349–364, 2012.

[50] S. Capitanio, A. J. Nordin, A. R. Noraini, and C. Rossetti. Pet/ct in nononcological lung diseases: current applications and future perspectives. *European Respiratory Review*, 25(141):247–258, 2016.

[51] M. J. Belman, W. C. Botnick, and J. W. Shin. Inhaled bronchodilators reduce dynamic hyperinflation during exercise in patients with chronic obstructive pulmonary disease. *American journal of respiratory and critical care medicine*, 153(3):967–975, 1996.

[52] R. L. Dellaca, P. Santus, A. Aliverti, N. Stevenson, S. Centanni, P. T. Macklem, A. Pedotti, and P. M. A. Calverley. Detection of expiratory flow limitation in copd using the forced oscillation technique. *European Respiratory Journal*, 23(2):232–240, 2004.

[53] G. G. King, S. R. Downie, S. Verbanck, C. W. Thorpe, N. Berend, C. M. Salome, and B. Thompson. Effects of methacholine on small airway function measured by forced oscillation technique and multiple breath nitrogen washout in normal subjects. *Respiratory physiology & neurobiology*, 148(1):165–177, 2005.

[54] F. C. Sciurba. Physiologic similarities and differences between copd and asthma. *CHEST Journal*, 126(2_suppl_1):117S–124S, 2004.

[55] D. S. Postma and K. F. Rabe. The asthma-copd overlap syndrome. *New England Journal of Medicine*, 373(13):1241–1249, 2015.

[56] M. L. Levy, P. N. R. Dekhuijzen, P. J. Barnes, M. Broeders, C. J. Corrigan, B. L. Chawes, L. Corbetta, J. C. Dubus, T. Hausen, F. Lavorini, et al. Inhaler technique: facts and fantasies. a view from the aerosol drug management improvement team (admit). *NPJ primary care respiratory medicine*, 26:16017, 2016.

[57] Thomas Rossing and Neville Fletcher. *Principles of Vibration and Sound*. Springer, 2nd edition edition, 1995.

[58] M. Schmidt, B. Foitzik, O. Hochmuth, and G. Schmalisch. Computer simulation of the measured respiratory impedance in newborn infants and the effect of the measurement equipment. *Medical engineering & physics*, 20(3):220–228, 1998.

[59] M. Yaegashi, V. A. K. Yalamanchili, V. Kaza, J. Weedon, A. E. Heurich, and M. J. Akerman. The utility of the forced oscillation technique in assessing bronchodilator responsiveness in patients with asthma. *Respiratory medicine*, 101(5):995–1000, 2007.

[60] G. Drapeau. Personal communication 31-01-2018.

[61] Malcolm Levitt. *Spin Dynamics: Basics of Nuclear Magnetic Resonance*. WILEY, 2nd edition edition, 2008.

[62] B. C. Grover. Noble-gas nmr detection through noble-gas-rubidium hyperfine contact interaction. *Physical Review Letters*, 40(6):391, 1978.

[63] Donald McRobbie, Elizabeth Moore, Martin Graves, and Martin Prince. *MRI From Picture to Proton*. Cambridge University Press, 2003.

[64] James Keeler. *Understanding NMR Spectroscopy*. WILEY, 2nd edition edition, 2010.

[65] Eiichi Fukushima and Stephen Roeder. *Experimental Pulse NMR. A nuts a bolts approach*. Westview Press, 1981.

[66] F. D. Colegrove and P. A. Franken. Optical pumping of helium in the s 1 3 metastable state. *Physical Review*, 119(2):680, 1960.

[67] F. D. Colegrove, L. D. Schearer, and G. K. Walters. Polarization of he 3 gas by optical pumping. *Physical Review*, 132(6):2561, 1963.

[68] Stanley J Kruger, Scott K Nagle, Marcus J Couch, Yoshiharu Ohno, Mitchell Albert, and Sean B Fain. Functional imaging of the lungs with gas agents. *Journal of Magnetic Resonance Imaging*, 43(2):295–315, 2016.

[69] A. Kastler. Optical methods of atomic orientation and of magnetic resonance. *JOSA*, 47(6):460–465, 1957.

[70] A. W. Overhauser. Polarization of nuclei in metals. *Physical Review*, 92(2):411, 1953.

[71] M. A. Bouchiat, T. R. Carver, and C. M. Varnum. Nuclear polarization in he 3 gas induced by optical pumping and dipolar exchange. *Physical Review Letters*, 5(8):373, 1960.

[72] J. Skinner. *Optimisation of Xenon-Rich Stopped-Flow Spin-Exchange Optical Pumping for Functional Lung Imaging*. PhD thesis, The University of Nottingham, 2016.

[73] D. Yablonskiy, A. Sukstanskii, J. Quirk, J. Woods, and M. Conradi. Probing lung microstructure with hyperpolarized noble gas diffusion mri: theoretical models and experimental results. *Magnetic resonance in medicine*, 71(2):486–505, 2014.

[74] J. Woods, C. Choong, D. Yablonskiy, J. Bentley, J. Wong, J. Pierce, J. Cooper, P. Macklem, M. Conradi, and J. Hogg. Hyperpolarized 3he

diffusion mri and histology in pulmonary emphysema. *Magnetic resonance in medicine*, 56(6):1293–1300, 2006.

[75] D. Gierada, J. Woods, A. Bierhals, S. Bartel, J. Ritter, C. Choong, N. Das, C. Hong, T. Pilgram, Y. Chang, et al. Effects of diffusion time on short-range hyperpolarized 3he diffusivity measurements in emphysema. *Journal of Magnetic Resonance Imaging*, 30(4):801–808, 2009.

[76] B. Saam, D. Yablonskiy, V. Kodibagkar, J. Leawoods, D. Gierada, J. Cooper, S. Lefrak, and M. Conradi. Mr imaging of diffusion of 3he gas in healthy and diseased lungs. *Magnetic resonance in medicine*, 44(2):174–179, 2000.

[77] M. Salerno, E. de Lange, T. Altes, J. Truwit, J. Brookeman, and J. Mugler. Emphysema: hyperpolarized helium 3 diffusion mr imaging of the lungs compared with spirometric indexesinitial experience. *Radiology*, 222(1):252–260, 2002.

[78] S. Fichele. *Hyperpolarised 3He Gas Production for Magnetic Resonance Imaging of the Human Air-ways*. PhD thesis, The University of Nottingham, 2002.

[79] H. Carr and E. Purcell. Effects of diffusion on free precession in nuclear magnetic resonance experiments. *Physical review*, 94(3):630, 1954.

[80] S. Meiboom and D. Gill. Modified spin-echo method for measuring nuclear relaxation times. *Review of scientific instruments*, 29(8):688–691, 1958.

[81] E. O. Stejskal and J. E. Tanner. Spin diffusion measurements: spin echoes in the presence of a time-dependent field gradient. *The journal of chemical physics*, 42(1):288–292, 1965.

[82] B. Waters. *Imaging the Lungs using Hyperpolarised Helium-3*. PhD thesis, The University of Nottingham, 2006.

[83] B. Waters, J. Owers-Bradley, and M. Silverman. Acinar structure in symptom-free adults by helium-3 magnetic resonance. *American journal of respiratory and critical care medicine*, 173(8):847–851, 2006.

[84] I. Ball. *Functional Pulmonary MRI using Hyperpolarised 3He*. PhD thesis, The University of Nottingham, 2011.

[85] C. Wang, G. Miller, T. Altes, E. de Lange, G. Cates Jr, and J. Mugler. Time dependence of 3he diffusion in the human lung: Measurement in the long-time regime using stimulated echoes. *Magnetic resonance in medicine*, 56(2):296–309, 2006.

[86] M. Narayanan, J. Owers-Bradley, C. S. Beardsmore, M. Mada, I. Ball, R. Garipov, K. S. Panesar, C. E. Kuehni, B. D. Spycher, S. E. Williams, et al. Alveolarization continues during childhood and adolescence: new evidence from helium-3 magnetic resonance. *American journal of respiratory and critical care medicine*, 185(2):186–191, 2012.

[87] S. Gonem, S. Hardy, N. Buhl, R. Hartley, M. Soares, R. Kay, R. Costanza, P. Gustafsson, C. E. Brightling, J. Owers-Bradley, et al. Characterization of acinar airspace involvement in asthmatic patients by using inert gas washout and hyperpolarized 3helium magnetic resonance. *Journal of Allergy and Clinical Immunology*, 137(2):417–425, 2016.

[88] S. Fain, T. Altes, S. Panth, M. Evans, B. Waters, J. Mugler, F. Korosec, T. Grist, M. Silverman, M. Salerno, et al. Detection of age-dependent changes in healthy adult lungs with diffusion-weighted 3he mri. *Academic radiology*, 12(11):1385–1393, 2005.

[89] T. Altes, J. Mata, E. de Lange, J. Brookeman, and J. Mugler. Assessment of lung development using hyperpolarized helium-3 diffusion mr imaging. *Journal of Magnetic Resonance Imaging*, 24(6):1277–1283, 2006.

[90] D. A. Yablonskiy, A. L. Sukstanskii, J. C. Leawoods, D. S. Gierada, G. L. Bretthorst, S. S. Lefrak, J. D. Cooper, and M. S. Conradi. Quantitative in vivo assessment of lung microstructure at the alveolar level with hyperpolarized 3he diffusion mri. *Proceedings of the National Academy of Sciences*, 99(5):3111–3116, 2002.

[91] S. Fichele, N. Woodhouse, A. J. Swift, Z. Said, M. N. J. Paley, L. Kasuboski, G. H. Mills, E. J. R. van Beek, and J. M. Wild. Mri of helium-3 gas in healthy lungs: posture related variations of alveolar size. *Journal of Magnetic Resonance Imaging*, 20(2):331–335, 2004.

[92] S. Fichele, M. N. J. Paley, N. Woodhouse, P. D. Griffiths, E. J. R. van Beek, and J. M. Wild. Investigating 3he diffusion nmr in the lungs using finite difference simulations and in vivo pgse experiments. *Journal of Magnetic Resonance*, 167(1):1–11, 2004.

[93] O. Dietrich, J. G. Raya, S. B. Reeder, M. F. Reiser, and S. O. Schoenberg. Measurement of signal-to-noise ratios in mr images: Influence of multichannel coils, parallel imaging, and reconstruction filters. *Journal of Magnetic Resonance Imaging*, 26(2):375–385, 2007.

[94] W. Dominguez-Viqueira, A. Ouriadov, R. O'halloran, S. B. Fain, and G. E. Santyr. Signal-to-noise ratio for hyperpolarized 3he mr imaging of human lungs: A 1.5 t and 3 t comparison. *Magnetic resonance in medicine*, 66(5):1400–1404, 2011.

[95] H. E. Möller, X. J. Chen, B. Saam, K. D. Hagspiel, G. A. Johnson, T. A. Altes, E. E. De Lange, and H-U Kauczor. Mri of the lungs using hyperpolarized noble gases. *Magnetic Resonance in Medicine*, 47(6):1029–1051, 2002.

[96] A. Buades, B. Coll, and J-M Morel. A non-local algorithm for image denoising. In *Computer Vision and Pattern Recognition, 2005. CVPR*

2005. IEEE Computer Society Conference on, volume 2, pages 60–65. IEEE, 2005.

[97] P. Coupé, J. V. Manjón, V. Fonov, J. Pruessner, M. Robles, and D. L. Collins. Patch-based segmentation using expert priors: Application to hippocampus and ventricle segmentation. *NeuroImage*, 54(2):940–954, 2011.

[98] H. Greenspan, G. Oz, N. Kiryati, and S. Peled. Mri inter-slice reconstruction using super-resolution. *Magnetic resonance imaging*, 20(5):437–446, 2002.

[99] E. Van Reeth, I. W. K. Tham, C. H. Tan, and C. L. Poh. Super-resolution in magnetic resonance imaging: A review. *Concepts in Magnetic Resonance Part A*, 40(6):306–325, 2012.

[100] E. Carmi, S. Liu, N. Alon, A. Fiat, and D. Fiat. Resolution enhancement in mri. *Magnetic resonance imaging*, 24(2):133–154, 2006.

[101] R. R. Peeters, P. Kornprobst, M. Nikolova, S. Sunaert, T. Vieville, G. Malandain, R. Deriche, O. Faugeras, M. Ng, and P. Van Hecke. The use of super-resolution techniques to reduce slice thickness in functional mri. *International Journal of Imaging Systems and Technology*, 14(3):131–138, 2004.

[102] A. Ben-Ezra, H. Greenspan, and Y. Rubner. Regularized super-resolution of brain mri. In *Biomedical Imaging: From Nano to Macro, 2009. ISBI'09. IEEE International Symposium on*, pages 254–257. IEEE, 2009.

[103] Z. Yan and Y. Lu. Super resolution of mri using improved ibp. In *Computational Intelligence and Security, 2009. CIS'09. International Conference on*, volume 1, pages 643–647. IEEE, 2009.

[104] Y. Bai, X. Han, and J. L. Prince. Super-resolution reconstruction of mr brain images. In *Proc. of 38th annual conference on information sciences and systems (CISS04)*, pages 1358–1363, 2004.